Title
Electric field effects in combustion with non-thermal plasma

Author
Casey, Tiernan Albert

Publication Date
2016

Peer reviewed|Thesis/dissertation

Electric field effects in combustion with non-thermal plasma

by

Tiernan Albert Casey

A dissertation submitted in partial satisfaction of the

requirements for the degree of

Doctor of Philosophy

in

Engineering - Mechanical Engineering

and the Designated Emphasis

in

Computational and Data Science and Engineering

in the

Graduate Division

of the

University of California, Berkeley

Committee in charge:

Professor Jyh-Yuan Chen, Chair
Professor Carlos Fernandez-Pello
Professor Phillip Colella

Spring 2016

Electric field effects in combustion with non-thermal plasma

Abstract

Electric field effects in combustion with non-thermal plasma

by

Tiernan Albert Casey

Doctor of Philosophy in Engineering - Mechanical Engineering

with Designated Emphasis
in
Computational and Data Science and Engineering

University of California, Berkeley

Professor Jyh-Yuan Chen, Chair

Chemically reacting zones such as flames act as sources of charged species and can thus be considered as weakly-ionized plasmas. As such, the action of an externally applied electric field has the potential to affect the dynamics of reaction zones by enhancing transport, altering the local chemical composition, activating reaction pathways, and by providing additional thermal energy through the interaction of electrons with neutral molecules. To investigate these effects, one-dimensional simulations of reacting flows are performed including the treatment of charged species transport and non-thermal electron chemistry using a modified reacting fluid solver. A particular area of interest is that of plasma assisted ignition, which is investigated in a canonical one-dimensional configuration. An incipient ignition kernel, formed by localized energy deposition into a lean mixture of methane and air at atmospheric pressure, is subjected to sub-breakdown electric fields by applied voltages across the domain, resulting in non-thermal behavior of the electron sub-fluid formed during the discharge. Strong electric fields cause charged species to be rapidly transported from the ignition zone across the domain in opposite directions as charge fronts, augmenting the magnitude of the electric field in the fresh gas during the pulse through a dynamic-electrode effect. This phenomenon results in an increase in the energy of the electrons in the fresh mixture with increasing time, accelerating electron impact dissociation processes. A semi-analytic model to represent this dynamic electrode effect is constructed to highlight the relative simplicity of the electrodynamic problem admitted by the far more detailed chemistry and transport. Enhanced fuel and oxidizer decomposition due to electron impact dissociation and interaction with excited neutrals generate a pool of radicals, mostly O and H, in the fresh gas ahead of the flame's preheat zone. The effect of nanosecond pulses are to increase the mass of fuel burned at equivalent times relative to the unsupported ignition through enhanced radical generation, resulting in an increased heat release rate in the immediate aftermath of the pulse.

To those that made this journey possible

Thank you all

Contents

List of Figures

List of Tables

Nomenclature

$\boldsymbol{\sigma}$	Fluid stress tensor
$\boldsymbol{\tau}$	Fluid shear stress
$\dot{\omega}_k$	Mass production rate of species 'k'
$\dot{M}$	Mass flux
$\dot{Q}$	External energy source
ϵ	Ionization potential
η	Fluid dynamic viscosity (momentum diffusivity)
Λ	Thermal de Broglie wavelength
λ	Mixture thermal conductivity
λ_D	Debye length
μ	Fluid electrical mobility
ν_{en}	Electron neutral collision frequency
ω_p	Plasma frequency
ϕ	Electric potential
ρ	Fluid mass density
ρ_c	Charge density
σ_k	Electron collision cross section with neutral species 'k'
σ_m	Total momentum-transfer collision cross section
τ_d	Dielectric relaxation time
$\mathbf{E}$	Electric field

$\mathbf{f}$	Body force
$\mathbf{I}$	Identity tensor
$\mathbf{q}$	Energy flux
$\mathbf{u}$	Fluid velocity
$\mathbf{V}_k$	Diffusion velocity of species 'k' (i.e. fluid velocity of species 'k' relative to the bulk velocity)
ε	Electron energy
ε_0	Electric permittivity of a vacuum
f	Electron energy density (distribution function) in velocity-position phase space
N_A	Avogadro's number
q	Charge number of molecule
c_p	Mass specific heat at constant pressure conditions
c_v	Mass specific heat at constant volume conditions
CFD	Computational fluid dynamics
D_k	Mass diffusivity of species 'k'
DC	Direct current
DDT	Deflagration-to-detonation transition
e	Elementary charge
E_a	Activation energy
EEDF	Electron energy distribution function
FWHM	Full width at half maximum
h_k	Mass specific enthalpy of species 'k'
k_B	Boltzmann constant
LODI	Linear one-dimensional inviscid
M	Total number of species
m_e	Electron mass

Ma Mach number

N Total number density of neutral species

n Species number density

NSCBC Navier-Stokes characteristic boundary conditions

p Fluid thermodynamic pressure

PAC Plasma assisted combustion

R Universal gas constant

TSA Targeted Search Algorithm

TVD Total-variation-diminishing

W Mean molecular weight of mixture

W_k Molecular weight of species 'k'

X_k Mole fraction of species 'k'

Y_k Mass fraction of species 'k'

Acknowledgments

Thank you to my adviser Jyh-Yuan Chen for introducing me to computational reacting flow modeling and to the topic of plasma-assisted combustion, and for allowing me to pursue my interests in numerical modeling and high-performance computing during my Ph.D. studies. Thank you to Robert Dibble for introducing me to the field of combustion, for his many words of wisdom, and for his advice on how to balance being a mercenary scientist with doing 'good-things'. Thank you to Jie Han, Fabrizio Bisetti, and Memdouh Belhi at KAUST for the many fruitful discussions on plasma and reacting flows that helped me to develop an intuition for the non-intuitive nature of plasma combustion. Thank you to Hong Im and Paul Arias for their help with implementing functionality into the S3D solver, and for making the code available for this work. A special thanks to my Master's adviser Sigurdur Thoroddsen for launching my scientific career in fluid mechanics, for convincing me to pursue a Ph.D., and for helping me to develop the temperament to navigate academia.

I would like to thank all the students (too many to mention...) that I have had the chance to meet and work with during my tenure in the Combustion Modeling Lab, for creating a vibrant and fun atmosphere in the depths of Hesse Hall during my studies at Berkeley.

Finally, and most importantly, thank you to my wife Yulia for her unending patience and support during my studies.

Chapter 1

Introduction

1.1 Structure of this dissertation

This dissertation aims to investigate the behavior of plasma kinetic processes in combustion environments under the action of strong electric fields in the context of methane-air plasmas. This chapter summarizes the aims of the dissertation work, provides an overview of the relevance of energy research, and gives a brief introduction to the field of plasma research in the combustion context. In Chapter 2 the relevant theoretical models under consideration are developed. In Chapter 3, fundamental aspects of plasma dynamics are discussed. In Chapter 4 practical aspects of the treatment of plasmas in fluid models are developed. In Chapter 5, the numerical approaches employed in the simulations performed in this work are discussed. In Chapter 6, the application of the plasma fluid methodology is discussed in the context of laminar flames. In Chapter 7, the simulation framework is applied to a specific case of interest, namely plasma assisted ignition. Chapter 8 summarizes the work and gives insight into future developments and continued research directions. The appendices include useful derivations to support the theory used in the discussion, as well as the complete skeletal methane-air plasma mechanism used in this work.

1.2 Dissertation contributions

Contributions to the increased understanding of this area, the confluence of reacting flows and kinetic plasmas, include:

- Development of a two-fluid reacting flow solver to investigate non-thermal equilibrium chemistry under the action of strong electric fields.
- Description of the interactions resulting in ignition assistance in the planar plasma-assisted ignition regime.

- Analysis and model development for the mechanisms controlling the electrodynamics of charge fronts resulting in electric field enhancement.

1.3 The energy paradigm

The maintenance of modern living standards, through the use of technologies and advanced means of production that enable our access to increasingly complex goods and services, inevitably relies on stable access to energy. This is true both in highly industrialized countries and in the developing world, where for the latter technology is crucial in enabling societies to transition from subsistence to productive economic growth in order to lift their populations from endemic and generational poverty.

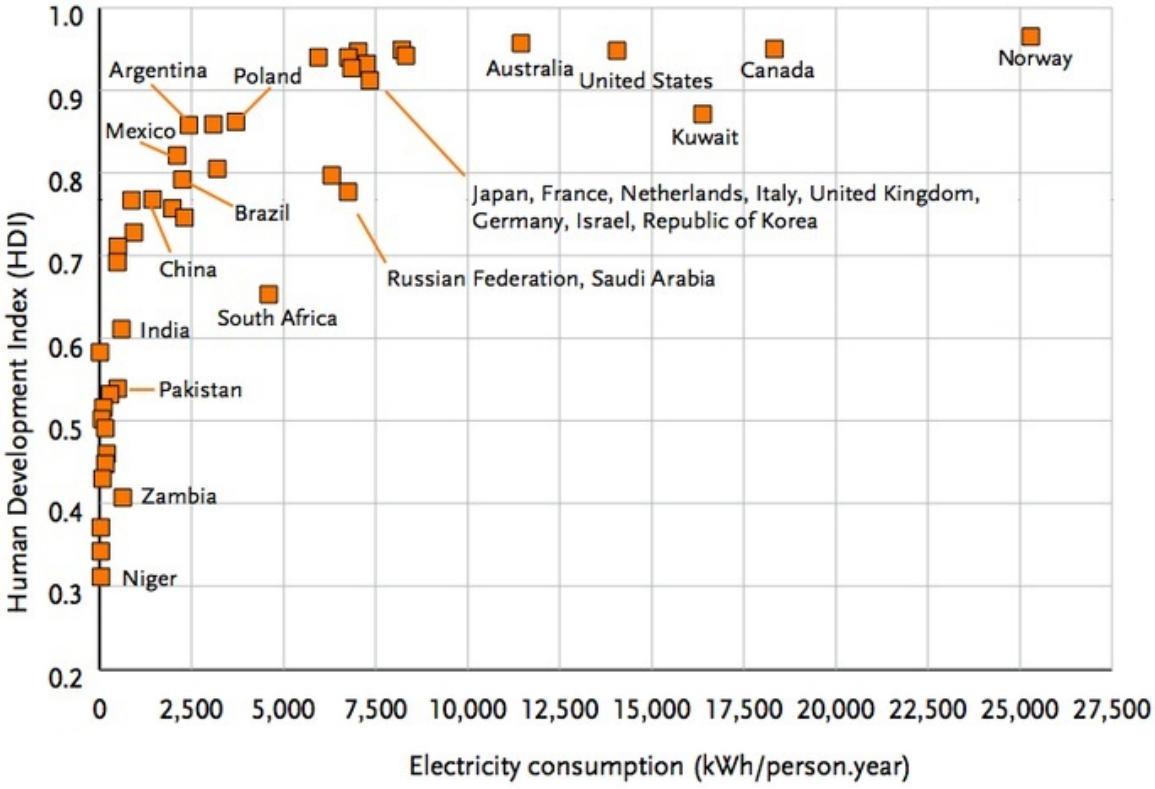

Figure 1.1: HDI and per capita energy consumption (UNDP, 2006)

Human development, as quantified using the composite Human Development Index (HDI) statistic, is evidenced to be highly correlated with the per capita use of electrical energy across a variety of countries (Fig. 1.1). A particularly urgent concern when considering this paradigm is the difficulty with which energy production can be expanded in developing countries while also mitigating the negative ecological, economic, and social aspects of the

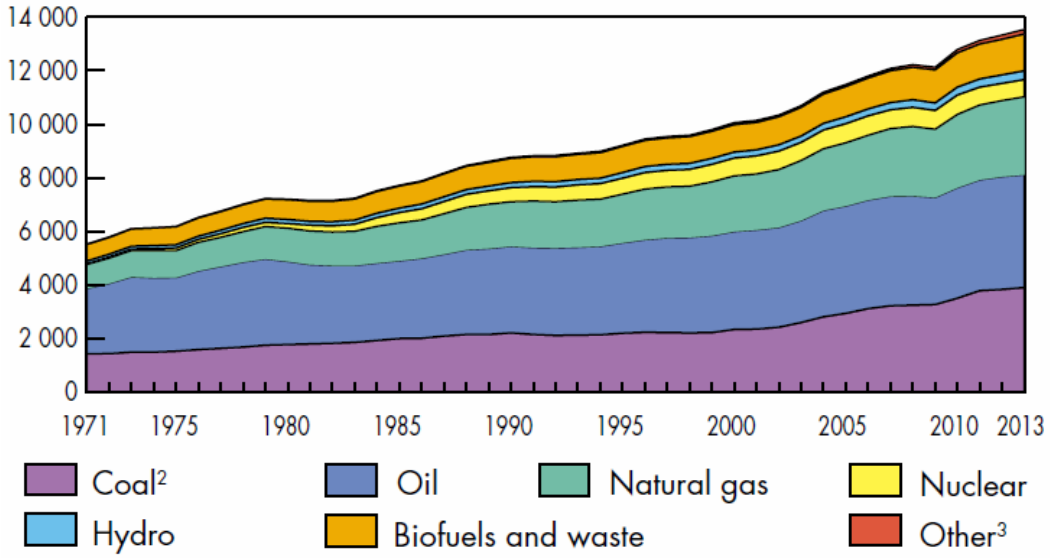

Figure 1.2: Global primary energy use from 1971 to 2013 in million tonnes of oil equivalent (Mtoe) (IEA, 2015).

use of polluting technologies. With respect to the current global energy mix, primary energy use is still dominated by fossil fuels (Fig. 1.2). This situation is expected to persist well into the current century, especially with the growth of energy use in countries with massive evolving middle class populations such as China and India. Using Norway as an extreme example for high living standards using HDI, the intensive energy use in that country has a relatively benign impact on the aspects listed previously due to the abundant availability of clean renewable hydroelectric energy sources. For countries that do not enjoy such natural resources, thermal plants employing coal and oil as energy sources are the cheapest modular alternatives for the rapid deployment of electrical capacity. Due to this economic reality, trends similar to that shown in Fig. 1.1 can also be developed to correlate economic development (e.g. per-capita Gross Domestic Product) with per-capita pollutant emissions. While the developing regulatory environment in the United States has heralded uncertainty as to the future of coal as an energy source for electrical power generation, throughout 2015 China commissioned a coal plant on average every two weeks and, as of 2016, Japan is currently planning to deploy more than 40 thermal plants using coal fuel to replace nuclear capacity in the wake of the political disdain for nuclear energy that developed globally following the 2011 Fukushima Daiichi disaster. However, the political will to transition from coal does appear to exist within both developed and developing countries. Natural gas, with a much lower emission intensity (defined as the mass of CO_2 emitted per Joule of energy delivered) appears to be a promising transition technology to mitigate the adverse effects of increasing use of coal and oil sources (IPCC, 2011). Faced with increasing severe pollution issues in its major cities, the Chinese government in 2014 signed a $400 billion dollar, 30-year contract with the government of the Russian Federation to supply natural gas with deliveries begin-

ning as early as 2018. An important aspect of this contract is the commitment to construct vast pipeline transit and distribution infrastructure that could see China transition towards natural gas as a primary energy source in the near future. As it stands, these global developments underscore the lasting importance that combustion technologies will have on energy use and human development for decades to come, as the importance of designing efficient, low-polluting combustors continues to be relevant to the sustainability of the global economy.

A crucial aspect of this paradigm is how global energy proliferation can be made compatible with concerns such as anthropomorphic climate change. Clean combustion technologies at their very best still rely fundamentally on the production of, and in the absence of capture and sequestration, emission of CO_2 into the atmosphere, and ongoing debate as to the appropriate treatment of CO_2 as a pollutant rages. Closed loop combustion technologies employing carbon capture and sequestration present promise (Steeneveldt et al., 2006; Blamey et al., 2010), but economic viability remains to be a huge issue. Growth in air travel also presents an acute challenge due to the difficulty in deploying emissions reduction or CO_2 capture technology onto mobile platforms without making powered flight essentially unfeasible. Recent interest in solar powered flight has produced prototype aircraft capable of long-distance travel, albeit not currently scalable to be commercially viable, while experiments as far back as the late 1980s were able to demonstrate the possibility of using cryogenically stored hydrogen as a fuel source to power a modified commercial airliner (Khandelwal et al., 2013). Again, reliable combustion technology is a crucial requirement for making such a zero (or near zero) emissions solution to global energy needs a reality.

1.4 Plasma assisted combustion

Plasma assisted combustion (PAC) has shown promise as a means to enhance the performance of a variety of reacting flow processes. Thermal plasmas have been used for decades to control ignition in engines (spark ignition), and non-thermal (i.e. non-equilibrium) plasmas are an area of active interest in combustion. The enhancement effect of the plasma is almost invariably associated with accelerated generation of reactive radical species through interaction of oxidizer molecules with ions, excited neutrals, and electrons, with the presence of any enhancement typically found to be strongly pressure dependent. Experiments and simulations performed by Uddi et. al. (Uddi et al., 2009) suggest that the primary formation mechanism of atomic O, a highly reactive radical, is by electron impact dissociation for PAC investigations of CH_4 (when using the GRI mechanism (Smith et al., 1999)) and C_2H_4 (when using USC Mech. II (Wang et al., 2007)) when considering supplemental plasma chemical processes. Enhancement can also be thermal in nature, through increased bulk gas heating by energy deposition (e.g. using microwave energy (Groff and Krage, 1984)) accelerating chemical rates and increasing the flame temperature or, for the case of ignition, the creation of larger ignition volumes facilitating accelerated transition to flame. While plasma processes can generate beneficial effects, pollutant formation can also be enhanced when attempting PAC. The production of ozone and oxides of nitrogen accelerates with increased densities

of atomic O, with ozone having an effect on low-temperature kinetics with the potential to modify flame speed (Won et al., 2015). A review of the fundamental processes in involved in PAC can be found in the reviews of Starikovskaia (2006), Starikovskiy and Aleksandrov (2013), and Sun and Ju (2013).

1.5 Advanced ignition technologies

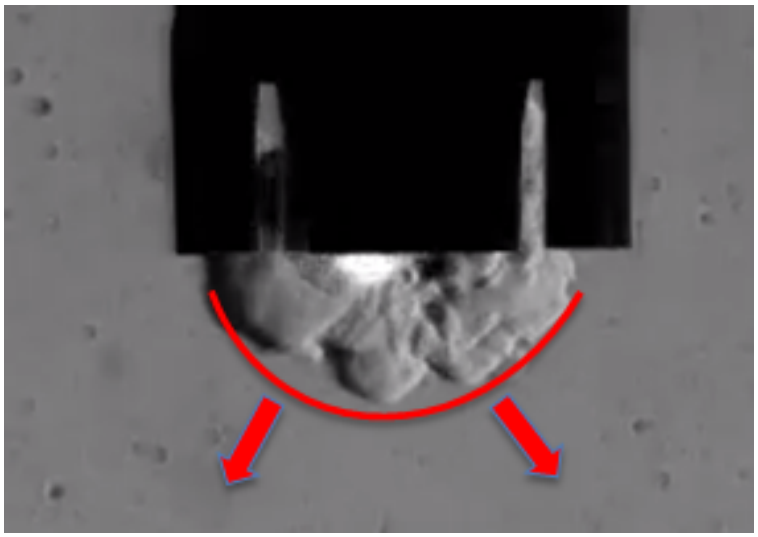

Figure 1.3: Nanosecond pulsed discharge spark plug

The development of next-generation engine technologies will require the consideration of new strategies for ensuring that controllable and reliable ignition can be initiated under a range of operating conditions. As emission standards continue to force engine designers to develop engines with smaller displacement (downsizing) the necessary satisfaction of power requirements is shifting operating modes to highly-boosted conditions. While highly-boosted conditions present unique challenges in their own right, e.g. super-knock at low-speed high-load conditions (Kalghatgi and Bradley, 2012), the generation of an ignition event also becomes more problematic. For spark-ignition using thermal plasma arc discharges, the ionization reactions required to generate breakdown of the reactant gases are mitigated by increased electron recombination reactions. Increasing electrode voltage and spark energy is a possible solution, but increased ablation at electrode surfaces inevitably reduces the lifetime and increases the expense of such devices.

Various novel technologies have been proposed as alternatives to arc discharge ignition as used in standard spark-plugs. Nanosecond duration pulsed discharges generating streamers in the glow regime have been proposed as a means to rapidly deposit thermal energy from non-thermal electrons into a reactant mixture leading to ignition (Pineda et al., 2015), although pulses of sufficient duration are typically found to result in transition to arcing (Fig.

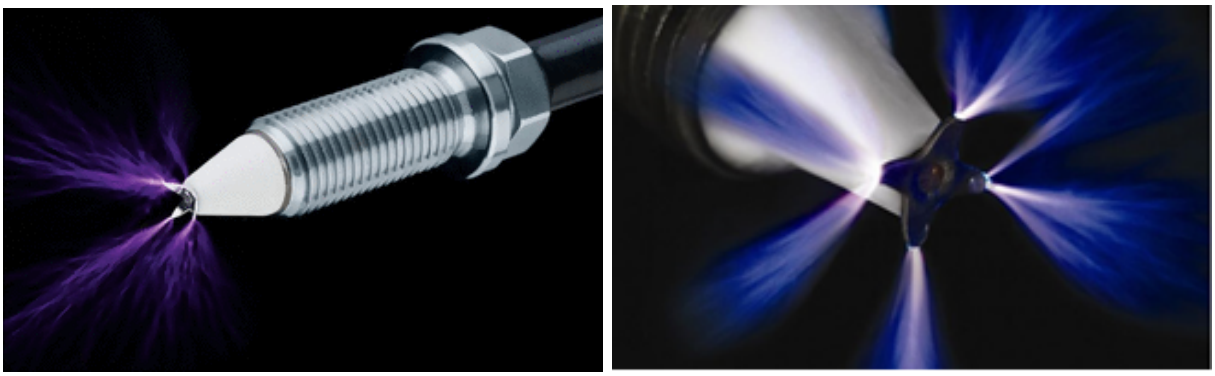

Figure 1.4: Corona discharge spark plug

1.3). An ignition device operating on the principle of corona discharge (Fig. 1.4) claims to achieve ignition and deliver improved combustion efficiency over standard arc discharge spark plugs (Burrows et al., 2013). A spark plug that employs a standard arc discharge followed by the application of microwave energy (Wolk et al., 2013; Ikeda et al., 2009) has been shown to support the development of an ignition kernel and decrease flame development time relative to the unsupported case. In all of these novel combustion systems the underlying mechanisms for combustion instigation or assistance are not well understood or difficult to investigate experimentally. As such, simple simulations play a vital role in probing the fundamental physics to elucidate the many factors at play.

Chapter 2

Theoretical models

2.1 Governing equations

The governing equations for reacting mixtures, i.e. the continuum statements of mass conservation, Newton's second law, and the first law of thermodynamics for chemically active mixtures of multiple fluids in local thermodynamic equilibrium are respectively (Poinsot and Veynante, 2005; Kuo, 1986):

$$\frac{\partial \rho Y_k}{\partial t} + \nabla \cdot (\rho Y_k \left[\mathbf{u} + \mathbf{V}_k\right]) = \dot{\omega}_k \tag{2.1}$$

$$\frac{\partial \rho \mathbf{u}}{\partial t} + \nabla \cdot (\rho \mathbf{u}\mathbf{u}) = \nabla \cdot \boldsymbol{\sigma} + \rho \sum_{k=1}^{M} Y_k \mathbf{f} \tag{2.2}$$

$$\frac{\partial \rho e_t}{\partial t} + \nabla \cdot (\rho \mathbf{u} e_t) = -\nabla \cdot \mathbf{q} + \nabla \cdot (\boldsymbol{\sigma} \mathbf{u}) + \rho \sum_{k=1}^{M} Y_k \mathbf{f}_k \left(\mathbf{u} + \mathbf{V}_k\right) + \dot{Q} \tag{2.3}$$

and are expressed here in the so called 'strong conservative' form, where transport flux terms of the conserved quantities appear explicitly under divergence operators. In addition to the transport equations governing conservation, for charged gases Gauss' law is required to establish the electric potential, the gradient of which (i.e. the electric field) will determine the body-forces on charged species:

$$\varepsilon_0 \nabla \cdot \mathbf{E} = \rho_c \tag{2.4}$$

In this work the value of the electric permittivity in the gaseous medium will be assumed to take the vacuum value.

The conservation of mass (Eq. 2.1) is cast in terms of each individual component species using mass fractions, and the energy equation (Eq. 2.3) is cast in terms of the sum of the bulk kinetic energy (i.e. the kinetic energy associated with the center of mass velocity of the mixture) and the mixture internal energy, where the internal energy encompasses both

sensible energy (relative to a reference temperature) and chemical energy (i.e. formation enthalpy at the reference temperature). This combination of energy terms is often referred to as the 'total' energy formulation, although it omits the kinetic energy associated with mass motion relative to center of mass velocity (i.e. the kinetic energy of diffusion) and as such is not 'total' in any objective sense. The energy flux term, $\mathbf{q}$, represents the transport of thermal energy by random molecular motion relative to the bulk fluid velocity and is typically modeled using the Fourier heat conduction model for pure gases but includes an additional contribution for mixtures, wherein the differential transport of mass carries the varying enthalpy of the constituent species by their respective velocities relative to the overall mass averaged velocity (i.e. their diffusion velocities):

$$\mathbf{q} = -\lambda \nabla T + \rho \sum_{k}^{M} h_k Y_k \mathbf{V}_k \tag{2.5}$$

Fluid stresses are typically modeled by first decomposing the stress tensor into isotropic and deviatoric components, and noting that the isotropic component terms correspond to the thermodynamic pressure of the fluid:

$$\boldsymbol{\sigma} = -p\mathbf{I} + \boldsymbol{\tau} \tag{2.6}$$

The deviatoric component is typically well modeled using the Newtonian fluid approximation, a constitutive model relating the deviatoric (shear) stresses to the fluid rate of strain through:

$$\boldsymbol{\tau} = \eta \left(\nabla \mathbf{u} + \nabla \mathbf{u}^T \right) - \mathbf{I} \frac{2\eta}{3} \nabla \cdot \mathbf{u} \tag{2.7}$$

This form of the governing equations will admit multiple interesting fluid phenomena including, non-linear advection, differential molecular mass diffusion of species, chemical reactions, and acoustic wave propagation. The appearance of acoustics is a consequence of solving the fluid energy equation directly without simplifying assumptions (as information associated with the internal energy propagates at a speed related to the physics of thermal motion) and while simple in its presentation, poses strict limitations on reacting flow simulations (and fluid simulations in general). Since many reacting flows are characterized by a vast range of time scales associated with chemical kinetics, the fluid response to such chemistry typically results in flow features with a variety of length scales. Flames for instance are thin zones with highly active chemistry that can typically have length scales on the order of fractions of millimeters at ambient conditions, requiring simulations to use spatial discretizations with thicknesses on the order of microns in order to resolve the rapidly changing curvature of profiles of interest within flames. The presence of the propagation of acoustic waves on numerical grids of such small dimensions can present severe penalties in terms of numerical stability of integration schemes if the time integration strategy relies on explicit integrators, which are often employed in simulations for simplicity or time accuracy. Since the energy carried by acoustic waves is typically small compared to the energetic processes

associated with the heat release from chemical reactions, acoustics rarely have an impact on many reacting flows of practical interest. Apart from detonations, or deflagration to detonation transitions (DDT), their presence in the governing formulation of the problem is essentially unnecessary.

When using such a formulation, the treatment of acoustic information propagation at boundaries is of crucial importance in order to reflect the natural propagation of information. In a spatially restricted domain, information from outside the domain (which could potentially affect the solution within the domain) is obviously not available. In order to avoid pollution of the solution within the domain, no information from outside should be allowed to enter the domain through boundaries and information from inside the domain should be allowed to freely propagate outwards. As such, boundary conditions can not be imposed on the conserved variables themselves, but rather on the characteristic variables whose wave vectors determine the speed and direction of information propagation. The derivation of the necessary relations between characteristic wave amplitudes and speeds at boundaries was performed by Poinsot & Lele (Poinsot and Lele, 1992) where the solutions at domain boundaries was assumed to be one-dimensional and inviscid, resulting in the so-called LODI relations. Corrections necessary to account for transverse variations, viscous forces, and reactions were developed subsequently resulting in the so-called NSCBC relations (Yoo and Im, 2007).

2.2 Constant pressure flames

An alternative to solving the energy equation as posed in Eq. 2.3 is to assume that the pressure field is essentially constant apart from the variations in pressure necessary to drive fluid flow. This is a commonly used approximation for combustion processes, to the point that the assumption of an isobaric process is often referred to as the 'combustion approximation' (Buckmaster and Ludford, 1982). Ignoring spatial variations in thermodynamic pressure typically allows for the use of much larger integration time steps compared to resolving acoustics (as the relevant hyperbolic equation requiring temporal resolution to be adequately propagated on the finite grid is now the far 'slower' momentum equation) and is as such a very attractive alternative to fully compressible flow. A governing formulation that acknowledged the separation of acoustic scales from the flow scales of interest was first employed by Rehm & Baum (Rehm and Baum, 1978) for simulations of buoyant flow in an open container. The procedure for eliminating acoustics proceeds as follows:

By employing a pressure decomposition:

$$p\left(x,t\right) = p_0\left(t\right) + p_1\left(x,t\right) \tag{2.8}$$

where p_0 is assumed to be the homogenous thermodynamic pressure and p_1 is a perturbation or dynamic pressure, which is an approximation whose accuracy can be shown to be

asymptotic in the Mach number, i.e.:

$$\frac{p_1}{p_0} \sim \mathcal{O}\left(Ma^2\right) \tag{2.9}$$

and employing an equation of state (e.g. ideal gas):

$$p_0 = \frac{\rho RT}{W} \tag{2.10}$$

Applying a material time derivative to the homogeneous pressure and expanding:

$$\frac{Dp_0}{Dt} = \frac{\partial p_0}{\partial t} = \frac{D\frac{\rho RT}{W}}{Dt} = \frac{RT}{W}\frac{D\rho}{Dt} + \rho RT\frac{D\frac{1}{W}}{Dt} + \frac{\rho R}{W}\frac{DT}{Dt} \tag{2.11}$$

From continuity:

$$\frac{D\rho}{Dt} = -\rho\left(\nabla \cdot \mathbf{u}\right) \tag{2.12}$$

thus:

$$\frac{\partial p_0}{\partial t} = -\frac{\rho RT}{W}\nabla \cdot \mathbf{u} + \rho RT\frac{D\frac{1}{W}}{Dt} + \frac{\rho R}{W}\frac{DT}{Dt} \tag{2.13}$$

Isolating the divergence of velocity:

$$\nabla \cdot \mathbf{u} = -\frac{W}{\rho RT}\frac{\partial p_0}{\partial t} + W\frac{D\frac{1}{W}}{Dt} + \frac{1}{T}\frac{DT}{Dt} \tag{2.14}$$

$$= -\frac{1}{p_0}\frac{\partial p_0}{\partial t} + W\frac{D\frac{1}{W}}{Dt} + \frac{1}{T}\frac{DT}{Dt} \tag{2.15}$$

From the definition of mean molecular weight:

$$W \equiv \sum_k X_k W_k \tag{2.16}$$

$$\frac{1}{W} \equiv \sum_k \frac{Y_k}{W_k} \tag{2.17}$$

thus:

$$\frac{D\frac{1}{W}}{Dt} = \frac{D}{Dt}\left(\sum_k \frac{Y_k}{W_k}\right) \tag{2.18}$$

$$= \sum_k \frac{1}{W_k}\frac{DY_k}{Dt} \tag{2.19}$$

combining with the species equation:

$$\frac{1}{W}\frac{D\frac{1}{W}}{Dt} = \frac{1}{\rho}\sum_k \frac{W}{W_k}\left(-\nabla \cdot \left[\rho Y_k \mathbf{V}_k\right] + \dot{\omega}_k\right) \tag{2.20}$$

replacing the material derivative of temperature with the energy equation (in temperature form):

$$\frac{1}{T}\frac{DT}{Dt} = \frac{1}{\rho c_p T}\frac{\partial p_0}{\partial t} + \frac{1}{\rho c_p T}\left(-\sum_k h_k\dot{\omega_k} + \nabla\cdot(\lambda\nabla T) - \left(\rho\sum_k c_{p,k}Y_k\mathbf{V}_k\right)\cdot\nabla T \right.$$
$$\left. +\boldsymbol{\tau}\cdot\cdot\nabla\mathbf{u} + \dot{Q} + \rho\sum_k Y_k\mathbf{f}_k\mathbf{V}_k\right) \quad (2.21)$$

combining all of these terms into the expression for the divergence of the velocity field:

$$\nabla\cdot\mathbf{u} = -\frac{1}{p_0}\frac{\partial p_0}{\partial t} + \frac{1}{\rho}\sum_i\frac{W}{W_k}\left(-\nabla\cdot[\rho Y_k\mathbf{V}_k] + \dot{\omega_k}\right) + \frac{1}{\rho c_p T}\frac{\partial p_0}{\partial t}$$
$$+\frac{1}{\rho c_p T}\left(-\sum_k h_k\dot{\omega_k} + \nabla\cdot(\lambda\nabla T) - \left(\rho\sum_k c_{p,k}Y_k\mathbf{V}_k\right)\cdot\nabla T + \boldsymbol{\tau}\cdot\cdot\nabla\mathbf{u} + \dot{Q} + \rho\sum_k Y_k\mathbf{f}_k\mathbf{V}_k\right) \quad (2.22)$$

where for many applications the thermodynamic pressure is steady and the time derivative of p_0 can be ignored.

Looking at the unsteady pressure term:

$$-\frac{1}{p_0}\frac{\partial p_0}{\partial t} + \frac{1}{\rho c_p T}\frac{\partial p_0}{\partial t} \quad (2.23)$$

$$= -\frac{1}{p_0}\frac{\partial p_0}{\partial t} + \frac{R}{p_0 c_p W}\frac{\partial p_0}{\partial t} \quad (2.24)$$

$$= -\frac{1}{p_0}\frac{\partial p_0}{\partial t}\left(1 - \frac{R}{p_0 c_p W}\right) \quad (2.25)$$

for an ideal gas:

$$c_p \equiv c_v + \frac{R}{W} \quad (2.26)$$

thus:

$$\frac{R}{W c_p} - \frac{c_p}{c_p} = \frac{c_v}{c_p} \quad (2.27)$$

$$\frac{R}{W c_p} - 1 = \frac{1}{\gamma} \quad (2.28)$$

The final form of the divergence of velocity:

$$\nabla \cdot \mathbf{u} = -\frac{1}{\gamma p_0}\frac{\partial p_0}{\partial t} + \frac{1}{\rho}\sum_k \frac{W}{W_k}\left(-\nabla \cdot [\rho Y_k \mathbf{V}_k] + \dot{\omega}_k\right)$$
$$+ \frac{1}{\rho c_p T}\left(-\sum_k h_k \dot{\omega}_k + \nabla \cdot (\lambda \nabla T) - \left(\rho \sum_k c_{p,k} Y_k \mathbf{V}_k\right) \cdot \nabla T + \boldsymbol{\tau} \cdot \cdot \nabla \mathbf{u} + \dot{Q} + \rho \sum_k Y_k \mathbf{f}_k \mathbf{V}_k\right) \tag{2.29}$$

As such the uniform thermodynamic pressure approximation (referred to as the low-Mach approximation, and whose error converges as the square of the Mach number as mentioned previously) is a constraint on the velocity divergence. By taking the divergence of the momentum field, an elliptic partial differential equation of Poisson type can be constructed for the dynamic pressure p_1 with a right-hand-side that depends on this velocity divergence. The enforcement of the constraint typically results in algorithms that are an extension of the projection method of Chorin (Chorin, 1968) for incompressible flows, which are fundamentally based on the principle of decomposing arbitrary vector fields into divergence free and gradient terms (Hodge-Helmholtz decomposition). Fractional step numerical schemes employing projections are thus naturally extendible to the solution of the low-Mach combustion problem (Lai et al., 1993; Day and Bell, 2000). The low-Mach formulation was initially proposed for combustion by Majda & Sethian (Majda and Sethian, 1985), and has been used in a variety of combustion simulation methodologies leveraging the operator splitting and fractional step type approaches originally developed for incompressible flows (Kim and Moin, 1985), ultimately resulting in highly elaborate splitting schemes to minimize splitting errors, e.g. spectral deferred corrections (Minion, 2004) as employed by Bell et. al. (Bell et al., 2007) for low-Mach number combustion.

A simple numerical solution approach to fractional stepping that is often employed for expediency (as an alternative to constructing and imposing the velocity divergence constraint explicitly) is to first integrate the momentum equation ignoring the pressure gradient (or in this context the dynamic pressure gradient) to generate an intermediate momentum field $(\rho\mathbf{u})^*$ and then to integrate the momentum equation using a second step that includes the dynamic pressure gradient:

$$\frac{\partial \rho \mathbf{u}}{\partial t} = -\nabla p_1 \tag{2.30}$$

which will give the solution after a full time step, $(\rho\mathbf{u})^{n+1}$. Taking the divergence of Eq. 2.30 and using a simple finite difference for the time derivative of momentum:

$$\nabla^2 p_1 = \frac{1}{\Delta t}\left[\nabla \cdot (\rho\mathbf{u})^{n+1} - \nabla \cdot (\rho\mathbf{u})^*\right] \tag{2.31}$$

The intermediate momentum field $(\rho\mathbf{u})^*$ is known, but an approximation is required for the divergence of momentum at the unknown forward time step. By replacing this divergence using the continuity equation:

$$\nabla^2 p_1 = \frac{1}{\Delta t}\left[\left(\frac{\partial \rho}{\partial t}\right)^{n+1} - \nabla \cdot (\rho \mathbf{u})^*\right] \tag{2.32}$$

and approximating the unknown future density time derivative by using a simple backward difference:

$$\left(\frac{\partial \rho}{\partial t}\right)^{n+1} \approx \frac{\rho^{n+1} - \rho^n}{\Delta t} \tag{2.33}$$

where the forward time density, ρ^{n+1}, is assumed to have been estimated separately through the time advancement of the equations for species mass densities (the sum of which at the forward time will equal ρ^{n+1} by definition), Eq. 2.32 is now closed and the solution for p_1 can be used to complete the second step of the momentum field integration. This procedure is typically embedded into a multi-stage predictor-corrector type explicit integrator in order to achieve accuracy. Although this method is simple overall, its range applicability is relatively limited as it can be shown to admit zeroth-order errors under some circumstances and it is not recommended for use in high-fidelity simulations where accuracy is desired.

For the grid spacings used in this work to resolve the spatial scales of reaction zones (≈7.2 μm) and assuming that the acoustic velocity scale is that for air (this work concerns lean fuel-air mixtures) at a temperature associated with the burned gas (e.g. at 2000 K, although for the case of instigated ignition this temperature can be much higher, the speed of sound in air is ≈1400 m/s), the characteristic time for information propagation by acoustic waves between grid points is approximately 5.5 ns. As such, when forced to resolve the time scales of chemistry due to the use of an explicit integration scheme (on the order of 1 ns), or the time scales of the application of an applied boundary condition (e.g. on the order of a few ns for discharges, or even smaller for the application of GHz frequency excitations in the case of microwave devices) the acoustic scale is also resolved and the use of a low-Mach projection would not deliver any improved performance over using the fully compressible formulation. Furthermore, severe time step restrictions are imposed on the required time step due to the dielectric relaxation time (see Section 3.1) which is the time scale at which perturbations of the electric potential decay due to collisions. As is discussed in Chapter 7, the time step employed in simulations when the fluid is subject to strong electric fields is on the order of 100 femtoseconds, which further compounds the argument against the unnecessary complexity and expense of employing a low-Mach formulation. As such the fully compressible formulation is used herein as the base fluid model for conducting simulations.

2.3 Electron energy

The electron energy is a parameter of interest primarily as it will determine the rates of important chemical reactions (see Chapter 4). At the level of theory employed in this work,

the rate constants for electron processes are determined using a 'local field approximation' (LFA), wherein the electron rates are expressed as functions of the local electric field and the equilibrium electron temperature is an additional result of the calculation which involves the determination of the electron energy distribution function (EEDF). Since at the level of the individual collisions (see Section 3.2) the interaction is mediated by the kinetic energies of the particles, and as such by the mean energy (in the fluid context), it is more appropriate to parametrize rates against electron energy (or temperature). This is precisely what is done for Arrhenius rates for the standard gas phase combustion reactions and represents a second order approximation relative to LFA. The latter approach is referred to as the 'local mean energy' assumption and requires the solution of a conservation equation for electron energy. As is discussed in Section 6.3, the time scales that are required to be resolved in order to represent transients of this electron energy equation are essentially intractable in the numerical framework employed in this work. LFA is known to be inaccurate under conditions of highly varying composition or electric field, and in Particle-in-Cell Monte Carlo simulations has been shown to under-predict ionization rates relative to the second-order model (Markosyan et al., 2015). For the simulations performed in this work the regions of high electric field (i.e. where the electron energy is expected to be high and the electron kinetics is expected to be most active) are essentially uniform, have an essentially uniform composition, and as such the relative simplicity of using LFA is justified.

2.4 Governing equations - two fluid model

To summarize, the governing equations of the two-fluid system modeled in this work are listed below (where 'e' refers to the electron species, which can potentially exhibit non-equilibrium behavior). Details on the specification of diffusion fluxes can be found in Chapter 3. The transport coefficients and rates of electron kinetic processes are functions of both the gas phase temperature (solved using the total energy equation) and the electron temperature, where the electron temperature is approximated using LFA in the context of approximation of the electron EEDF (see Section 4.3). As discussed in Section 4.2, the transport coefficients for neutrals and ions are treated using tabulated molecular potential data and calculated in the CHEMKIN transport framework.

$$\frac{\partial \rho Y_k}{\partial t} + \nabla \cdot \left(\rho Y_k \left[\mathbf{u} + \mathbf{V}_k\right]\right) = \dot{\omega}_k \tag{2.34}$$

$$\frac{\partial \rho \mathbf{u}}{\partial t} + \nabla \cdot (\rho \mathbf{u}\mathbf{u}) = \nabla \cdot \boldsymbol{\sigma} + \rho \sum_{k=1}^{M} Y_k \mathbf{f} \tag{2.35}$$

$$\frac{\partial \rho e_t}{\partial t} + \nabla \cdot (\rho \mathbf{u} e_t) = -\nabla \cdot \mathbf{q} + \nabla \cdot (\boldsymbol{\sigma}\mathbf{u}) + \rho \sum_{k=1}^{M} Y_k \mathbf{f}_k \left(\mathbf{u} + \mathbf{V}_k\right) + \dot{Q} \tag{2.36}$$

$$\mathbf{V}_{k\neq e} = -D_{k\neq e} \frac{\nabla \left(Y_{k\neq e} W\right)}{Y_{k\neq e} W} + \mu_{k\neq e} \mathbf{E} \tag{2.37}$$

$$n_e \mathbf{u}_e = -\mu_e n_e \mathbf{E} - D_e \nabla n_e \tag{2.38}$$

$$\varepsilon_0 \nabla \cdot \mathbf{E} = \rho_c \tag{2.39}$$

Chapter 3

Plasma dynamics

3.1 Plasma overview

Plasmas are often described as being the 'fourth' fundamental state on the temperature continuum of matter, characterized as an ionized gas with a considerable population of freely moving charge carriers maintaining global quasi-neutrality. Plasmas are ubiquitous in the cosmos (e.g our Sun, most stars), and by some estimates make up 99% of the matter in the visible universe. Plasmas can exist over a temperature range from 10-10^8 K and over a number density range of 10^3-10^{33} m^{-3}, which bridges the spectrum of cold rarefied interstellar plasmas to laboratory scale plasmas at closer to earth's atmospheric pressure, to the hot dense plasmas confined in stars and fusion reactor cores. At higher temperatures (e.g. those found in neutron stars) molecular nuclei begin to disintegrate leading to a new distinct state of matter. At the cold end of the temperature continuum, Bose-Einstein condensates and superfluids are also considered to be distinct states of matter, rendering the numbering system for the states of matter referred to in the first sentence of this chapter to be somewhat arbitrary. While the plasma state can be achieved by raising the gas temperature such that the mean energy of the gas molecules is sufficiently high to activate ionization processes through collisions (with the resulting ionization rate roughly balancing the recombination rate), plasmas can also be generated by energetic photons or the application of strong electric fields at low temperature as a means to liberate electrons from neutral molecules. Lower density plasmas are typically colder as the decreased collision frequency at low densities limits the recombination rate, allowing the plasma to be sustained at lower temperatures (i.e. with lower ionization rates). However, not all charged gases satisfy the definition of plasma and the distinction must be qualified by the precise behavior of the gas material in question. As quasi-neutrality holds approximately in plasmas, long range electrical forces tend to dominate short range forces and plasma fluids tend to exhibit a collective response on continuum scales to such long range forces.

Equilibrium ionization fractions in weakly-ionized plasmas can be predicted using the Saha-Langmuir ionization equation (Eq. 3.1, where the values g_0 and g_1 are the energy

degeneracies of neutral and ionized molecules respectively, written for the case of one level of ionization), which considers ionization from thermalization.

$$\frac{n_e^2}{N - n_e} = \frac{2}{\Lambda^3}\frac{g_1}{g_0}\exp\left(\frac{-\epsilon}{k_B T}\right) \tag{3.1}$$

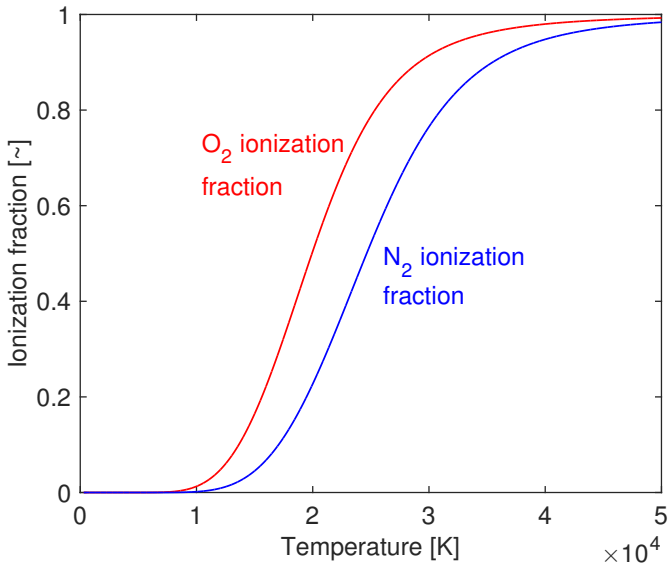

Figure 3.1: Ionization fractions predicted by the Saha-Langmuir ionization equation (Eq. 3.1).

Figure 3.1 shows the ionization fractions for molecular oxygen and nitrogen as a function of temperature, indicating that the ionization fraction is typically very low for the gases that comprise air at temperatures relevant to combustion (300-3000 K).

The prevalence of large scale collective motions in plasmas occurs as a consequence of damping of short-range forces within the plasma. The elimination of short range interactions arises due to a phenomenon referred to as shielding, which causes charge perturbations in the plasma to be locally neutralized by the motion of nearby charge. The displacement of charge in an otherwise homogeneous plasma establishes a polarization field that shields the rest of the plasma from the original charge perturbation. The domain of influence of the charge perturbation is restricted to within a length scale which is a function of the plasma temperature and density, referred to as the Debye length (see Section A.3 for a derivation of this scale):

$$\lambda_D = \sqrt{\frac{\varepsilon_0 k_B T_e}{e^2 n_{e0}}} \tag{3.2}$$

The Debye length is the limiting length scale for features of the potential field within the plasma, and the criterion for plasma behavior (i.e. the existence of large scale collective

motions) is that the length scale (or 'size') of the plasma itself be much larger than this characteristic length.

In the absence of collisional damping, plasmas are constantly in motion. Charge displacements in a homogeneous plasma will result in a restoring force toward the equilibrium position corresponding to neutrality. Without collisions, the induced motion will be simple harmonic in character due to the the fact the charge carriers possess inertia. The characteristic frequency of the oscillatory motion will depend on the plasma density and the inertial mass. This frequency is referred to as the plasma frequency (see Section A.2 for a derivation of this scale) and for electron plasmas is written as:

$$\omega_p = \sqrt{\frac{n_e e^2}{m_e \varepsilon_0}} \tag{3.3}$$

This scale represents the frequency of standing waves within the plasma (i.e non-propagating Langmuir waves) and its inverse is the fastest time with which the plasma can respond to charge displacement. As such, homogeneous, quiescent (i.e. no bulk motion) plasmas are typically never completely still as can be the case for regular gases, but rather 'quiver' at their plasma frequency. These fluid plasma waves are analogous to plasmons in the context of condensed matter physics.

For collisional plasmas, charge oscillations will decay due to collisions. The relevant time scale for a charge oscillation to decay (and as such the time scale for the potential field to reach local equilibrium) is the dielectric relaxation time (see Section A.4 for a derivation of this scale):

$$\tau_d = \frac{\nu_{en}}{\omega_p^2} \tag{3.4}$$

3.2 Collisions in plasmas

In contrast to collisions between uncharged particles, collisions between charged particles are not well represented by a simple hard-sphere type model conforming to Lennard-Jones type intermolecular potentials. At distances much further than those where Pauli repulsion becomes relevant, charged particle pairs (e.g. electron and ion) will begin to feel the influence of each other's smoothly varying Coulomb potential (varying as r^{-1}). As such, the interaction time between the collision partners is a relevant parameter as the collision is much less instantaneous than in the neutral-neutral case. Charged particle collisions also tend to result in scattering with smaller scattering angles than for the neutral-neutral case as collisions tend not to be 'head on', rather more massive particles modify the trajectory of the lighter particle in a direction dependent on the sign of the charge on each particle. Figure 3.2 shows the schematic of a collision and resultant scattering between an electron and a positron. In the frame of the positron, the electron will scatter towards the positron center of mass due to the decreasing potential with scattering angle χ, whereas for the case of an electron-electron

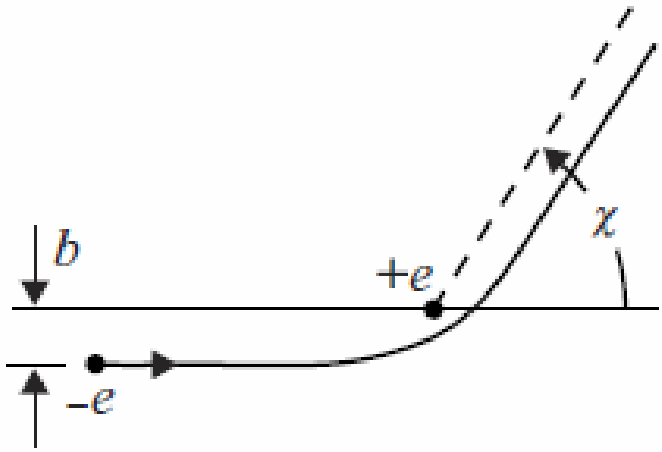

Figure 3.2: Electron scattering as a result of a collision with a charged particle (Gurnett and Bhattacharjee, 2005).

collision the approaching electron would scatter outwards. The scattering angle will be mediated by the interaction time, as this is the time that the approaching electron interacts with the potential field of its collision partner. A consequence of this is that the scattering angle will decrease with an increasing approach velocity. In other words, the collision cross section of the collision event (essentially a metric for describing the probability of a collision) will decrease with increasing approach velocity, or equivalently, increasing kinetic energy. In the fluid framework, this collision kinetic energy is the definition of temperature when considering an ensemble of particles. The principle of decreasing (or varying) collision cross section with temperature is not restricted to collisions between charged particles with other charged particles, but also extends to the collision of charged particles with neutrals since the electron is of sufficiently small mass to be sensitive to the charges in the neutral molecules outer shell at longer distances than a relatively massive neutral molecule would be. Since collisions between charged particles (i.e. electrons) is the plasma kinetic process relevant to this work, the collision cross section between electrons and neutrals for a variety of processes is of interest. Table 4.1 shows data for the collision cross section of electrons with atomic oxygen for the first ionization reaction. The cross section is zero below the ionization potential (12.06eV), rises to a maximum at 15eV and then begins to fall. The fall in collision cross section can be attributed to the fact that the energetic electron travels past the O_2 molecule so rapidly that there is less time for any effective interaction to take place.

As mentioned previously, electron collisions are dominated by interactions with neutral molecules due to the abundance of neutrals in weakly ionized plasmas. These collisional interactions can result in ionization, impact dissociation, neutral excitation, attachment (to form a negative ion), charge exchange (where an outer shell electron from a neutral molecule jumps to a positive ion, neutralizing it while forming a new positive ion), and elastic transfer

(where no chemical interaction takes place but momentum and energy are transferred) to name a few. Elastic collisions are of interest as they are common and determine the transport properties of the electron fluid.

A simple electron elastic collision model which will be used implicitly in this work to define the drag force experienced by electrons through collisions with neutrals is the Lorentz model. Following Gurnett (Gurnett and Bhattacharjee, 2005), the Lorentz model assumes that on average, electron scattering from fixed neutral scattering centers is isotropic, meaning that on average the effect of scattering is to produce an impulse equal to the negative of the electron momentum (since the average momentum of the collision partners after a collision is zero). The collision operator in the momentum equation for the electron fluid becomes:

$$\frac{\delta \mathbf{p}_c}{\delta t} = \nu_{en} \int_V -m_e \mathbf{v} f_s d^3 v \tag{3.5}$$

where the integration is over velocity phase space and f_s is the electron distribution function in velocity-position phase space, resulting in the Lorentz collision model which acts as a sink in the electron momentum equation:

$$\frac{\delta \mathbf{p}_c}{\delta t} = -\nu_{en} m_e n_e \mathbf{u}_e \tag{3.6}$$

3.3 Electric discharges

Electric discharges are common occurrences both in nature and in engineering applications. Large scale arc discharges between clouds and the earth's surface (lightning) occur globally at a frequency of approximately 10 Hz, while small scale arc discharges occur at frequencies on the order of 1000s of Hz in every spark ignited engine in operation, and are relied upon as a well behaved source of ignition. Figure 3.3 shows a qualitative i-v curve partitioning various discharge phenomena into a regime diagram for gases confined between boundary electrodes across which voltages are applied. Initially, for vanishingly small applied voltages, any current present in the gas arises from the motion of electrons and ions produced by background radiation sourced from cosmic rays or materials emitting small amounts of radiation. This radiation ionizes neutral molecules and produces a small pool of charged particles even in the case of zero applied voltages. The application of a voltage will cause this charge to migrate towards the electrodes resulting in a small current. Increasing the applied voltage will cause the charge to be swept towards the electrodes more rapidly, increasing the effective current. At some point the rate at which charge is removed from any particular location in the domain due to the action of the applied voltage will equal the rate at which it is replaced by charge generated from the radiative ionization sources. This condition is referred to as saturation and the corresponding current is the saturation current, with no further increases in current observed for increasing applied voltages.

If the voltage is continuously increased in the saturation regime, a point will be reached where the current begins to increase once again. This increase is due to electrons gaining

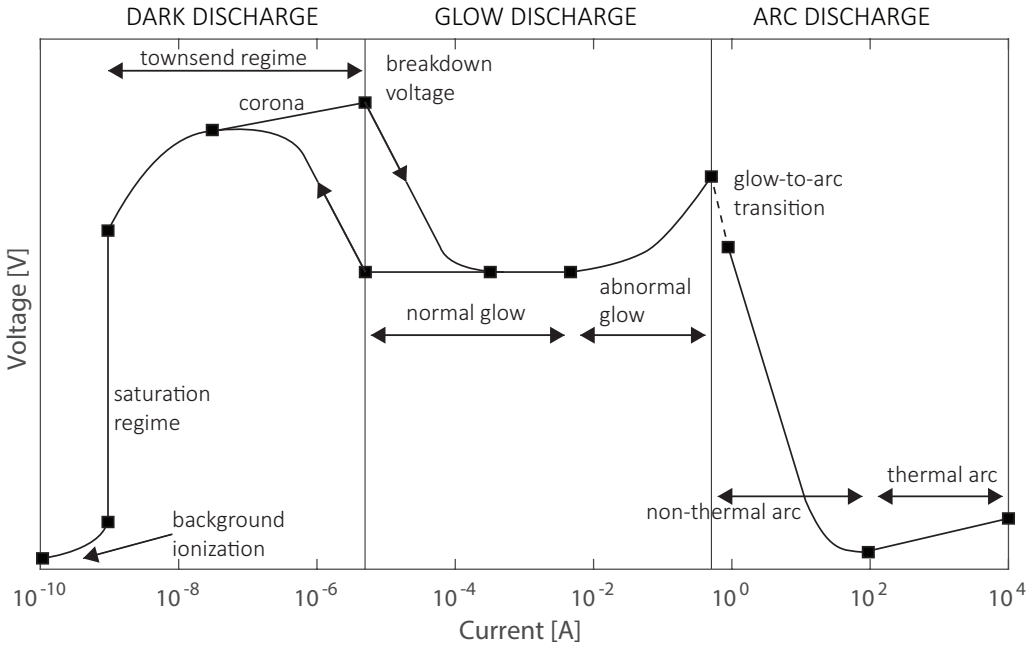

Figure 3.3: Electric discharge schematic adapted from Leal-Quirós (2004)

sufficient energy to activate kinetic processes such as electron impact ionization reactions which result in the generation of ions and secondary electrons which are subsequently transported by the electric field towards the relevant electrodes, contributing to the current flow. The ionization rate increases exponentially with voltage as does the resulting current, as the secondary electrons generated from the primary ionization events can themselves take part in further ionization reactions resulting in electron avalanche (Townsend discharge), i.e. an ionization chain reaction process.

The regimes discussed previously are all observed to occur in a 'dark' mode, such that there is essentially no visible signature of the current or the electron avalanche process. As the voltage and current increases, and as a result the density of electrons and their energy increases, electron kinetic processes that result in the electronic excitation of neutral molecules become more prevalent, with associated photon emission on de-excitation. While such excitation and de-excitation processes are too seldom to generate a globally significant level of photon emission, at boundaries and at regions of sharp changes in geometry the local electric field can be high enough to cause ionization and excitations that are visible to the human eye. This strongly local mode of discharge is referred to as a corona, and can be observed in nature in the vicinity of sharp geometric features in an electric field (e.g. St. Elmo's Fire occurring on the masts of ships due to the buildup of static charge), characterized by a weak purple glow for air plasmas due to the frequencies associated with

electronic de-excitation of N_2 (blue) and O_2 (red) in air, dominated by the presence of N_2.

Further increase in voltage up to a critical value will result in an electrical breakdown, which causes a large abrupt drop in the electrical resistance of the conducting gas, resulting in a discontinuous orders of magnitude increase in current.

After breakdown has occurred, the current (and as such the electron density) is sufficiently high to cause a sustained level of electronic excitation of the neutral molecules throughout the domain with associated de-excitation and photonic emission. This regime is characterized as the glow discharge regime, as the plasma is globally luminescent and 'glows' with light at a wavelength determined by the energy of the emitted photons. By varying the gas composition within a device operating in the glow discharge regime a variety of wavelengths can be achieved by leveraging the varying excitation energies of molecules comprising the mixture, with such devices being used in a variety of commercial lighting applications using inert gases such as argon, neon, krypton, and xenon to generate a spectrum of desired colors. At the onset of the glow discharge regime (normal glow), the plasma occupies a small area of the negatively charged electrode and the current increases by covering more cathode area as the plasma 'grows' at constant charge density and essentially constant voltage. Once the negative electrode is covered with plasma, further increases in current require increases in voltage (abnormal glow).

As the plasma interacts with the boundary electrodes, an arc is finally achieved when the electrons bound in the solid material become sufficiently energetic to overcome the work function of the material (i.e. the energy required to remove an electron from a solid to a point immediately outside the solid surface) and contribute to the overall current under the action of the applied potential. This electron liberation process is driven by thermionic and field emission occurring at the boundaries of the solid material.

3.4 Charged species transport

The governing transport equations for conserved quantities in fluid mixtures (reacting or non-reacting) are essentially an aggregation of a family of transport equations for each species, with the aggregated conserved variables typically being associated with transport at the center of mass velocity of a fluid sub-volume. The transport of a conserved quantity relative to that velocity results in the invocation of concepts such as mass diffusion, bulk thermal conductivity (for energy transport), and bulk viscosity (for momentum transport) using some sort of mixture averaging to define bulk material properties of the mixture. Such approaches invariably rely on assumptions such as local thermodynamic equilibrium in order to define such properties of mixtures. However, in the context of applied electric fields and charged species, it is possible that strong electric fields can cause such assumptions to break down and that the mixture can potentially support multiple temperatures. In this case one is forced to derive individual conservation equations for possible non-equilibrium components (e.g. using moments of the Boltzmann kinetic equation) and couple these equations to the bulk mixture equations. For example, we can consider the electron fluid momentum equation,

since the electron fluid is the species that is expected to be the first sub-fluid to exhibit non-equilibrium behavior within the mixture due to the large charge-to-mass ratio of the electron. The dynamics of electrons are typically not treated in their unsteady form when using fluid equations, rather a zero-inertia approximation for electrons is often invoked which results in the drift-diffusion approximation for the electron number flux:

$$n_e \mathbf{u}_e = -\mu_e n_e \mathbf{E} - D_e \nabla n_e \tag{3.7}$$

where for simplicity an electron mass diffusion coefficient has been generated by assuming that the electron temperature field is approximately uniform on the scale of the electron density and subsequently invoking the Einstein relation (see Section A.5 for derivation) for the diffusion of charge particles.

In the context of coupled multi-component diffusion in mixtures, this classical drift diffusion flux can be invoked after some simplifications. Starting from the expression presented by Williams (Williams, 1958) using the approach of Furry (Furry, 1948), presenting the forces that drive molecular diffusion in the sense that they support scalar gradients:

$$\nabla X_k = \sum_{j=1}^{M} \frac{X_k X_j}{D_{ij}} \left(\mathbf{V}_j - \mathbf{V}_k\right) + \left(Y_k - X_k\right) \frac{\nabla p}{p} + \frac{\rho}{p} \sum_{j=1}^{M} Y_k Y_j \left(\mathbf{f}_k - \mathbf{f}_j\right) \tag{3.8}$$

For most scenarios in combustion the effect of differential body forces are neglected, but must be retained here due to the importance of Coulomb forces in plasmas (albeit with the coupling neglected). Invoking the Hirschfelder-Curtiss approximation (Hirschfelder et al., 1954) to neglect the coupling of diffusion velocities, and introduce unary mixture averaged diffusion coefficients:

$$\nabla X_k = -\frac{X_k \mathbf{V}_k}{D_k} + \left(Y_k - X_k\right) \frac{\nabla p}{p} + \frac{\rho}{p} Y_k \mathbf{f}_k \tag{3.9}$$

Isolating the flux term $Y_k V_k$ by transforming from mole fractions to mass fractions using $Y_k = X_k \frac{W_k}{W}$:

$$Y_k \mathbf{V}_k = -D_k \frac{W_k}{W} \left(\nabla X_k + \left(Y_k - X_k\right) \frac{\nabla p}{p} + \frac{\rho}{p} Y_k \mathbf{f}_k \right) \tag{3.10}$$

Neglecting the pressure gradient component of the flux in this treatment:

$$Y_k \mathbf{V}_k = -D_k \frac{W_k}{W} \left(\nabla X_k + \frac{\rho}{p} Y_k \mathbf{f}_k \right) \tag{3.11}$$

By specifying the body force to be the Coulomb force associated with the electric field, and invoking the Einstein relation for the diffusion of charged particles:

$$Y_k \mathbf{V}_k = -D_k \frac{\nabla \left(Y_k W\right)}{W} + \mu_k Y_k \mathbf{E} \tag{3.12}$$

The contribution of Coulomb forces is an additive drift flux and is similar to the form of the single species drift diffusion equation (Eq. 3.7), albeit achieved without explicitly invoking a zero-inertia approximation (although drift-diffusion character is assumed through the use of the Einstein relation) and as such is appropriate for specifying diffusion fluxes for heavy charged species such as ions. This form is employed in the plasma fluid solver developed in this work, with strict mass conservation (lost due to the relaxation of coupling when invoking the Hirschfelder-Curtiss type approximations) enforced using a correction velocity treatment, as detailed in text of Poinsot (Poinsot and Veynante, 2005).

Boundary conditions for charged species at solid boundaries become complicated due to the fact that secondary ionization processes can take place in the solid material. Boundary conditions of the form employed by Mahadevan & Raja (Mahadevan and Raja, 2010) are typically used in simulations where electron emission occurs at solid electrodes, however in this work the boundaries are considered to be fluid and such additional charge generation processes are ignored at boundaries.

Chapter 4

Plasma kinetics

4.1 Chemical kinetic models

At low values of electric field, or more relevantly low values of reduced electric field (E/N), electrons are in thermal equilibrium with neutral molecules (and by extension ions) due to insufficient time for electrons to accelerate between collisions. As the reduced electric field is increased either by increasing the electric field (so as to accelerate electrons between collisions) or by decreasing the neutral species number density, (to reduce the collision frequency) electrons gain sufficient kinetic energy such that on collision with neutrals (where some of their energy is lost and the remainder is essentially randomized), their mean energy is higher than their neutral counterparts. When electrons are energized, a variety of processes are activated that effectively create new pathways in the chemical system.

Charge is liberated from neutral molecules by ionization processes and one of these routes can be purely chemical in nature occurring at low E/N. Chemi-ionization is a process wherein "species undergo a chemical rearrangement that releases sufficient energy to ionize one of the products" (Lawton and Weinberg, 1969), and forms the basis for electron production in flames at low values of electric field. The chemi-ionization mechanism follows:

$$CH + O \longrightarrow HCO^+ + e^-\text{: Chemi-ionization} \tag{4.1}$$
$$HCO^+ + H_2O \longrightarrow H_3O^+ + CO\text{: Proton transfer} \tag{4.2}$$
$$H_3O^+ + e^- \longrightarrow H_2O + H\text{: Electron-ion recombination (exothermic)} \tag{4.3}$$
$$H_3O^+ + e^- \longrightarrow OH + 2\,H\text{: Electron-ion recombination (exothermic)} \tag{4.4}$$
$$H_3O^+ + e^- \longrightarrow H_2 + OH\text{: Electron-ion recombination (exothermic)} \tag{4.5}$$
$$H_3O^+ + e^- \longrightarrow O + H_2 + H\text{: Electron-ion recombination (exothermic)} \tag{4.6}$$

After chemi-ionization (Eq. 4.1), the transition ion (HCO^+) reacts rapidly to form H_3O^+ (Eq. 4.2). Equations 4.3-4.6 are exothermic recombination reactions that generate reactive radicals that will in principle aid with fuel decomposition and heat release.

Energy (eV)	Cross section (m^2)
1.206e+1	0.000e+0
1.300e+1	2.300e-22
1.800e+1	2.000e-21
2.800e+1	7.400e-21
3.800e+1	1.320e-20
4.800e+1	1.800e-20
5.800e+1	2.100e-20
6.800e+1	2.330e-20
7.800e+1	2.500e-20
8.800e+1	2.600e-20
1.000e+2	2.700e-20
1.500e+2	2.700e-20
2.000e+2	2.500e-20
3.000e+2	2.170e-20
5.000e+2	1.660e-20
7.000e+2	1.350e-20
1.000e+3	1.040e-20
1.500e+3	7.600e-21
2.000e+3	6.000e-21
3.000e+3	4.200e-21
5.000e+3	2.700e-21
7.000e+3	2.000e-21
1.000e+4	1.400e-21

Table 4.1: Collision cross sections for O_2 ionization by electron impact. Note that the first entry corresponds to the first ionization potential of O_2, 12.06eV.

The two-temperature (i.e. parameterized by the temperature of the bulk gases and the electrons) methane-air plasma mechanism used in this work is built upon the GRI-Mech 3.0 methane-air mechanism (Smith et al., 1999). Ion chemistry pathways containing thermal electrons are added following the mechanism of Prager (Prager et al., 2007). The rates of inelastic electron impact reactions, resulting in the decomposition of neutral molecules, ionizations, and excitations, are precomputed using a representative lean unreacted methane-air mixture and parameterized by the electron temperature in the CHEMKIN framework using Janev, Langer, Evans, and Post (Janev et al., 1987) fits (see Eq. 5.13). Using a representative lean mixture to pre-calculate the rates is justified by the fact that electron/neutral interactions that control the overall evolution of the system are expected to take place in the fresh gas only, where the electron temperature is sufficiently high. Collision cross section data for these electron neutral interactions are obtained from the LXCat database (Pancheshnyi

et al., 2012; DeFilippo, 2013). Mechanism reduction is performed using ignition delay targets via the Targeted Search Algorithm (TSA) (Tham et al., 2008) for lean methane-air mixtures at 300K, 1atm, using a variety of initial electron densities and electric fields, thus reducing the detailed mechanism from 106 species and 2141 reactions to 45 species and 514 reactions. The mechanism, including ground state and excited neutral species, e.g. $N_2(B_3)$, $N_2(C_3)$, $N_2(a')$, $O_2(a^1)$, $O(^1D)$, electron, and several ions, e.g. $CH_4{}^+$, $O_2{}^+$, $O_2{}^-$, $N_2{}^+$, HCO^+, H_3O^+, can be found in Appendix C.

4.2 Thermodynamic and transport data

The thermodynamics of excited state species are sourced from the database of Burcat (Burcat and Ruscic, 2005), where the energy stored in the additional activated energy modes (i.e. electronic, vibrational) are included. Transport properties for excited states are assumed to be identical to their ground state equivalents due to a lack of available data for electronic state intermolecular potentials. The transport data for all species (apart from the electron) are sourced from the CHEMKIN transport database (Kee et al., 1986).

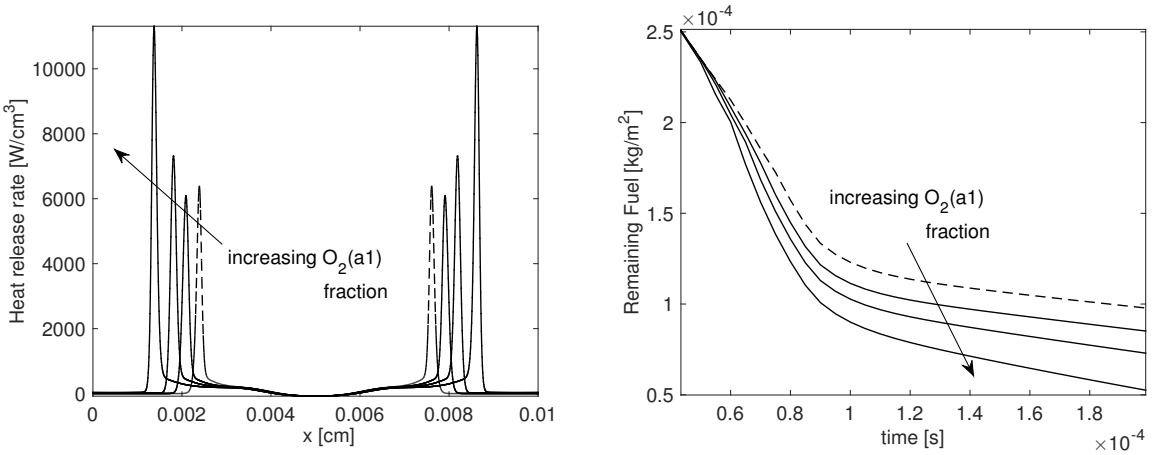

(a) (b)

Figure 4.1: Flame kernel size at equivalent times (a) and mass of unburned fuel (b) for increasing initial fractions of electronically excited O_2 (in the $O_2(a^1)$ state) .

However, the determination of the modified intermolecular potentials accounting for excitation is possible by performing ab-initio calculations of long-range dispersion reactions, e.g. using Restricted Open-Shell Hartree-Fock theory with Configuration Interaction to solve for approximate wave functions. Numerical simulations to approximate these wave function using the GAMESS solver (Schmidt et al., 1993) for an electronically excited state of molecular oxygen, $O_2(a^1)$, performed by Pineda (Pineda and Chen, 2016) and used to determine updated Lennard-Jones parameters for flame simulations at reduced pressure (0.03 atm),

showed that small discrepancies in flame speeds can be observed relative to simply using the ground state data. Figure 4.1 shows the effect of changing the $O_2(a^1)$ fraction in planar ignition simulations. $O_2(a^1)$ is a more reactive form of O_2 and increasing fractions result in more rapidly flame development and fuel consumption. The transport data generated by Pineda was used in repeated simulations of the cases shown in Fig. 4.1 (which are performed at atmospheric pressure) and the differences were found to be negligible for all excited state densities employed, and are most likely insignificant within the uncertainty of any of the models employed, and as such the use of ground state transport data for the excited states is a justifiable approximation.

Ion mass diffusion also differs from neutral diffusion through the different intermolecular potential presented by ions due to their charge. A Lennard-Jones or Stockmayer type potential may not necessarily be suitable for representing the potential field of an ion. Various modified potentials have been proposed and an (n-6-4) type interaction potential using the ion polarizability as a parameter has been investigated in the context of laminar flames (Han et al., 2015). The updated transport parameters were found to only have a small effect on the ion profiles. In the simulations performed in this work the intermolecular potential parameters for ions are set to be the same as those for the equivalent neutral molecule.

4.3 BOLSIG+

In order to estimate the electron EEDF, a freely available third party Boltzmann equation solver is employed, BOLSIG+ (Hagelaar and Pitchford, 2005). The capabilities of the BOLSIG+ library are conveniently accessed using a FORTRAN interface module, ZDPLASKIN (Pancheshnyi et al., 2008), that allows for straightforward deployment in CFD solvers.

$$\frac{\partial f}{\partial t} + \mathbf{v} \cdot \nabla_{\mathbf{x}} f - \frac{e}{m} \mathbf{E} \cdot \nabla_{\mathbf{v}} f = C\left[f\right] \tag{4.7}$$

The conceptual treatment used in BOLSIG+ is developed here briefly, as in order to make such simulations tractable the Boltzmann formulation for electron phase space density (Eq. 4.7) must be simplified somewhat. The left hand side of Eq. 4.7 represent unsteadiness, the transport of density, and the influence of external forces, while the right-hand-side accounts for collisional processes that augment the distribution by potentially adding or removing electrons from different regions of the distribution space. External forces are assumed to arise from external electric fields only, the external electric field and the collision cross sections of electron-neutral interactions (e.g. Fig. 4.2) are assumed to be spatially uniform on the length scale of the collisional mean free path, and the EEDF is assumed to vary in the direction of the electric field only (denoted as 'z'). Transforming the velocity into spherical coordinates (Eq. 4.8) delivers a formulation for the evolution of f depending on three rather than six phase space coordinates, namely electron velocity magnitude (v), the angle between the electron velocity vector and the applied electric field (θ), the position along the field (z), and finally also the time dimension. A typical strategy for solving (Eq. 4.8) is to

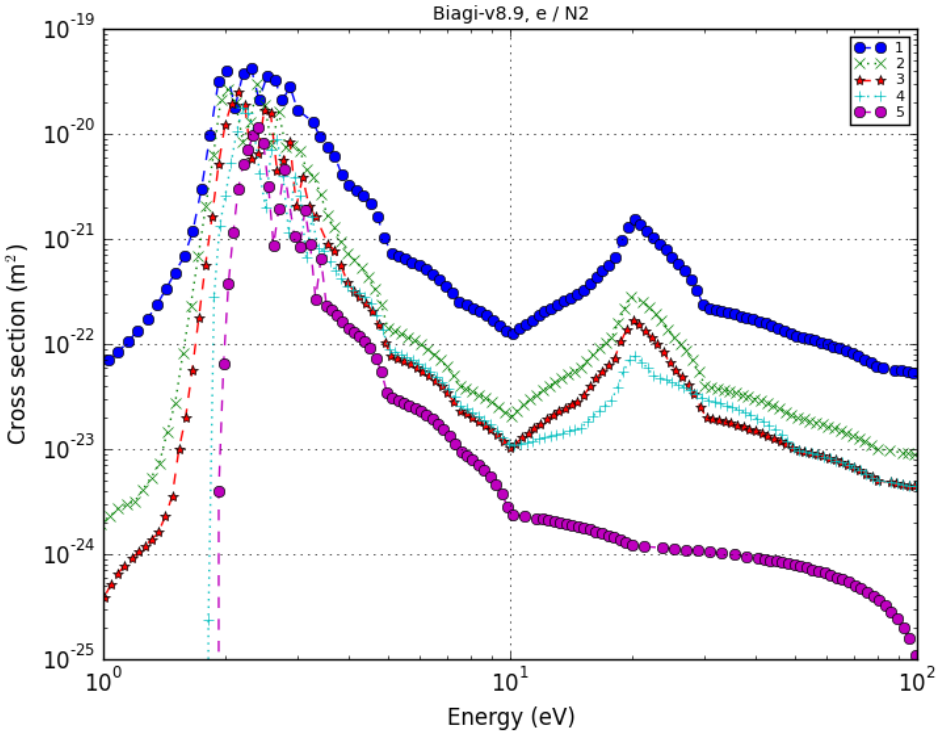

Figure 4.2: Electron collision cross sections for collisions with the first five vibrationally excited states of N_2

decompose the distribution function into an isotropic component (i.e. independent of θ) and a perturbative component, using the so-called two-term expansion in Legendre polynomials of cosθ (Eq. 4.9), and to solve equations for the expansion coefficients. This approach is known to break down for large values of reduced electric field when the distribution function becomes highly anisotropic.

$$\frac{\partial f}{\partial t} + v cos\theta \frac{\partial f}{\partial z} - \frac{e}{m} E \left(cos\theta \frac{\partial f}{\partial v} + \frac{sin^2\theta}{v} \frac{\partial f}{\partial cos\theta} \right) = C\left[f\right] \tag{4.8}$$

$$f\left(v, cos\theta, z, t\right) = f_0\left(v, z, t\right) + f_1\left(v, z, t\right) cos\theta \tag{4.9}$$

By substituting the two-term expansion (Eq. 4.9) into Eq. 4.8, multiplying in turn by the first two Legendre polynomials (1 and cosθ) and integrating over cosθ, expressions for each of the expansion coeffients are obtained (Eqs. 4.10, 4.11):

$$\frac{\partial f_0}{\partial t} + \frac{\gamma}{3} \varepsilon^{1/2} \frac{\partial f_1}{\partial z} - \frac{\gamma}{3} \varepsilon^{-1/2} \frac{\partial}{\partial \varepsilon} \left(\varepsilon E f_1 \right) = C_0 \tag{4.10}$$

$$\frac{\partial f_1}{\partial t} + \gamma\varepsilon^{1/2}\frac{\partial f_0}{\partial z} - E\gamma\varepsilon^{1/2}\frac{\partial f_0}{\partial \varepsilon} = -N\sigma_m\gamma\varepsilon^{1/2}f_1 \tag{4.11}$$

where the constant $\gamma = \left(\frac{2e}{m_e}\right)^{1/2}$, ε is the electron energy (i.e. translational thermal energy) in electronvolts (eV), N is the neutral species number density, and σ_m is the total momentum-transfer collision cross section defined as:

$$\sigma_m = \sum_r X_r\sigma_r \tag{4.12}$$

summed over all possible collision processes denoted by the dummy-variable 'r'. C_0 encapsulates change due to collisional processes.

While the distribution function is inherently temporally and spatially variable, we are ultimately interested in some representation of the electron distribution in energy space at a single location at a single instant. In order to filter spatial and temporal variation from the representation of the EEDF, a simple decomposition is proposed to separate out the energy dependence (Eq. 4.13):

$$f_{0,1}(\varepsilon, x, t) = \frac{1}{2\pi\gamma^3}F_{0,1}(\varepsilon)\, n(z,t) \tag{4.13}$$

such that such temporal and spatial variations are entirely attributed to the variation of the electron number density itself. $F_{0,1}$ are then the uniform steady representations of the isotropic and perturbative parts of the EEDF. Substitution of this decomposition into Eqs. 4.10, 4.11, along with an appropriate approximation for the time variation of the electron number density as a function of collisional processes that produce or consume electrons (such as ionization and attachment) an explicit dependence of F_1 on F_0 is arrived at in the limit of neglecting the spatial variation of electron number density. An expression for F_0 can also be derived which takes the form of an advective-diffusive-reactive equation in electron energy space, taking the form:

$$\frac{\partial}{\partial\varepsilon}\left(\tilde{W}F_0 - \tilde{D}\frac{\partial F_0}{\partial\varepsilon}\right) = \tilde{S} \tag{4.14}$$

where $\tilde{W}$ and $\tilde{D}$ are transport coefficients comprising combinations of constants and moments of the approximate isotropic distribution F_0, and $\tilde{S}$ is a reaction term dependent on the collision cross sections and threshold energies of various collisional processes. The precise formulation can be found in detail in the original seminal paper by Hagelaar and Pitchford (Hagelaar and Pitchford, 2005). Thus, by supplying information about local conditions such as the gas phase temperature, reduced electric field, and mixture composition along with a set of relevant collisional processes (represented by collision cross sections) an estimate for the local EEDF can be computed.

Once an approximation for the EEDF has been obtained, the rate constants of chemical reactions can be obtained by convolution of the electron energy dependent collision cross sections with the EEDF:

$$k = \left(\frac{2e}{m_e}\right)^{\frac{1}{2}} \int_0^\infty \varepsilon\sigma\left(\varepsilon\right) f\left(\varepsilon\right) d\varepsilon \tag{4.15}$$

4.4 Energy exchange

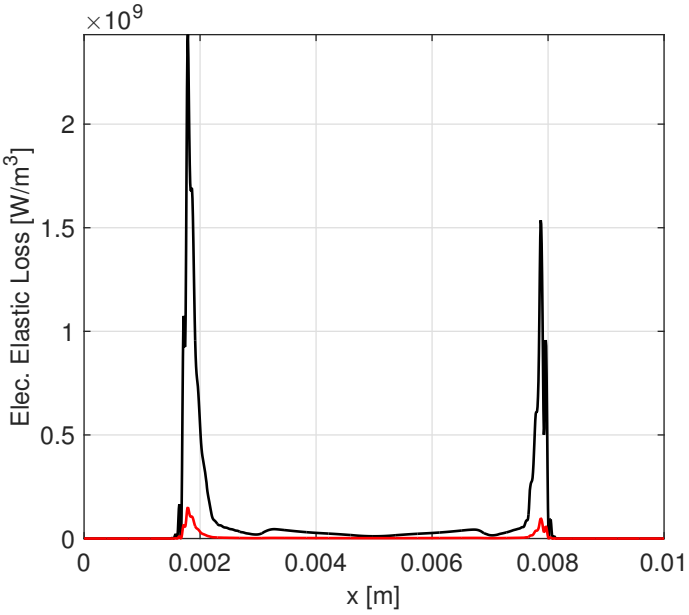

Figure 4.3: Electron elastic loss modeling. The black curve represents the streaming Maxwellian interaction model while the red curve employs the model used by BOLSIG+.

While not responsible for the progress of any chemical processes, elastic collisions between electron and neutral molecules result in momentum and thermal energy transfers. For non-thermal electrons, energy transfer is a complicated process as it involves the interaction between fluids with differing energy distributions. Simplified models for energy transfer can be derived by assuming that particle interactions (in the context of their underlying distributions) can be represented as a Markov process. Following Gurnett (Gurnett and Bhattacharjee, 2005) the collision integral of the Boltzmann kinetic equation can be represented using such probabilistic assumptions to arrive at the Fokker-Planck equation. In the framework of Fokker-Planck, a dynamical friction vector representation of the collision integral coupled with the assumption that the energy distributions of the partner molecules are Maxwellians (Hinton, 1983), allows for an analytic representation of the elastic energy exchange. This approach certainly involves a cascade of drastic simplifications, in particular the approximation that the electron energy distribution is Maxwellian, but still this approach is commonly used in the plasma literature (Nitschke and Graves, 1994; Hammond et al., 2002; Surendra and Dalvie, 1993; Nagaraja et al., 2013; Colella et al., 1999). The

generality of the simplifications are such that the analytic expression is used as a model across a vast range of scales, having been employed not only in the context of laboratory scale plasmas, but also for interstellar plasmas when approximating the energy interactions of star clusters (Spitzer Jr, 1940).

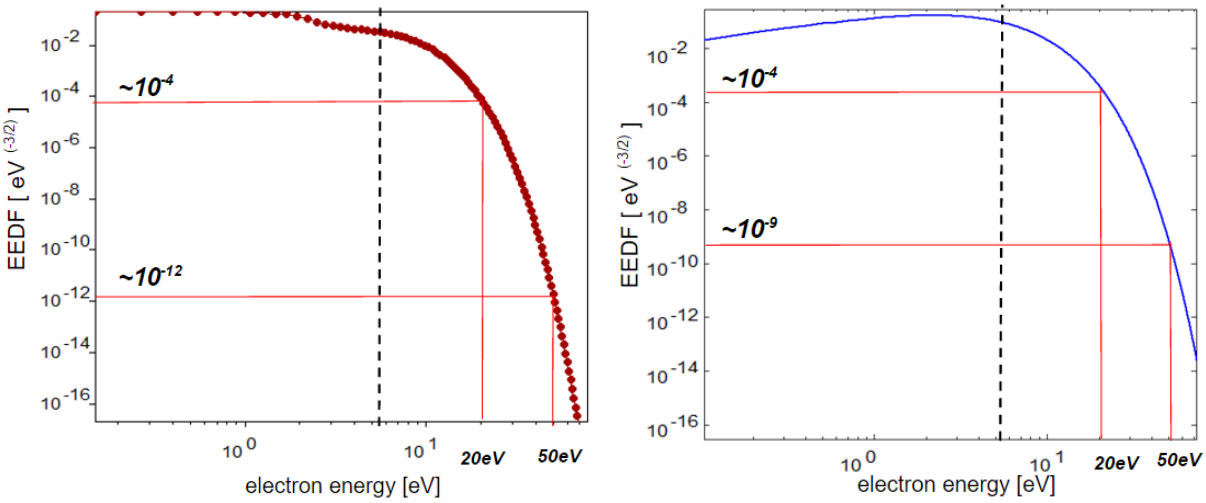

(a) BOLSIG+ calculated EEDF (b) Maxwellian EEDF

Figure 4.4: BOLSIG+ EEDF (a) and Maxwellian EEDF (b) for equivalent mean energies

Assuming streaming energy Maxwellian distributions, the elastic energy exchange rate is written as:

$$3\frac{N_A m_e}{W} n_e k_B \nu_{en} \left(T_e - T\right) \tag{4.16}$$

which is linear in the temperature difference between the species temperatures (aggregated over all fluids to generate a single expression assuming bulk fluid thermal equilibrium).

In contrast to the above simplified expression, when access to the EEDF is available an expression that takes into account the non-Maxwellian character of the electron energy can be used. In the process of determining the EEDF the energy transfer from electron to neutral gases at all energies must be accounted for, with the total energy loss (as calculated by the BOLSIG+ solver) being:

$$\sum_k X_k \frac{\left(2em_e\right)^{1/2}}{m_k} \int_0^\infty \sigma_k \varepsilon^2 F_0 d\varepsilon \tag{4.17}$$

and involves integration over all the energies represented in the EEDF.

Comparison of the performance of both models to investigate their discrepancy in the context of the plasma solver developed in this work is shown in Fig. 4.3 for a single instance of an applied electric field acting on a planar ignition problem (see Chapter 7). It is thus apparent that the simplified model using the streaming Maxwellian assumption predicts a

much higher energy transfer rate (i.e. electron energy loss) than the model using the approximate EEDF, which may lead to excessive bulk gas heating. This outcome can potentially be explained by comparing the shape of the EEDFs employed in each model. Figure 4.4a shows the EEDF as calculated by BOLSIG+ for a representative mixture subjected to an applied electric field and Fig. 4.4b shows the corresponding Maxwellian EEDF with both distributions having the same mean energies (both shown on log scales). By looking at the densities toward the higher energies for both cases, it appears that the Maxwellian EEDF preferentially assigns density to the higher energies compared to the calculated EEDF. This result may be responsible for excessive distribution integrated energy transfer as the Maxwellian case implicitly results in a higher density of highly energetic electrons allowing for more heat transfer relative to the calculated EEDF. As a conservative approach to avoid excessive bulk gas heating (as well as to be consistent with the theory employed in the BOLSIG+ solver), the BOLSIG+ energy loss term is the model employed in the bulk gas energy equation in the plasma solver as an energy source term.

Chapter 5

Numerics

5.1 S3D solver

A fully compressible reacting flow solver, S3D, developed at Sandia National Labs, (Chen et al., 2009; Im et al., 2012; Hawkes et al., 2005), is used as the base solver for implementing the plasma transport and chemistry functionality. S3D is a FORTRAN90 solver that achieves parallelism in the MPI framework using (in this work) OpenMPI compiled with the Intel Fortran compiler, with aggressive optimization to activate auto-vectorization. The governing equations described in Section 2.1 are discretized directly using simple finite difference methods. Spatial derivatives are approximated using 6th order centered differences and time derivatives are approximated using a 4th order low-storage explicit Runge-Kutta method. High performance parallel input and output is achieved using the HDF5 library (Folk et al., 1999). All simulations are performed using a 16 core Intel Xeon server with hyper-threading (i.e. 32 software threads). Simulations typically have a wall time on the order of 2-3 days when simulating plasma assisted ignition (see Chapter 7).

5.2 High-order schemes

The use of high-order methods is important not only due to their superiority over low-order schemes with respect to their decay in local truncation error under grid refinement, but also for accurately capturing phenomena with small spatial scales on any fixed finite grid due to the strong low-pass filtering behavior of low-order schemes. This spectral accuracy of finite difference schemes can be analyzed by considering differencing schemes acting on the Fourier modes of a test function, using modified wavenumber analysis (Lele, 1992).

For example, consider some function $g(x)$ with Fourier representation:

$$g(x) = \sum_j \tilde{g}_j exp\left(\frac{2\pi ijx}{L}\right) \tag{5.1}$$

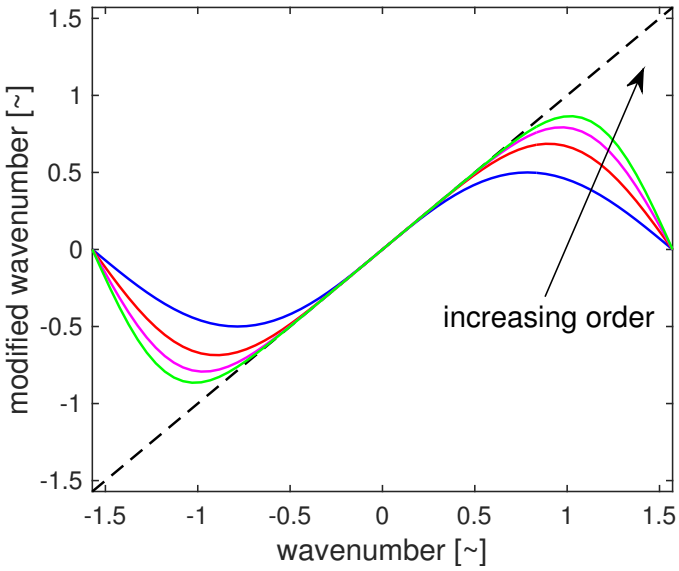

Figure 5.1: Spectral accuracy of centered finite difference schemes of 2nd, 4th, 6th, and 8th order.

over a domain of length L, where j are the wavenumbers of the Fourier expansion and $i = \sqrt{-1}$, analytic differentiation of each mode will result in modified Fourier coefficients, $\tilde{g}_j^{'}$ as:

$$\tilde{g}_j^{'} = \frac{2\pi i j}{L}\tilde{g}_j \tag{5.2}$$

Defining a scaled wavenumber w as:

$$w = \frac{2\pi j}{N_{grid}} \tag{5.3}$$

where N_{grid} is the number of grid points (collocation points) used for the discrete representation of the function g, the relationship between the Fourier coefficients of the differentiated modes and the original modes under analytical differentiation becomes:

$$\tilde{g}_j^{'} = iw\tilde{g}_j \tag{5.4}$$

while the relationship between the same modes under approximate differentiation using some form of finite differencing is then:

$$\tilde{g}_j^{'} = iw^{'}\tilde{g}_j \tag{5.5}$$

The spectral accuracy of finite differencing can then be quantified for each wavenumber by comparing the exact w with the approximate $w^{'}$.

Fig. 5.1 displays the relationship between w (abscissa) and w' (ordinate) for commonly used schemes, including those used in S3D for approximating gradients. The straight line represents the expected attenuation of Fourier coefficients under analytic differentiation (i.e. zero attenuation) while the curves represent the ratio w'/w for the finite approximations. It is clear that all finite approximations attenuate the magnitude of the Fourier mode to some degree, and the well resolved modes are those with the lowest wavenumber. The highest possible wavenumbers on the grid are annihilated by all finite schemes, while higher order schemes attenuate modes less at higher wavenumbers than the lower order schemes.

Reinterpreting the differentiation procedure as a cascade of two operations, exact differentiation followed by a filtering procedure, Fig. 5.2 shows the consequence of low order schemes more clearly. While increasing order preserves spectral content, there is a diminish return. Furthermore, increasing order is achieved for these centered schemes by increasing the size of the differencing stencil. This stencil can only be increased to the limit of the spatial discretization employed by the parallel topology (i.e. the width of an MPI domain), before increasing order requires sacrifice of parallelism or increased complexity of parallelism.

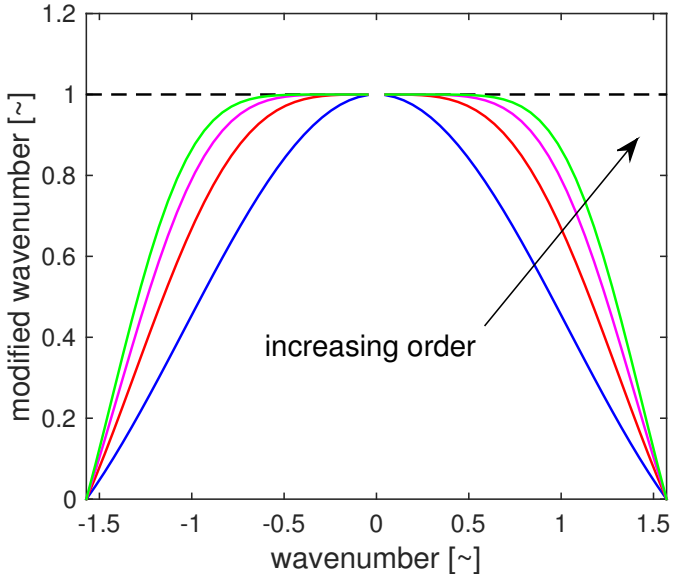

Figure 5.2: Filter characteristics of centered finite difference schemes

5.3 Iterative linear solvers

A fundamental numerical problem of interest for the plasma solver is Gauss' Law of electromagnetism, which is a Poisson equation for electric potential forced by the charge distribution. The elliptic character of this equation introduces global coupling, and its numerical form can be written as a simple linear system:

$$Au = b \tag{5.6}$$

where A is the numerical Poisson operator (employing second order finite differences in this case), u is the solution vector (i.e. for electric potential), and b is the right-hand-side (i.e. the charge density scaled by the vacuum permittivity).

Since direct methods for solving this linear system can be expensive and difficult to implement in parallel applications, the use of an iterative method is attractive. The numerical solution methodology is to solve for a transient variable $\tilde{u}$ as a function of a pseudo-time t and use this transient variable as an approximation for u following:

$$\frac{d\tilde{u}}{dt} = A\tilde{u} - b \tag{5.7}$$

such that the steady state solution to the parabolic transient problem converges to the solution of the elliptic time-independent problem.

$$\frac{d\tilde{u}}{dt} \to 0, \tilde{u} \to u \tag{5.8}$$

Approximating the time derivative using a simple explicit finite difference:

$$\tilde{u}^{n+1} = \tilde{u}^n + \xi \left(A\tilde{u}^n - b\right) \tag{5.9}$$

where ξ is the numerical time step in the pseudo-time coordinate. The error after some arbitrary number of time steps n is:

$$e^n = \tilde{u}^n - u \tag{5.10}$$

This iterative solution algorithm (known as the Jacobi method) can be used to iterate the solution to convergence, however such an approach is typically hindered by extremely slow convergence of low wavenumber components of the error.

Applying the numerical Poisson operator to the error itself:

$$Ae^n = A\tilde{u}^n - Au = A\tilde{u}^n - b \equiv R^n \tag{5.11}$$

where R^n is defined as the residual at iteration 'n', defines a new linear system that can be solved for the error of the iterative scheme discussed previously:

$$Ae^n = R^n \tag{5.12}$$

For an unconverged $\tilde{u}^n$ after a certain number of point iterations, the true solution is known if e^n can be found. One important observation is that, after a few iterations of point relaxation using a method such as Jacobi, the high wavenumber components of the error will be sufficiently damped that the spectral content of the residual can be represented on a coarser grid. By restricting the residual onto a coarser grid and solving Eq. 5.12 by performing point relaxation on this grid, the convergence of the error can be accelerated. When

the error is converged it can then be interpolated back to the fine grid and the true solution determined from Eq. 5.10. A few more point relaxation iterations are typically performed on the fine grid to smooth out any high wavenumber errors introduced by the interpolation procedure. This procedure can be considered as a single level multigrid algorithm.

The true power of the multigrid approach comes from identifying that Eq. 5.12 is simply a numerical Poisson equation in its own right which can be solved using the same philosophy as was applied to the numerical form of Eq. 5.6 at the start, i.e. making the multigrid approach recursive at every level. In this approach a hierarchy of iterative linear systems is solved for a cascade of errors, allowing the error on the finest grid to be converged rapidly. It can be formally shown that the multigrid algorithm requires $\mathcal{O}(N)$ work to achieve convergence and is versatile in its implementation in parallel topologies as most of the work is still performed pointwise.

Appendix B contains the source files for the multigrid solver developed for solving the Poisson equation conforming to the parallel topology of the S3D solver. The example case in the source driver is for a single Fourier spatial mode (sine wave) with wavelength spanning the domain, as waves of this type represent the most challenging convergence test for iterative methods using point relaxation. Besides the Jacobi algorithm, the Gauss-Seidel, and Gauss-Seidel with red-black ordering (GSRB) algorithms are implemented. The expected multigrid convergence (i.e. $\mathcal{O}(N)$ work to convergence) is achieved (convergence data not shown). However, since sparse linear algebra is a common motif of high performance parallel computing, many high-performance multigrid libraries already exist that are highly optimized. The HYPRE library (Falgout and Yang, 2002) is an example of a sparse linear-algebra framework that leverages the multigrid algorithm along with a variety of error estimation metrics and grid coarsening strategies to achieve optimal convergence. The HYPRE library was finally chosen as the appropriate implementation for the plasma solver developed in this work due to its superior performance, but also due to the fact that it easily generalizes to multiple dimensions, a planned direction of future work.

5.4 CHEMKIN

Chemical rate constant parameterizations, thermodynamic data for the various species (i.e. specific heat tabulation with respect to temperature), and transport data (i.e. Lennard-Jones and Stockmayer parameters for molecular potentials) are inputted and processed using the CHEMKIN framework (Kee et al., 1989), which supports the calculation of chemical rates as a function of multiple temperatures. In order to accelerate the expensive calculation of the chemical rates, the rate constants are precomputed using the CHEMKIN routines across a range of expected temperatures and linearly interpolated at runtime, delivering an approximately factor of two speed-up during execution. For temperatures outside the precomputed temperature range the rate constants are calculated directly using CHEMKIN in-situ.

For electron impact reactions, the rate constants calculated from BOLSIG+ are interpolated across a range of electron temperatures T_e using fits available in the CHEMKIN package, e.g.:

$$k = AT_e^{\beta} exp\left(\frac{E}{T_e} + \sum_{n=1}^{9} b_n \left(\ln T_e\right)^{n-1}\right) \tag{5.13}$$

The rate of progress of the reaction is calculated assuming a fixed mixture using the fresh gas composition, where β, E, and A are fitting parameters in addition to the nine coefficients b_n.

5.5 PREMIX

PREMIX (Kee et al., 1985), a component of the CHEMKIN suite of reacting flow solvers, is a steady, one-dimensional, laminar flame solver that computes the temperature and species profiles for freely propagating and burner stabilized flames using finite rate chemical kinetics and multi-component molecular diffusion under constant pressure conditions. For the case of freely propagating flames at steady state, the mass continuity equation:

$$\dot{M} = \rho u = const \tag{5.14}$$

results in a constant mass flux, which is an eigenvalue of the system that must be determined as part of the solution, and this eigenvalue is constrained by the solution methodology such that the flame is stabilized at an arbitrary position within the computational domain. The boundary conditions at the inlet are specified mixture and temperature and (implicitly) zero-gradient at the outlet. The steady equilibrium of the energy and species transport equations are solved using Newton iterations until convergence is achieved to within arbitrary numerical tolerances. The result for a given input inlet condition, chemical kinetics specification, thermodynamic data, and transport data is the mass flux required to stabilize the flame under such conditions. With knowledge of the density field from the species and energy profiles this mass flux can be translated into fluid velocity, which is equivalent to the laminar burning velocity of the propagating flame. With the inclusion of charged species in the chemical kinetic mechanism and modification of the diffusive transport calculation to account for body forces arising from the action of Coulomb forces, the calculation of the electric potential in the domain can be included as part of the Newton solve in order to determine the steady electric potential arising from the charge generated by the flame. Furthermore, boundary conditions for the electric potential can be specified in order to investigate the influence of applied fields on the flame stabilization.

Chapter 6

Electronic structure of flames

6.1 Laminar flames

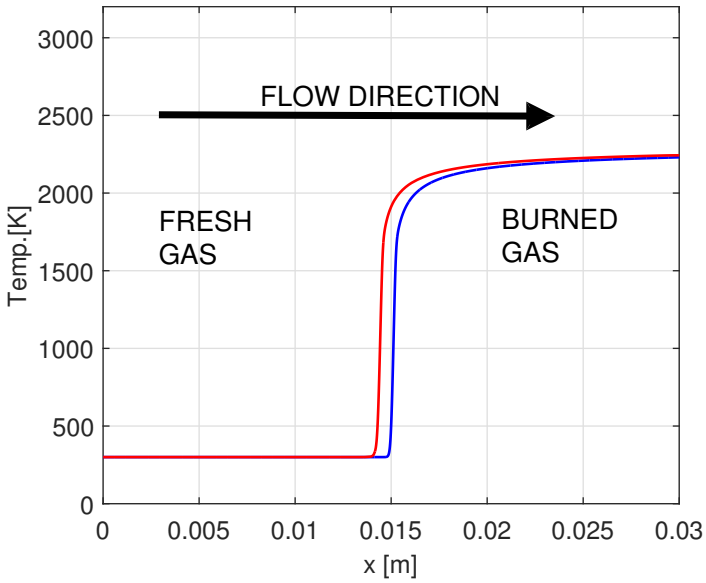

Figure 6.1: Comparison of PREMIX (red) and S3D (blue) laminar flame calculations: temperature field

In order to understand the fundamental processes in a reacting combustion plasma, the planar one-dimensional laminar premixed flame framework is investigated using the transient plasma combustion solver (i.e. modified S3D). This set-up is particularly advantageous as the 1D laminar flame will admit a steady solution. Analyses of laminar flames have been used to investigate the production of charged species in flames in the context of the measurement of saturation currents (Speelman et al., 2015a,b) which is of importance for

practical combustion devices. Figure 6.1 shows the solution for the temperature field for a stoichiometric laminar premixed methane-air flame at atmospheric pressure and ambient fresh gas temperature (300K) in a domain with grounded ends (left and right boundaries at 0V) which was investigated using both the transient solver (S3D) which employs a homogeneous mesh as well as a steady solver (PREMIX (Kee et al., 1985)) employing adaptive mesh refinement, with both codes accounting for the transport of charged species by electric fields. The chemistry used for these laminar flame simulations is a skeletal methane-air combustion mechanism with the chemi-ionization pathway (see Chapter 4) added to represent the generation of electrons and ions at low electric fields. For such flames, the production of charged species depends on the location of the peak in the CH species profile. For both solvers the flame is set-up to be anchored approximately in the center of a 3 cm domain, in the case of the transient solver by tuning the fresh gas boundary velocity to equal the laminar burning velocity (i.e. flame speed) of the flame. The stabilization points used in each code are separated slightly for clarity of presentation. The flame acts a thin zone which converts the fresh gas methane-air mixture into products with a temperature rise (and associated density decrease and fluid velocity increase) due to chemical heat release. In its steady state, the entire domain is at essentially constant pressure, except for the small change in pressure associated with the momentum change across the flame.

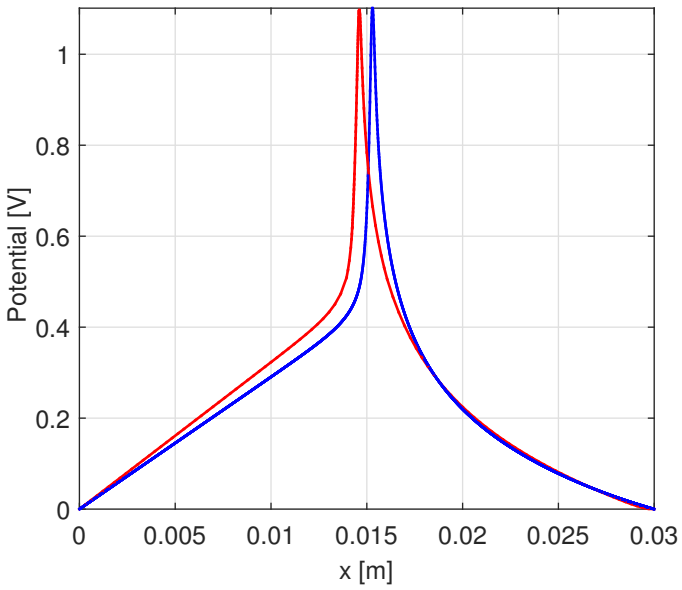

Figure 6.2: Comparison of PREMIX (red) and S3D (blue) laminar flame calculations: electric potential

The flame acts as a source of charge and establishes an electrical structure within the domain due to the weak self-fields induced by local charge separation. The potential field admitted by the presence of the flame with both ends grounded is shown in Fig. 6.2. In

the fresh gas the potential is essentially linear, indicating zero charge density in this region. Moving closer to the flame the curvature of the potential shows a positive increase, indicating the presence of a locally negative charge density. The potential then shows an extremely abrupt change to negative curvature before transitioning back to a more gradual positive curvature in the hot burned gases. The consequence of this potential field structure is that the fresh and burned gas electric fields are essentially constant while an abrupt change takes place in the flame zone only (Fig. 6.3).

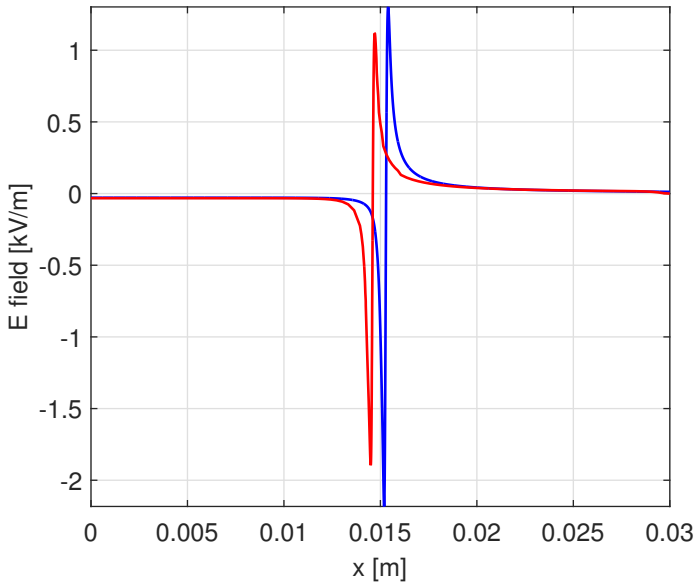

Figure 6.3: Comparison of PREMIX (red) and S3D (blue) laminar flame calculations: electric field. The PREMIX solution can support a slightly higher curvature due to the implementation of adaptive mesh refinement delivering additional mesh resolution in the flame.

The rapid local change in the electric field suggests that charged species transport is important only in the flame region itself, and that the electric potential in the vicinity of the flame depends on how charge created there is transported. Figure 6.4 shows the spatial variation of the electron drift flux (associated with the electron response to a collision-averaged Coulomb force) and diffusion flux (associated with thermal motion) in the steady flame. The sign of the electron diffusion mass flux is negative on the upstream side and positive on the downstream side of the flame reflecting the random-walk character of electron mass diffusion away from the flame where the electron density is expected to be at a maximum. The electron drift mass flux is precisely the opposite, indicating that electrons that have escaped the flame zone are transported back towards the flame. By comparing these mass fluxes on a single axis (Fig. 6.5) we see that these fluxes are identically in balance, and the electron density is in a dynamic equilibrium in the flame zone. In contrast to neutral species whose density is essentially determined by a balance of reaction and diffusion, charged species den-

sities will depend on an additional anisotropic mass flux determined from the electric field, and for the example of the electron species, the electric drift flux that is established is such to resist the action that establishes the electric field (i.e. electron mass diffusion).

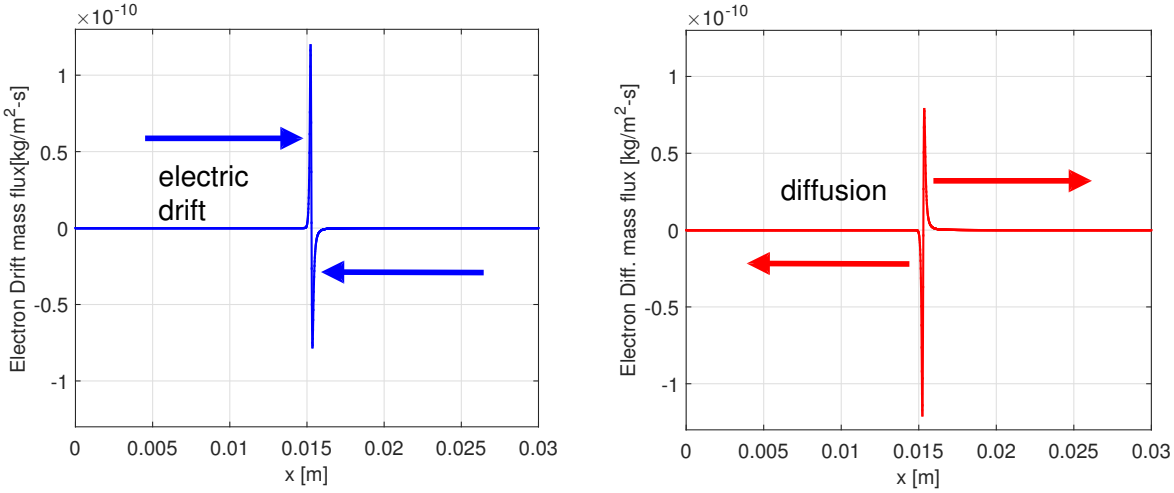

Figure 6.4: Electron drift (a) and diffusion (b) mass fluxes in a laminar flame

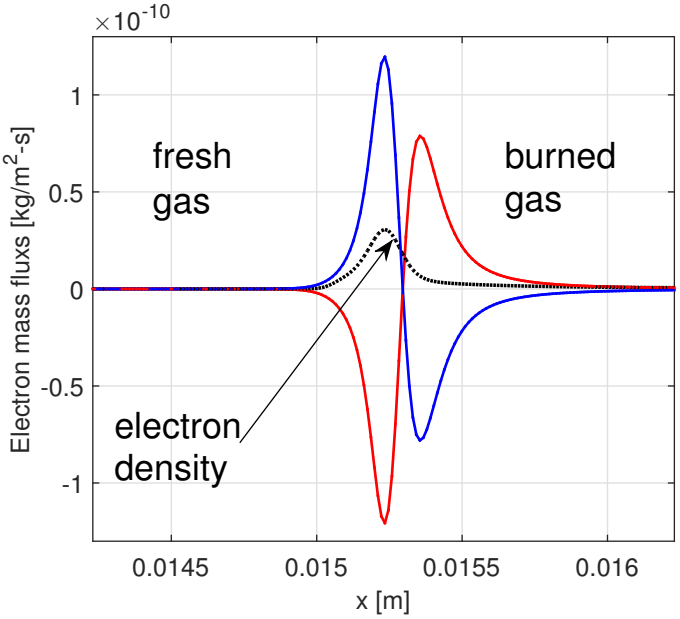

Figure 6.5: Electron mass fluxes. The electron density is plotted in arbitrary units (dashed line).

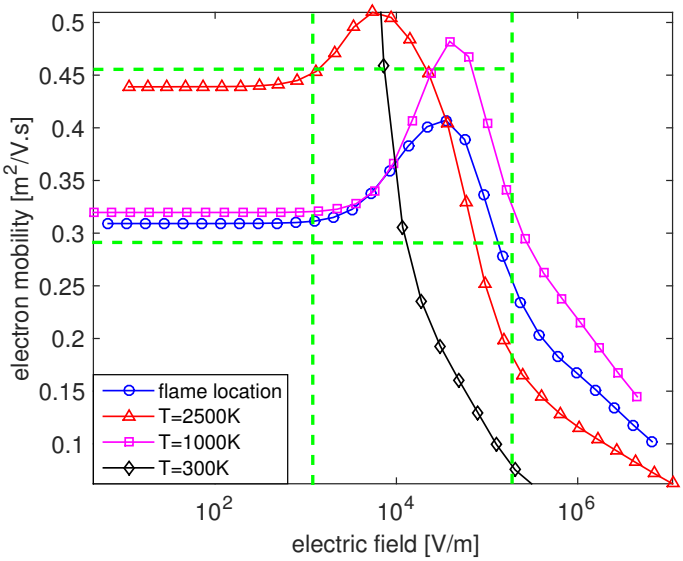

Figure 6.6: Electron mobility

Using the mixtures and temperature solutions for the laminar flame discussed previously, the BOLSIG+ solver (see Section 4.3) was used to calculate the electron EEDF and the relevant electron transport properties for a range of hypothetical electric field strengths as a post-processing procedure (i.e. electric fields uncoupled from the flame dynamics). Figure 6.6 shows the variation of electron mobility with electric field at various locations in the flame using the local mixture and temperature. At all locations the mobility is essentially insensitive to the electric field strength at low values of electric field. At high values of electric field the mobility falls, attributable to the increased energy of electrons increasing the effective electron-neutral collision frequency. In the electric field range below approximately 10 ^{5}V/m (corresponding to applied voltages on the order of a few kV for this domain size) the mobility in the flame zone is approximately 0.4 $\mathrm{m^2V^{-1}s^{-1}}$, which agrees with values typically found in the literature (and in fact is the value employed in the PREMIX and S3D simulations used to generate the flame data, making the choice self-consistent). Figure 6.7 shows the normalized mobility (i.e. the mobility normalized by the local total neutral species number density), indicating that at large values of electric field the normalized mobility is independent of location in the flame. This phenomenon suggests that the collision cross sections for the individual species comprising the various mixtures at each flame location become unimportant at high electron energies and the electrons no longer differentiate between their collision partners.

Using the constant mobility discussed previously, the PREMIX solver was used to simulate flames under a variety of applied voltages. Figure 6.8 shows flames subject to applied voltages ranging from 100 V to 6000 V, with both positive burned gas applied voltage (blue curves) and positive fresh gas potential (red curves), to instigate differential electron

transport through the boundary conditions. The conditions are identical to those employed previously apart from the use of a smaller domain (1 cm). The approximate flame location for all simulations is marked with a dashed line. For both polarities, variations in the electric field are restricted to the fresh gas and the electric field in the burned gas is essentially zero. The burned gas thus represents an electrically 'dead-zone', where although the quantity of charged species is quite high, the mixture is locally neutral. This quasi-neutrality in the burned gas shows a highly anisotropic response to the applied voltages, with the burned gases containing sufficient charge to adjust to the charge fluxes sourced from the flame so as to remain quasi-neutral regardless of the direction of the electric field.

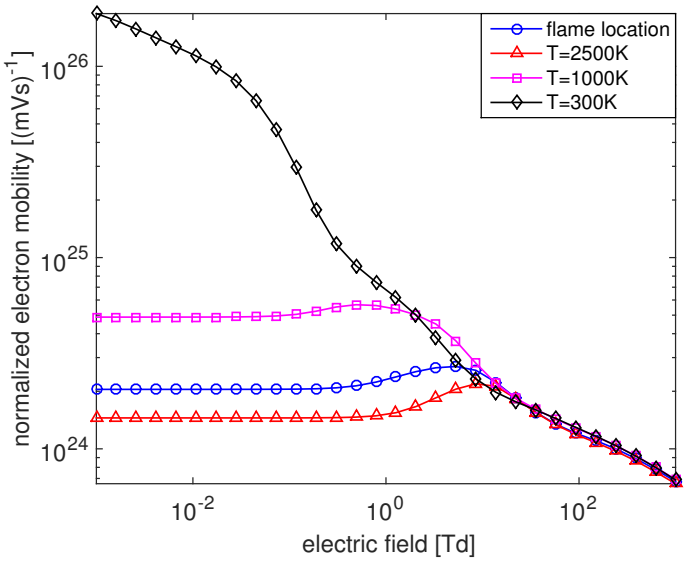

Figure 6.7: Normalized electron mobility (μ_eN)

As a consequence of the presence of the electric 'dead-zone', the electric field is only non-zero in the fresh gases. As such, the opportunity for non-thermal electron behavior is essentially restricted to the fresh gases. Although the PREMIX solver assumes that the electrons are thermal and only contains charged species chemistry at the level of chemi-ionization, an approximation for the fresh gas electron temperature in the low electric field limit can be post-processed using the BOLSIG+ solver in a similar way as to how the electron mobility was calculated for Figs. 6.6 & 6.7. Figure 6.9 shows the fresh gas electron temperature for the applied voltages simulated, with temperatures as high as 25,000 K estimated for the highest applied voltages used. The results are essentially identical for both polarities in the fresh gas, while the burned gas electron temperature associated with the negative polarity (red curves) appears to be higher than the positive case. It is suspected that the negative polarity result admits an artificially high electric field in the burned gas as a result of the boundary conditions employed by the PREMIX solver, which are designed to conserve mass but not charge.

The steady laminar flame simulations allows us to make some broad conclusions as to the response of reacting flows to applied voltages, in particular the anisotropy of the potential and electric field due to the 'dead-zone' phenomenon. For strong electric fields with non-thermal plasma transport fully coupled to the solution the dead-zone behavior is also observed. Figure 6.10 shows the evolution of the electric field in a laminar flame subject to a strong applied potential (9 kV) solved using the transient S3D plasma solver. The electric field is initially almost constant in the fresh and burned gases (with a sharp variation only in the flame zone) but over the course of approximately 20 ns, a quasi-steady field is established with a strong increase in the fresh gas magnitude and large decrease in the burned gas magnitude such that a dead-zone is established.

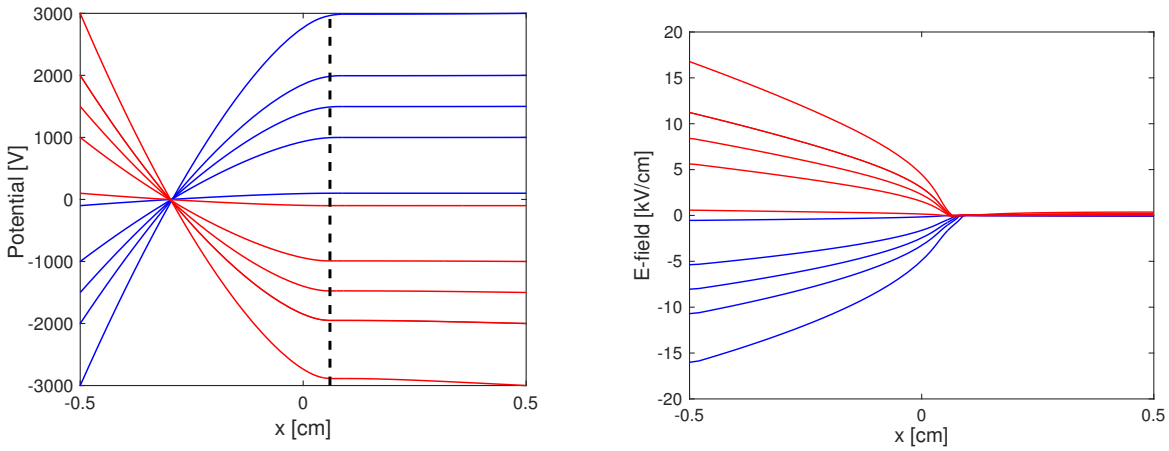

(a) (b)

Figure 6.8: PREMIX steady laminar flames: voltages (a) and electric fields (b)

6.2 Lookup tables

Invoking the BOLSIG+ solver directly within the plasma flow solver can be a prohibitively expensive exercise, as the EEDF must be calculated at every grid point for every time step. When the time step is necessarily decreased in order to resolve the small times scales of plasma chemistry or the fluid velocities of electrons under strong electric fields, the direct use of the BOLSIG+ solver becomes completely intractable in the current numerical framework. As an alternative to solving for the EEDF directly to determine electron properties in-situ, a tabulation approach is employed where the required parameters are precomputed and values are looked up by the plasma solver. BOLSIG+ takes gas temperature, reduced electric field and mixture as inputs to calculate electron properties, which inevitably results in precomputed tables of high dimension. In order to limit the dimensionality of the tables,

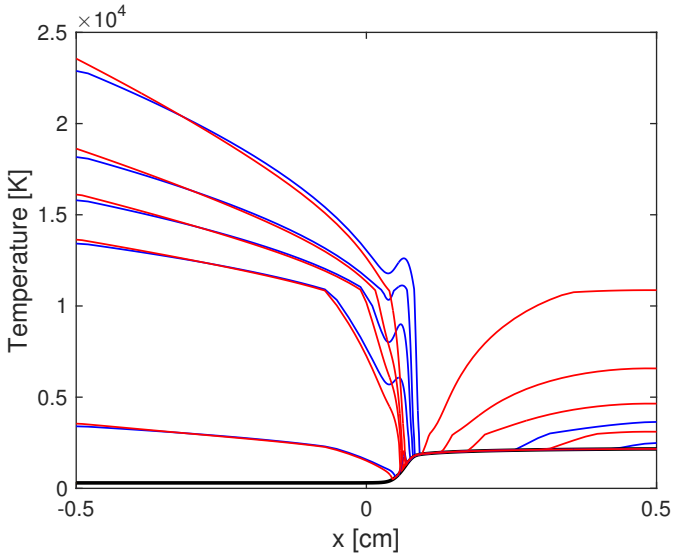

Figure 6.9: PREMIX steady laminar flames: electron temperatures. The black curve is the bulk gas temperature.

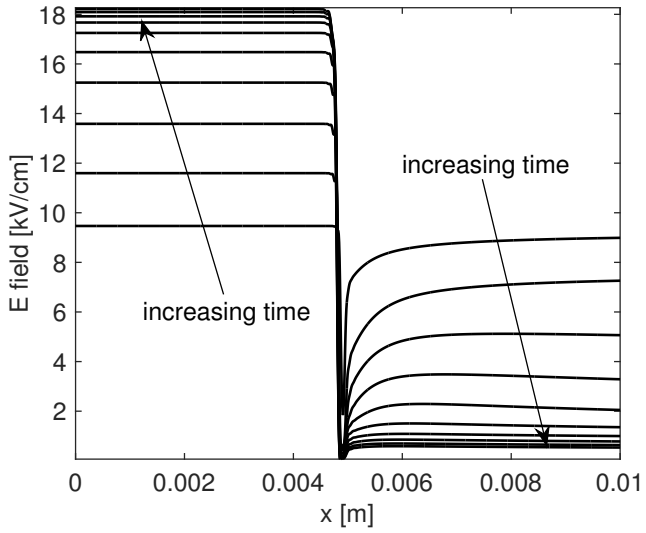

Figure 6.10: Establishment of electric field in a laminar flame under strong applied voltage. On application of a DC voltage, a quasi-equilibrium electric field is established in approximately 20 ns

the mixture is restricted to four major neutral species, which typically make up approximately 95% of the neutral population. As a result of this simplification the dimensionality of a precomputed data table would ostensibly be six, with dimensions for gas phase temperature, reduced electric field, N_2, O_2, CO_2, and H_2O number densities. However by posing the

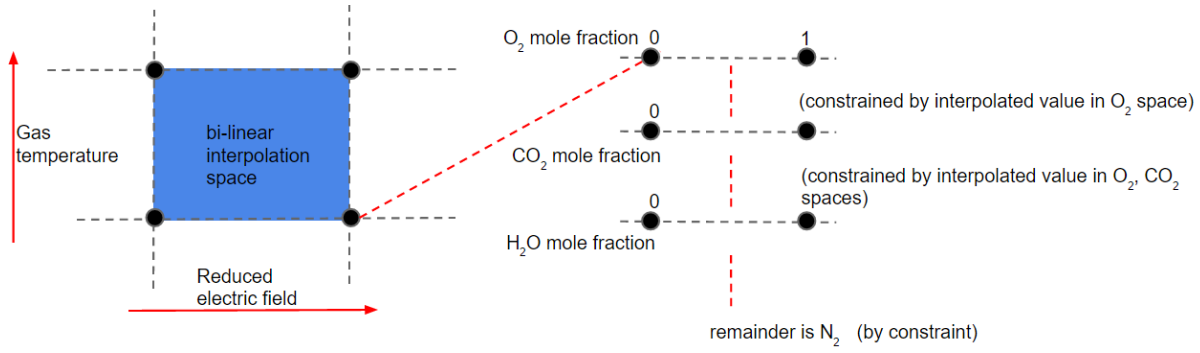

Figure 6.11: Interpolation scheme for BOLSIG+ tables

mixture data in terms of fractions, the dependence of each species (mole) fraction on the remaining species in the set allows for the reduction of the table dimension by one. Figure 6.11 shows a schematic of the interpolation scheme employed. A two-dimensional interpolation space spanning gas phase temperature and reduced electric field is constructed where each discrete node represents the mixture space. Within each of the four bounding nodes the input value of the O_2 mole fraction is used to find the bounding table entries in O_2 space. Within each of these bounding values for O_2, the input value of CO_2 is used to find the bounding table entries in CO_2 space where this space ranges from 0 to 1-X_{O_2} (i.e. the space constrained by the O_2 mole fraction through the definition of mole fraction). This procedure is continued for the constrained H_2O space (i.e. constrained between 0 and 1-X_{O_2}-X_{CO_2}). Interpolation for N_2 is then unnecessary as N_2 is already completely constrained by the other components of the mixture. The value of the target parameter is assigned at the level of the H_2O space and is interpolated upwards to the level of the two-dimensional 'temperature-reduced electric field' space, at which point a bi-linear interpolation is performed to determine the approximate value of the target parameter.

The tables are built by invoking the BOLSIG+ solver to populate a discretized space employing either linear or logarithmic grid spacing. The typical discretization employed is 20 points per variable, resulting in 20^5 table entries, highlighting the importance of reducing the overall dimensionality. A table file typically takes up 100MB of disk memory when saved in ASCII (for debugging purposes) or 50MB when stored in binary. Using serial processing, such tables take approximately 10 hours to build, but the procedure can be sped up quite easily using multi-threaded parallelism as the problem presents an embarrassingly parallel workload.

When comparing the lookup procedure using tables to direct invocation of the BOLSIG+ solver in-situ, the speedup is typically three orders of magnitude, which makes a significant difference to the solver performance as the procedure is typically called 30 times per processor per time step at the level of parallelism employed in this work.

6.3 Electron temperature approximation

Electron properties can be precomputed for representative mixtures, but by pre-computing the electron parameters the electron EEDF is also available, with the expected value of the EEDF being an equilibrium approximation of the electron energy. The electron energy (and thus temperature by triviality) can also be solved for by deriving a conservation equation from the electron distribution function directly by taking appropriate moments, and accounting for all appropriate energy exchange mechanisms. For the case of strong electric fields, the rate at which the electron temperature increases due to acceleration by the electric field (i.e. Joule heating) imposes a serious time scale restriction on the explicit numerical integration framework employed by the plasma solver. This can be shown by performing a rudimentary scale analysis on the electron energy equation. Ignoring transport fluxes and assuming that the dominant source term is Joule heating, the electron energy equation becomes:

$$\frac{d}{dt}\left(\frac{3}{2}n_e k_B T_e\right) = e n_e \mu E^2 \tag{6.1}$$

Assuming that the electron density is steady on the scale of the electron energy evolution:

$$\frac{3}{2}n_e k_B \frac{dT_e}{dt} = e n_e \mu E^2 \tag{6.2}$$

Simplifying:

$$\frac{3}{2}k_B \frac{dT_e}{dt} = e \mu E^2 \tag{6.3}$$

Approximating the electron temperature time derivative as a simple finite difference:

$$\frac{dT_e}{dt} = \frac{2e\mu E^2}{3k_B} \approx \frac{\Delta T}{\Delta t} \tag{6.4}$$

A time scale for electron heating is isolated:

$$\Delta t \approx \frac{3k_B \Delta T}{2e\mu E^2} \tag{6.5}$$

Substituting values associated with strong electric fields (taken from the results of simulations), e.g. T_e=35,000K and E=2,000,000V/m, results in a characteristic rise time on the order of 10^{-12}s, and even smaller for higher values of E which are often admitted. As such, changes in the electron temperature field occur incredibly rapidly and to adequately resolve transients of the electron temperature would require numerical time steps much smaller than the scale derived above. This is inevitably intractable in the current numerical framework. This realization leads to the approximation of local equilibrium of the electron temperature field, and the equilibrium value of electron energy (as calculated using the BOLSIG+ solver) is taken to be a reasonable representation of the instantaneous electron temperature.

Changes in the steady laminar flame dynamics (i.e. noticeable changes in flame speed, flame temperature) were not observed when electric fields were applied, besides the small temporal perturbations during the initial application. The numerical framework employed in this study is far more suited for the study of highly transient phenomena, and due to the time resolution requirements of chemistry and charged species dynamics, time scales on the order of the variation of the laminar flame speed are so large as to be almost intractable to resolve. As such, more suitable frameworks for the study of the applied electric fields are considered to study chemistry in the presence of transport and spatial variations in electric potential, which leads to the consideration of the planar ignition framework discussed in the following chapter.

Chapter 7

Plasma assisted ignition

7.1 Introduction

As mentioned previously, flames act as weakly ionized plasmas, generating weak self-induced electric fields due to local charge separation over small distances of length comparable to the reaction zone. As such, externally applied electric fields have the potential to augment flame behavior non-intrusively. Investigations of applied electric fields have shown the ability to enhance burning velocities (Jaggers and Von Engel, 1971), stabilize flames near flammability limits (Bak et al., 2012), and support ignition (Wolk et al., 2013). If the strength of the electric field is high enough to produce a sufficient level of non-thermal electrons, it is understood that enhancement occurs due to fragmentation of fresh gas molecules resulting in an increased population of reactive intermediates such as O and H (Ju and Sun, 2015).

In the context of ignition, simulations of multiple nanosecond pulsed plasma discharges in n-heptane have been shown to decrease ignition delay time significantly (Nagaraja et al., 2015) through the generation of non-thermal electron plasma in a breakdown process. Furthermore, it has been demonstrated experimentally that microwave frequency electric field excitation reduces the flame development time of inductive spark ignition of methane-air mixtures in a constant volume chamber (Wolk et al., 2013). The experiments by Wolk et al. suggested that enhancement arises as a result of flame wrinkling due to the perturbative effect of the applied field, indicating that both chemistry and hydrodynamics play important roles. As a practical concern to ignition strategies relying on breakdown arc discharges, increasing the energy of the discharge itself (e.g. increasing the spark energy) can have undesirable effects in terms of device wear due to electrode ablation arising from the hot flow of current in the gas medium, which presents significant challenges for igniting lean high-pressure mixtures typical of projected future advanced engine technologies. As such, it is desirable to investigate means of ignition and ignition-support that occur in the sub-breakdown regime (i.e. avoiding excessive arcing) that deliver necessary performance, while avoiding excessive device wear. Furthermore, with increasing interest in using natural gas as a clean fuel alternative, the plasma-assisted ignition of methane is an important process due to the difficulty

of initiating the first H abstraction from CH_4. Analysis of non-thermal electron transport properties and energy coupling to bulk mixtures in the sub-breakdown regime in premixed methane-air flames suggests a breakdown threshold of approximately 150 Td (Bisetti and Morsli, 2014). As such it is of interest to investigate sub-breakdown electric field assisted combustion of an established ignition kernel at device relevant pressure, in order to shed light on the multiple electrodynamic and chemical processes involved in possibly increasing the overall mass of fuel burned as a result of the application of strong electric fields.

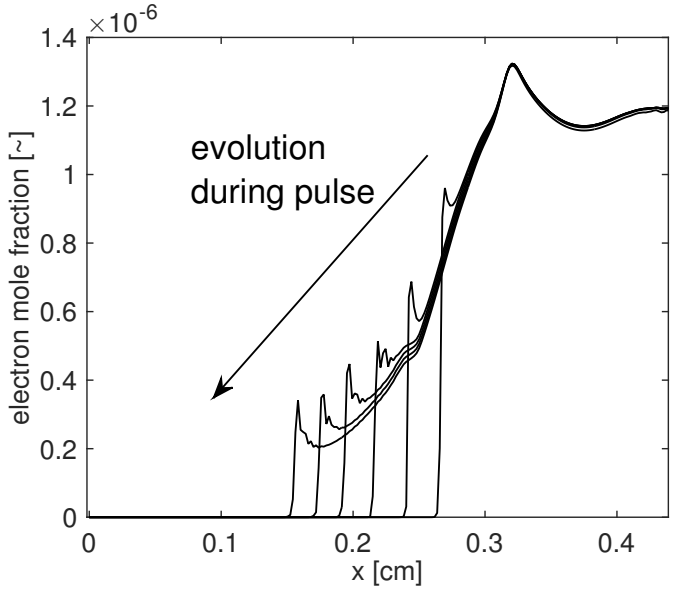

Figure 7.1: Electron mole fraction

The ignition regime also presents a more suitable framework with which to study the response of combustion to applied electric field due to the much higher electron densities admitted by the hot ignited gases through chemi-ionization. The initial pool of electrons is crucial for initiating the ionization processes that are important for activating the plasma chemistry, and the regime maps developed by DeFilippo (DeFilippo, 2013) for homogeneous reactor simulations with specified electric field and initial electron mole fractions showed that mole fractions on the order of 10^{-7} and above are required to see any reasonable effect of plasma kinetics on the ignition delay of methane-air mixtures. Figure 7.1 shows the evolution of the electron mole fraction during ignition subjected to applied electric fields, showing that the burned gas electron density is on the order of 10^{-6}, indicating that under the conditions of planar ignition significant plasma kinetic effects should be expected.

7.2 Configuration and modeling

The physical domain chosen for the simulations is a 1 cm region filled with premixed methane and air (79% N_2 and 21% O_2 by volume) with equivalence ratio 0.5 at 1 atm. This lean condition is chosen as it coincides with the maximum observed ignition enhancement observed in experiments (Wolk et al., 2013). The boundaries are open fluid outlets (i.e. implemented using non-reflective characteristic boundary conditions at each end) with imposed potentials (i.e. Dirichlet conditions for the Poisson equation for Gauss' law), conceptually representing wire mesh electrodes unobstructive to fluid. This configuration is chosen such that the ignition event occurs at approximately constant pressure, allowing ignition to smoothly transition to quasi-flame behavior at 1 atm. The nanosecond pulses are applied with positive 4.5 kV and negative 4.5 kV on the left and right electrodes respectively, for a total of 9 kV across the domain. Pulses are applied for up to a maximum of 35 ns, as pulses of longer duration resulted in charge interacting excessively with the boundaries. These pulse parameters are chosen to represent the typical values employed in constant-volume methane-air plasma ignition experiments using advanced ignition devices relying on nanosecond DC pulses (Pineda et al., 2015).

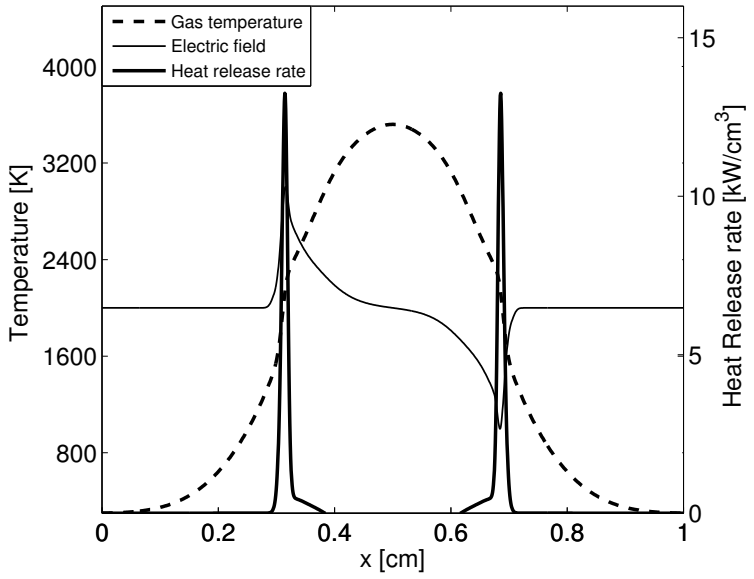

Figure 7.2: Instantaneous gas phase temperature, heat release rate, and electric field (arbitrary unit) just prior to the application of the external potential. A hot burned gas zone supports the rapid outward propagation of heat release rate fronts where charged species are produced. The peak electric field strength is 0.5 Vcm^{-1}. The zero gradient of the electric field in the fresh gas indicates the absence of charge density.

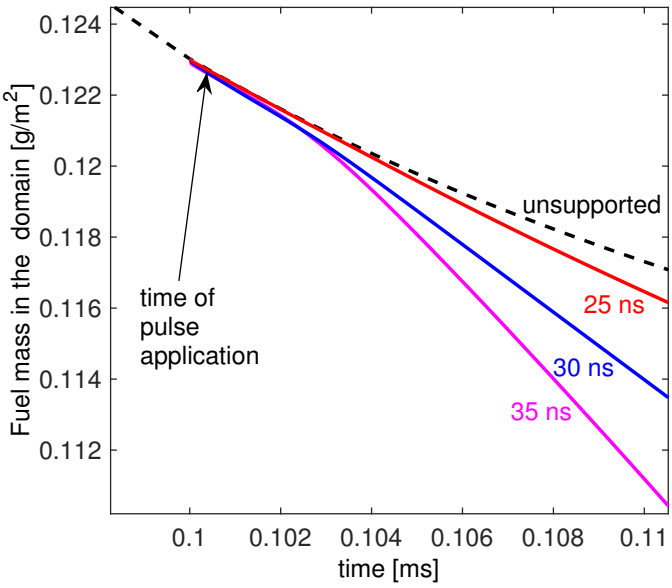

Figure 7.3: Ignition enhancement as a function of voltage pulse width, quantified by the remaining fuel mass in the domain as a function of time.

Numerics

As discussed in Section 5.1, a compressible reacting flow solver employing high-order central differencing and an explicit Runge-Kutta time integration scheme is used to advance the conservation equations governing the planar ignition problem. The outlet boundaries are implemented in the governing equations using a non-reflecting treatment based on characteristics (Yoo and Im, 2007). The Poisson equation for Gauss's Law for the electric potential is solved using a geometric multi-grid scheme. Electron fluxes are specified in the drift-diffusion limit (i.e. zero electron inertia approximation (Nitschke and Graves, 1994)) using transport coefficients calculated using the BOLSIG+ solver (Hagelaar and Pitchford, 2005). The electron temperature is obtained from BOLSIG+ given the neutral mixture and local reduced electric field. Ion-mobilities are set equal to 1 $\mathrm{cm^2V^{-1}s^{-1}}$ (Fialkov, 1997; Belhi et al., 2013). For computational efficiency, BOLSIG+ electron data are calculated a-priori and retrieved with efficient queries from databases at runtime. Mixture dependency is included by constructing a multi-dimensional interpolation space consisting of the major neutral species. As mentioned previously, the transport data for electronically excited species is assumed to be the same as the ground state equivalents. Due to the explicit time integration scheme, the time scales of the plasma chemistry must be resolved for numerical stability. As such, the time step employed during the high voltage pulse is $\Delta t = \mathcal{O}(10^{-13}$ s). Post pulse, the time step relaxes back to the time scales associated with the gas phase chemistry, typically $\Delta t = \mathcal{O}(10^{-9}$ s). This relaxation strategy has previously been employed successfully in simulations of nanosecond electrical discharges (Poggie et al., 2012; Nagaraja et al., 2013). A

uniform mesh of 1280 grid points is used ($\Delta x \approx 7.8$ μm) with the computational domain decomposed spatially in parallel using the MPI (message passing interface) framework.

7.3 Results and discussion

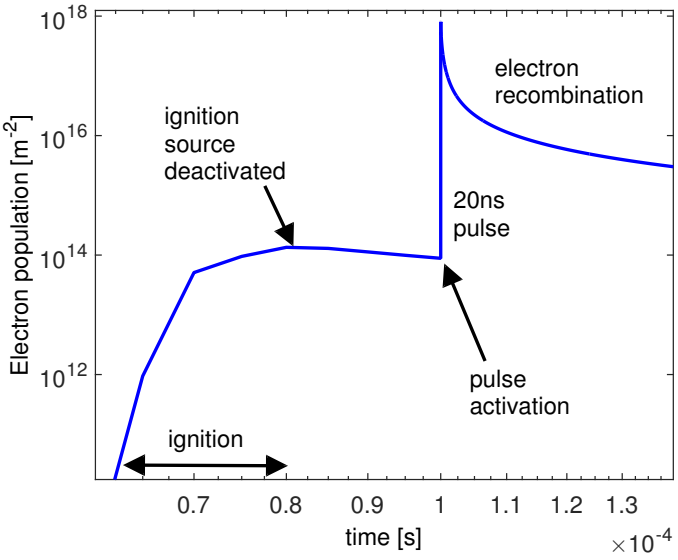

Figure 7.4: Electron population

Overview of ignition enhancement

At the start of each simulation, ignition is initiated using a Gaussian energy source profile with 0.17 cm full width at half maximum (FWHM), with magnitude 16 kWcm^{-3} imposed over the interval $0 \leq t \leq 80$ μs. Approximating the 3D analog of this source profile as a sphere with radius equal to the Gaussian FWHM, gives an estimate of 85 mJ of total energy deposited. This energy deposition is chosen to emulate the typical energies of arc discharge spark plugs. Figure 7.2 shows the gas temperature, heat release rate, and electric field profile 0.1 ms into the simulation. At this time, two reaction fronts, or alternatively ignition waves, originating from the center have propagated away from each other. Throughout the entire simulation period, the reaction fronts undergo highly transient behavior and never reach steady deflagration fronts. As such, it is difficult to assess the effects of the electric pulse in terms of the flame speed enhancement; rather, the effects are quantified in terms of the rate of the fuel consumption within the domain.

The 9kV DC voltage is applied as a step function after 0.1 ms has elapsed, with the voltage sustained for as little as 25 ns or as long as 35 ns. A pool of charged species

exists in the reaction zones due to chemi-ionization prior to the application of the electrical pulse, which subsequently generate further electrons through ionization processes. Figure 7.4 shows the evolution of the total domain integrated electron population during the energy deposition, during the pulse, and post pulse. During the pulse itself the electron population increases by approximation four orders of magnitude due to the activation of secondary ionization processes creating a chain reaction (avalanche) effect. The overall effect of the pulse duration is measured in terms of the temporal evolution of the remaining fuel mass as shown in Fig. 7.3. It is seen that the remaining fuel mass is essentially unchanged during the pulse but begins to deviate from the unsupported solution after approximately 20 μs. No enhancement is observed for pulse lengths shorter than 20 ns, indicating that a threshold of plasma chemistry activation is achieved for longer pulses with a sustained high electron temperature.

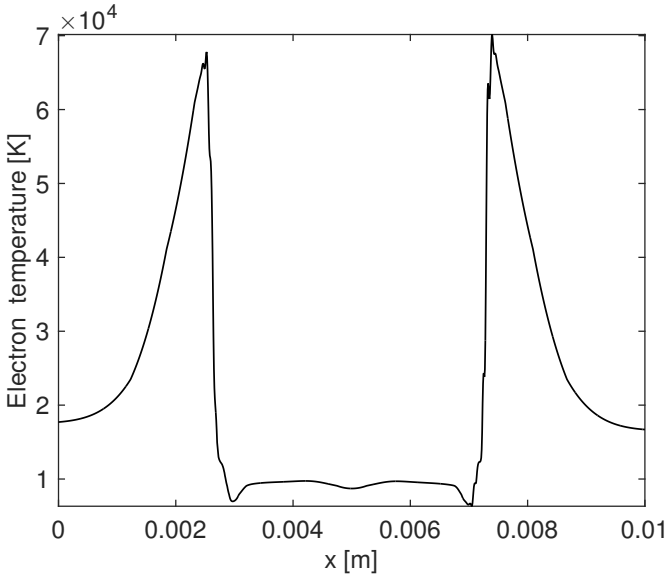

Figure 7.5: Typical electron temperature profile during a nanosecond pulse

Electrodynamics of charge fronts

As a 9 kV voltage is applied across the domain, an electric field pointing towards the right of the domain is established. Under the influence of the electric field, charged species are transported from the flame zone into the fresh gases where electrons take part in further ionization processes, with the electrons and anions transported to the left and the cations to the right. At the same time, the burned gas loses most of its net charge, although the density of charged species remains high and is characterized by an electric field close to zero along with zero potential (i.e. an electric dead-zone). The electric field is shown in Fig. 7.6

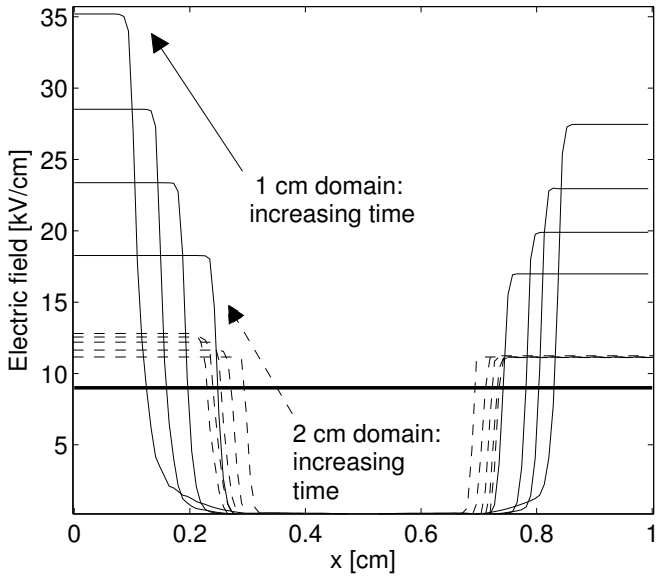

Figure 7.6: Effect of domain size on the electric field strength ahead of the charge fronts in the fresh gases at four time instants during the pulse: 5, 10, 15, and 20 ns. The horizontal line represents the electric field in a domain with zero charge, which is the same for both configurations.

(1 cm case), with zero electric field in the burned gas for all times. The concentration of charge in the outwardly propagating fronts (Fig. 7.7) results in a floating electrode effect, such that changes in the electric field are restricted to regions in the immediate vicinity of the fronts. Across the charge fronts, the potential increases abruptly from zero in the burned gases to a linear distribution in the fresh gas, where there is close to zero charge density and the electric field strength is constant (Fig. 7.6). Figure 7.7 provides a close look at the dynamics of the electrons prior, during, and after the nanoscale voltage pulse. From 3 ns to 7 ns the electron density in the fresh gas on the left side of the domain builds up as electrons, now non-thermal, take part in impact ionization processes as they transit toward the left boundary electrode. At the same time, the positive charge front made up of cations on the right side of the domain builds up due to ionization of fresh gas molecules by non-thermal electrons, initially present at low concentration in the fresh gas due to diffusion from the flame zone prior to the pulse, as they drift to the left. These electrons will tend to remain near the positive right propagating charge front due to the large change in electric field that occurs in its vicinity, hindering their leftward drift motion. Towards the end of the pulse from 23 ns to 31 ns, the charge fronts continue to propagate outwards, with the left moving negative charge front, comprised primarily of electrons, advancing further than its cation analog. Post pulse, the charge fronts collapses due to recombination, as shown by the profile at 4 μs.

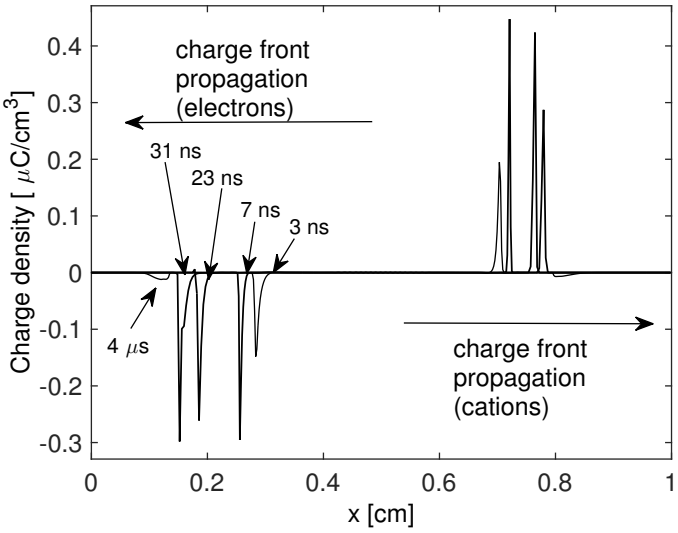

Figure 7.7: Outward propagation of charge fronts, electrons (left) and cations (right), originating from the flame zone and burned gas and enhanced by ionization.

As the fronts advance toward the electrodes at the boundaries, the electric field strength in the fresh gas increases driving a further increase in electron temperature in the fresh gases. This *compression* of the electric potential in the fresh gas introduces a length scale in the problem, since the degree of compression depends on the separation between the fronts and the boundaries where the electrodes are located. Figure 7.6 compares the electric field strength for the 1 cm domain with 9 kV applied voltage to the case of a 2 cm domain with 18 kV voltage difference (i.e. equivalent initial effective electric field strength). It is apparent that increasing the separation between the electrode and the charge front decreases the magnitude of the electric field strength increase in the fresh gas relative to the smaller domain with 9 kV.

7.4 Electric field compression

As discussed in the previous section, the enhancement of the electric field magnitude in the fresh gases as a result of charge front propagation under the action of strong electric fields is a phenomenon of interest due to its strong effect on the acceleration of electron kinetic processes, however the expense of the plasma assisted ignition simulations makes it difficult to investigate this process parametrically. One aspect of the dynamics of the charge fronts that is seemingly non-intuitive based on the simulation results is the propagation of the front containing positive charge. This front, consisting of positive ions, would be expected to translate at a speed associated with the drift velocity of ions (using a constant ion mobility in this treatment) under the action of the applied electric field. Since the mobility of ions is

orders of magnitude less than electrons the simulation results seem inconsistent. In order to investigate the parameters controlling the enhancement process, a simple analytical model was constructed. Figure 7.8 shows the charge fronts admitted during a simulation of plasma assisted ignition and an approximate representation of the charge distribution using delta functions. This approximation implicitly ignores the spatial character of the charge fronts and assumes that all charge is confined to infinitely thin regions, with the charge density being equal to zero everywhere else in the domain.

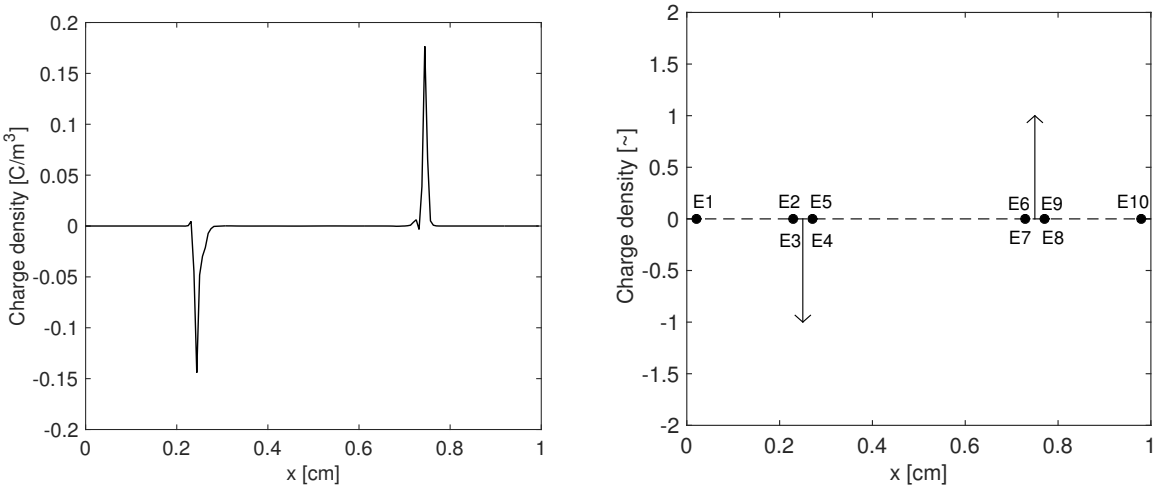

(a) (b)

Figure 7.8: (a) S3D charge fronts during pulse. (b) Conceptual model for charge fronts approximated as floating delta functions.

The charge density is initially:

$$\rho_c(x) = \begin{cases} 0, & 0 \le x \le x_1 \\ 0, & x_1 \le x \le x_2 \\ 0, & x_2 \le x \le 1 \end{cases} \tag{7.1}$$

where x_1 and x_2 are the positions of the fronts (in cm). Assuming the charge density is steady Gauss' law is posed as:

$$\frac{dE(x)}{dx} = \frac{\rho_c(x)}{\varepsilon_0} \tag{7.2}$$

which is separable and can be solved by direct integration piece-wise:

$$\int_1^2 dE = \int_1^2 \frac{\rho_c(x)}{\varepsilon_0} dx \tag{7.3}$$

For regions containing zero charge the solution is trivial:

$$E_2 - E_1 = 0 \tag{7.4}$$

$$E\left(x\right) = const \tag{7.5}$$

while integration across the infinitely thin charge fronts results in a jump condition for the electric field, E:

$$E_4 - E_3 = \frac{C}{\varepsilon_0} \tag{7.6}$$

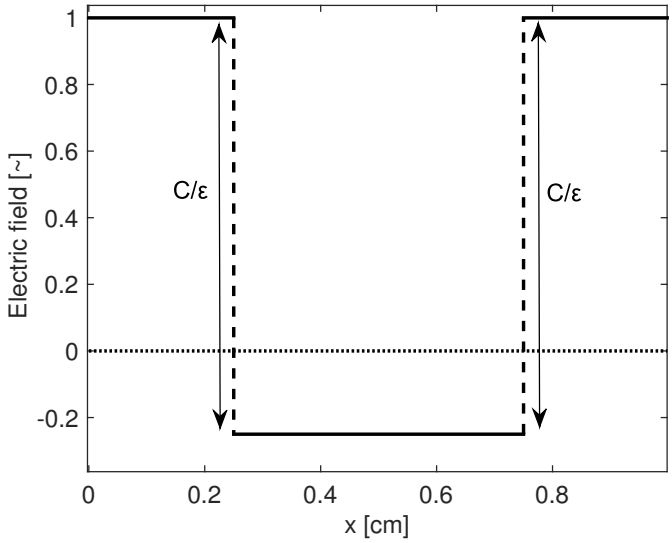

Figure 7.9: Compression electric field model

The resulting solution for the electric field across the whole domain is then characterized by regions of constant electric field (high in the fresh gases and low in the burned gases between the charge fronts) with two jumps (Fig. 7.9). The magnitude of the jumps at the charge fronts depends on the total amount of charge in the fronts themselves, which is a model parameter that is sourced from integration of the simulation solution (Fig. 7.8). Comparing the solution to the character of the electric field during the simulation (Fig. 7.7) shows that the result is qualitatively correct, with the model obviously lacking the curvature of the electric field in the charge front region due to the assumption of delta function distributed charge.

Direct integration of Gauss's law as a first-order differential equation results in a solution for the electric field to within an additive constant. Since the boundary conditions for Gauss's law are applied in the simulations as voltages, a similar methodology can be applied to the second-order form of Gauss's law for electric potential:

$$\frac{d^2\phi}{dx^2} = -\frac{\rho_c}{\varepsilon_0} \tag{7.7}$$

Integrating across the discontinuous charge fronts results in jump conditions for the slope of the potential:

$$\left.\frac{d\phi}{dx}\right|_3^4 = -\frac{C}{\varepsilon_0} \tag{7.8}$$

$$\left.\frac{d\phi}{dx}\right|_7^8 = \frac{C}{\varepsilon_0} \tag{7.9}$$

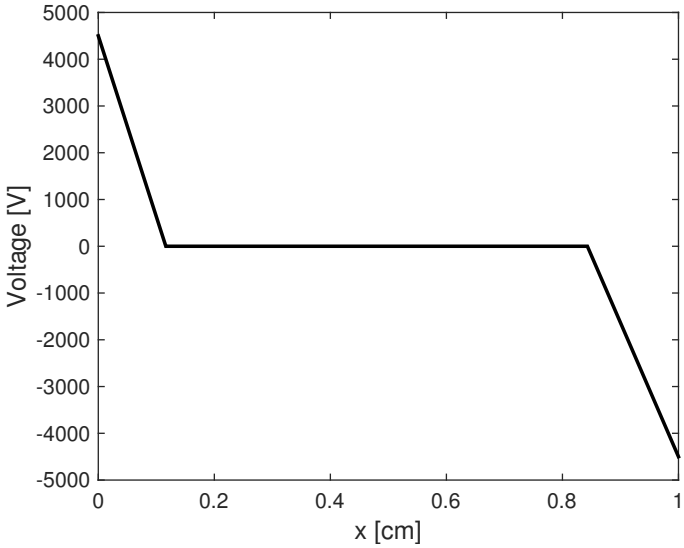

Figure 7.10: Compression voltage model

In order to determine the solution for a given choice of applied voltages, a solution algorithm based on a 'shooting method' is employed.

The solution methodology is as follows:

1. Starting from the left boundary, set the boundary voltage to the desired value, set the left front location (x_1) and the total charge in front 1

2. Guess the value of the slope of the electric potential in the fresh gas adjacent to the left boundary (this value is constant due to assumed zero charge density). Apply the jump condition to the slope at the first charge front. Since front 1 contains negative charge in this framework the jump in slope will be positive.

3. Apply the jump condition at the second charge front. Since front 2 contains positive charge in this framework the jump in slope will be negative.

4. Since the slope of the electric potential is also constant in the fresh gas adjacent to the right boundary by construction, the value of the voltage at the right boundary can be calculated by extrapolation.

5. Steps 1-4 until are then iterated (repeating the guess for the value of the slope of the electric potential in the fresh gas adjacent to the left boundary) until the correct voltage is achieved at the right boundary. Convergence to arbitrary precision is achieved using binary chops starting from two intuitive bounding guesses.

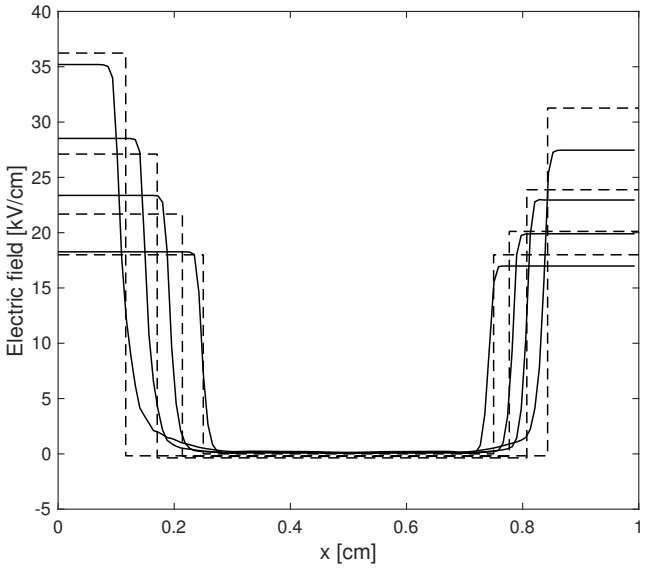

Figure 7.11: Result of transient electric compression model: dashed black lines are the results of the analytic model and the solid lines are the simulation results at equivalent times.

The model is made transient by advecting the locations of the charge fronts with a velocity determined by the drift velocity, calculated using the fresh gas electric fields and an estimate for the charge mobility in the front. The execution of this algorithm is of negligible computational expense, and thus can be repeated using many sets of input parameters in an attempt to match the simulation data. At its simplest, the model depends on only three parameters: the total charge in each front (taken to be that from the simulation and assumed to be initially equal and opposite), the mobility of charge carriers in the negative front (again taken from the simulation), and the mobility of charge carries in the positive front (prescribed in order to match the simulation data). Agreement can be constructed quite easily for a single electric field at some instant, but transient agreement (with the

charge fronts translating at speeds dependent on the effective mobility and the electric field outputted by the model) is more difficult to establish. Additional complexity was added to this analytic model by allowing the charge magnitude in the fronts themselves to grow in time in an attempt to include the effects of secondary ionization processes that generate charge. Exponential charge growth is assumed with prescribed characteristic time scale for each front (i.e. a characteristic ionization time), increasing the total number of input parameters to the model to five. With this new approach, comparison between the time evolution of the model to that of the simulation is quite good (Fig. 7.11), showing that although the simulation depends on many complex sub-models to admit a solution, the character of the electrodynamic problem that controls the evolution of the electric field can be described in quite a simple way. With this model it is possible to make estimates of maximum electric field strength for various applied potentials, in order to estimate the solver parameters necessary to set up a detailed simulation.

Nanosecond pulse chemistry

Prior to the application of the 9 kV DC pulse, the decomposition of CH_4 in the regions of the domain ahead of the propagating reactive fronts is dominated by H abstraction reactions by the radicals, OH, H, and O, with the dominant heat release pathways (as determined using the KINALC reaction pathway analysis package (Turányi, 1997)) being oxidation of CH_3 by atomic O through:

$$O + CH_3 \longleftrightarrow H + CH_2O \tag{7.10}$$

and

$$O + CH_3 \longleftrightarrow H + H_2 + CO. \tag{7.11}$$

Oxidizer decomposition is dominated by the chain branching reaction:

$$H + O_2 \longleftrightarrow O + OH. \tag{7.12}$$

For the case of unsupported ignition, these pathways persist as the primary means of decomposition and heat release up to later times. Immediately after the DC pulse is turned on, and a sufficient population of non-thermal electrons is generated, the decomposition of CH_4 occurs almost entirely by electron impact dissociation, which is represented in Fig. 7.12 at the time instant labeled '1' by the reaction:

$$e^- + CH_4 \longrightarrow e^- + CH + H_2 + H \tag{7.13}$$

while oxidizer decomposition occurs through impact ionization:

$$e^- + O_2 \longrightarrow 2\,e^- + {O_2}^+ \tag{7.14}$$

and dissociation:

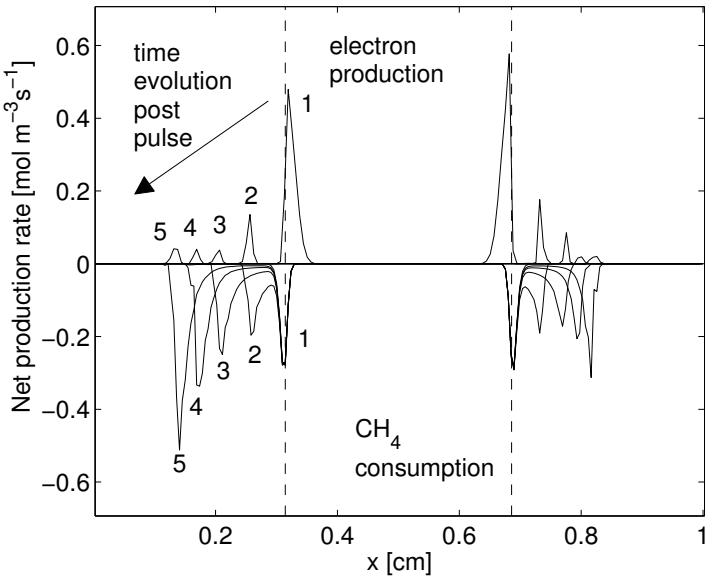

Figure 7.12: Production rate of electrons (top half plane) and consumption of CH_4 (bottom half plane) during the pulse at five time instants corresponding to 1, 4, 8, 12, and 16 ns labeled '1' to '5'. The dashed lines indicate the location of the reaction front (peak heat release rate), which does not vary during the nanoscale pulse.

$$e^- + O_2 \longrightarrow e^- + 2\,O. \tag{7.15}$$

This ionization reaction is almost entirely responsible for producing electrons at this stage of the pulse. Electron production is at a maximum at this early stage of the pulse, as shown by the time '1' electron production profile in Fig. 7.12. This can be attributed to the thermal electron pool concentrated in the flame zone prior to the pulse, which subsequently takes part in ionization reactions with abundant O_2 and N_2 in the flame zone, although primarily with O_2 due to its lower ionization energy, i.e. 12.06 eV for O_2 compared to 15.58 eV for N_2.

After 5 ns from the onset of the pulse, the charge fronts have propagated appreciably into the fresh gas and are essentially separated from the flame zones. Increasing electron energy in the fresh gases accelerates the impact excitation of abundant N_2. Analysis of the chemical pathways for the decomposition of fuel and oxidizer in the flame zones, where the electric field is now close to zero and the electron temperature is low, shows that the dominant reactions are those that were identified prior to the pulse, i.e. abstraction reactions by radicals. At this stage, fuel decomposition by electron impact reactions takes place further into the fresh gas in the vicinity of the advancing charge fronts (time 2), and the rate of CH_4 consumption in these regions is comparable to that taking place in the flame zone by radical abstraction. The consumption of fuel and oxidizer in these regions near the charge fronts arises from both electron impact dissociation as well as de-excitation reactions of electronically excited

N_2 molecules, $N_2(B_3)$, $N_2(C_3)$, and $N_2(a')$, in contrast to electron impact processes that dominated in the immediate aftermath of the pulse application. The charge density in the outwardly propagating fronts is enhanced by impact ionizations of the fresh gas neutrals, mostly the abundant N_2, which is now favored over O_2 as the electron energy is now high enough to overcome the higher ionization energy of N_2. For times 3, 4, and 5, the rate of electron production is relatively unchanged, indicating that ionization processes have not accelerated markedly despite the increase in electron energy due to the increasing electric field, but impact dissociation, and excitation and de-excitation processes do increase the magnitude of the CH_4 consumption rate from time 3 to time 5 by about a factor of 2.

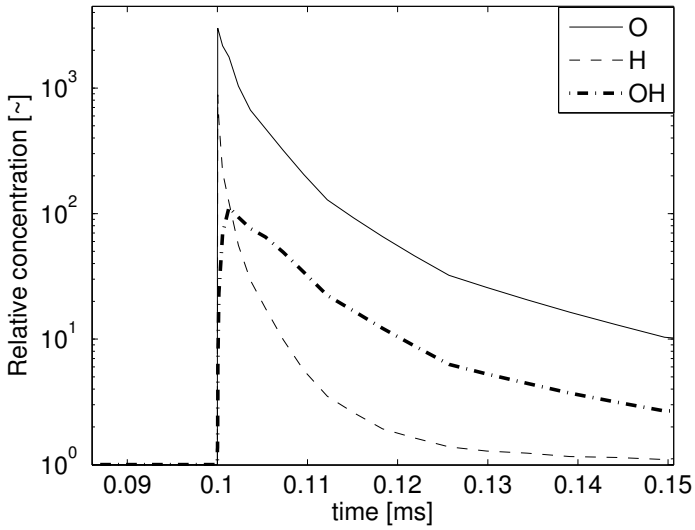

Figure 7.13: Evolution of spatially-averaged major radical species concentrations for a 35 ns pulse normalized by the evolution in the unsupported case. See commentary for details about the averaging procedure.

Radical profiles

To analyze the enhancement of radical formation in the fresh gas due to the action of the applied voltage, the radical concentrations are integrated spatially between the electrodes and a fixed location, chosen to be the locations of the reaction fronts prior to the application of the voltage pulse. Prior to the pulse, the fresh gas concentrations are essentially zero, during the pulse the concentrations of O and H build up due to non-thermal electron processes, while after the pulse these concentrations decrease due to recombination. The decrease is compensated in part by the positive contribution of diffusion from the burned gases as the flame fronts advance. Figure 7.13 shows the rapid build-up of major radicals during the application of the 35 ns pulse, with radical concentrations slowly relaxing to the values of the unsupported case post-pulse. Once the pulse is deactivated, recombination depletes

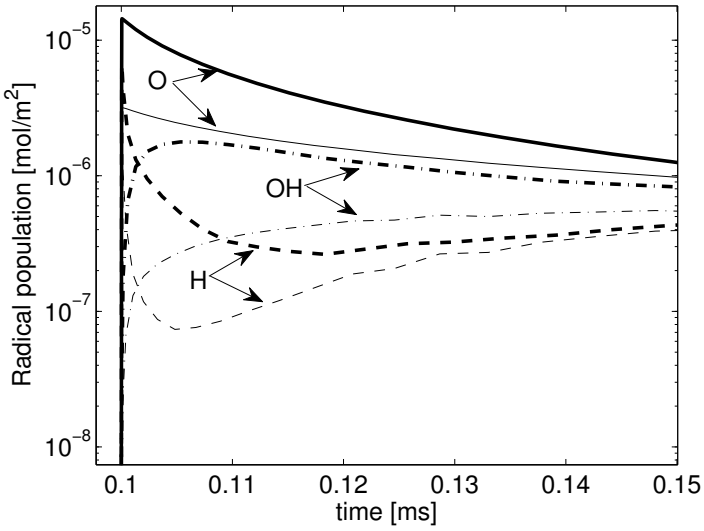

Figure 7.14: Evolution of total populations of major radical species for a 35 ns (solid lines) and 26 ns (dashed lines) pulse.

the populations of O and H rapidly, resulting in the production of OH. The O population decreases at a much slower rate post pulse than H. Comparing the 35 ns case to a shorter duration pulse (Fig. 7.14) highlights the degree to which the radical build up is sensitive to the pulse length. Shortening the pulse by approximately 25% results in a factor of 4-5 decrease in the total domain integrated radical populations.

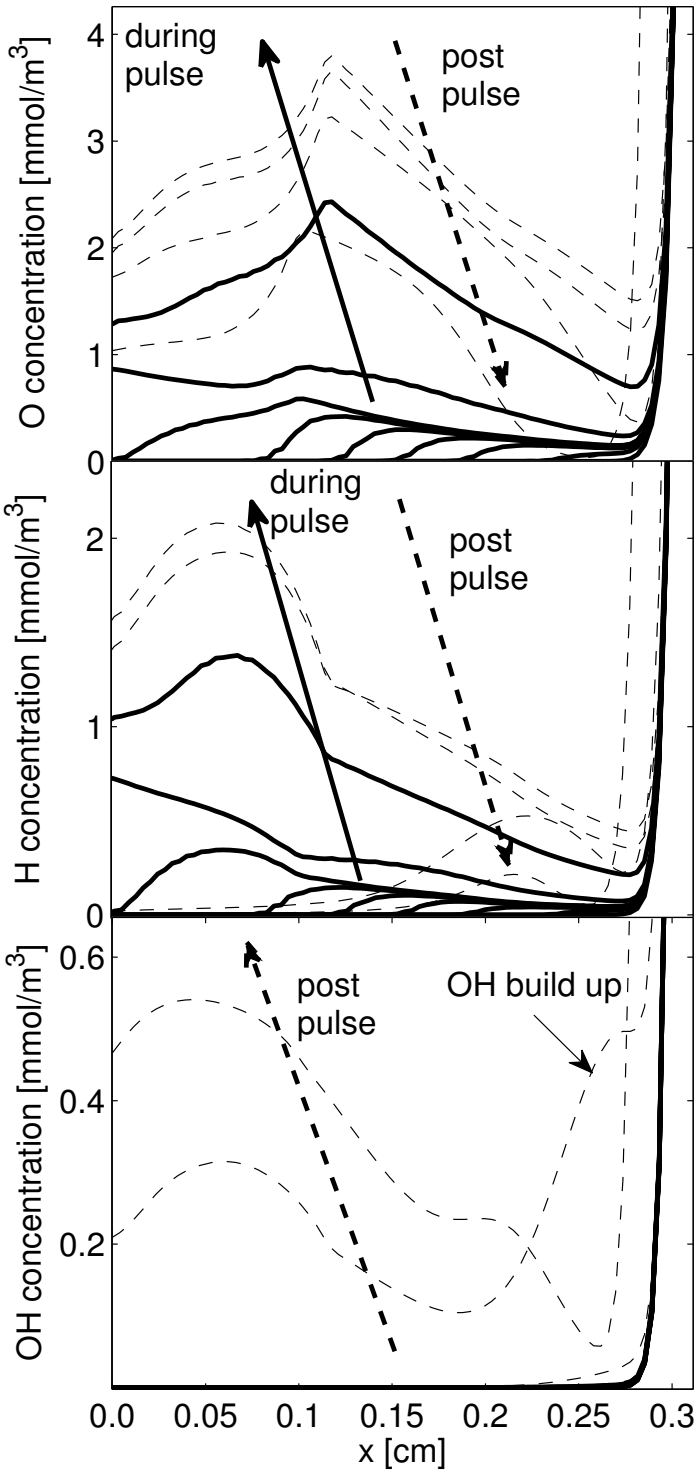

Figure 7.15: Evolution of radical species spatial profiles during the pulse (solid lines) and post pulse (dashed lines). The profiles are separated in time by 4 ns during the pulse, with the post pulse profiles taken at 1 ns, 56 ns, 1.7 μs, and 8.2 μs after the pulse has ended. The OH pool in front of the flame post pulse is entirely due to O and H recombination.

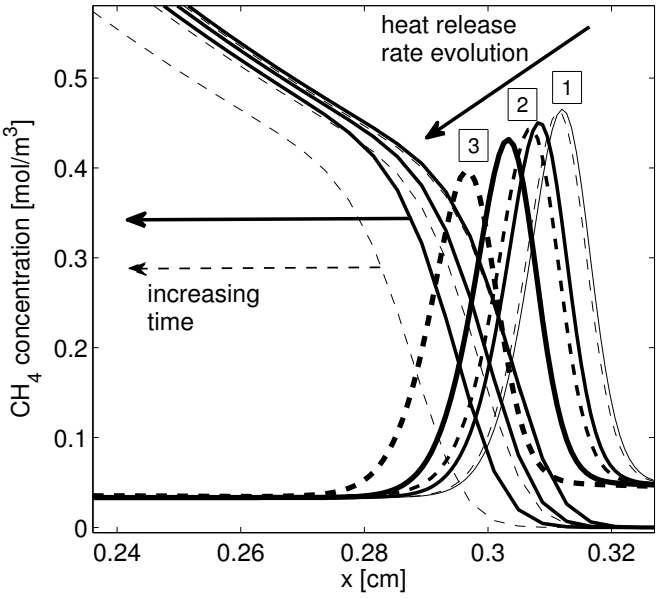

Figure 7.16: Time series of the CH_4 concentration profiles in the flame zone post pulse for the unsupported case (solid lines) and the nanosecond pulsed case (dashed lines). The profiles are taken 56 ns, 1.7 μs, and 8.2 μs after the pulse has ended. The corresponding evolution of the spatial extent of the heat release rate is plotted in arbitrary units to show the locations of the flame zone for both the unsupported and nanosecond pulsed cases).

Figure 7.15 shows the analysis of the spatial distribution of the radicals during and post pulse in the left side fresh gas, indicating that the OH concentration is unaffected in the fresh gas and close to the flame zone during the pulse when the recombination chemistry is essentially frozen, but grows post pulse as the pool of O and H radicals recombine. Figure 7.15 also shows that the contribution to overall O and H generation is mostly towards the end of the pulse, with the spatial profiles of both reaching their maxima in the regions close to the boundaries where the fresh gas electric field strength is at its highest. The populations slowly build up (solid lines) before reaching maxima in the vicinity of the boundary. The spatial character of the profiles is such that O and H deep in the fresh gas have the propensity to migrate back towards the flame zone through diffusion even as recombination is taking place. Peaks in the post pulse OH profiles occur in the vicinity of the O and H maxima but also close to the flame zone, suggesting that the balance of the radicals in this region is affected by diffusion of O and H before these are consumed in the flame zone.

The consequence of the pulse for CH_4 consumption is to advance the outward propagation of the CH_4 profile relative to the unsupported case, as shown in Fig. 7.16. The heat release rate is similarly augmented, with the heat release rate fronts in the supported case leading those in the unsupported one as they advance into the fresh gas. As the heat release rate fronts advance, their magnitudes diminish (time instants 1, 2, 3) due to the diminished heat

flux support supplied by the burned gases as the flames propagate outwards.

The total domain integrated heat release rate for the 35 ns and unsupported cases are shown in Fig. 7.17. This metric provides a measure of the enhancement of the overall reactivity. In the immediate aftermath of the pulse when the radical populations are at a maximum, the heat release rate experiences a spike, followed by a rapid and then gentle decay as radicals recombine to form OH. Once the OH population has reached a maximum post pulse (at approximately 0.105 ms as indicated in Fig. 7.14 for the 35 ns case), the heat release rate begins to decay much slower, supported by an enhanced OH pool.

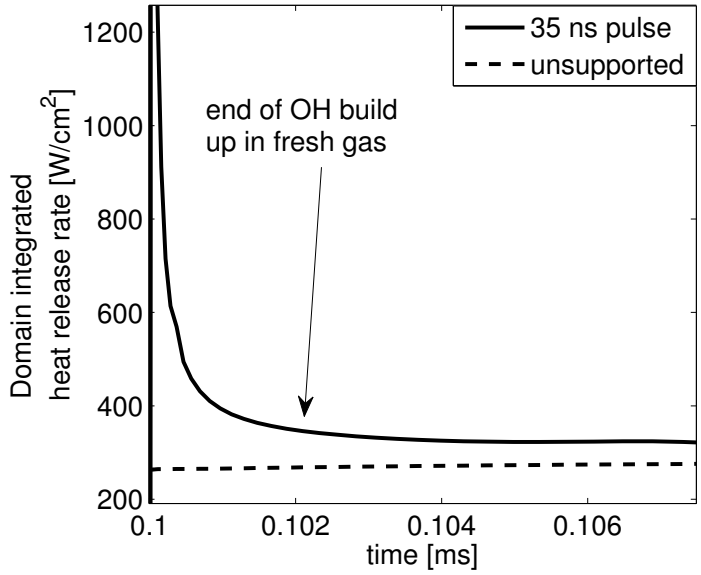

Figure 7.17: Comparison of the evolution of the domain integrated heat release rate in the post-pulse period for a 35 ns pulse (solid line) and the unsupported case (dashed line).

In addition to the chemical interactions driven by high-energy electrons, thermal energy transfer between the electrons and the neutrals and ions occur due to elastic and inelastic collisional processes, increasing the temperature of the bulk gas. The influence of these electron energy interactions was investigated by omitting these coupling terms from the right-hand-side of the bulk gas energy equation. The effect on fuel mass consumption was almost negligible, indicating that the major enhancement effect is chemical in nature.

7.5 Conclusions

The effect of a nanosecond applied voltage on a developing ignition kernel at 1 atm pressure was studied numerically using a two-fluid solver with two-temperature chemistry to represent non-thermal electron processes. Fuel and oxidizer decomposition in the fresh gases is

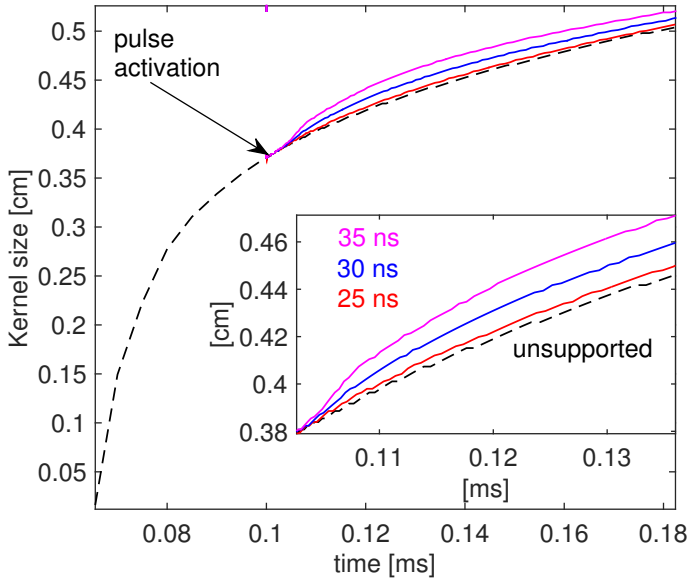

Figure 7.18: Kernel spatial development for applied nanosecond DC pulses of varying duration.

enhanced by the propagation of charge fronts introducing a dynamic electrode effect, which acts to increase the fresh gas electric field, and thus the electron energy, accelerating electron impact processes. Fuel and oxidizer fragments in the fresh gas recombine to form an enhanced pool of OH in front of the outwardly propagating flame fronts, causing an enhancement of fuel consumption. Enhanced fuel consumption (i.e. as the reaction zones eat into the fuel) results in a more rapid growth of the ignition kernel (Fig. 7.18), suggesting that kernel growth modulation and potentially interface instability (for the 2D or 3D case) and wrinkling is possible to instigate with nanosecond pulses. The relatively modest ignition enhancement by a single pulse suggests that a strategy consisting of multiple pulses in sequence may sustain an enhanced radical pool, opening up a large design space for determining optimal and novel pulsing strategies for practical regimes of interest. In closing, it is noted note that multi-dimensional simulations ultimately are required to investigate the possibility of inducing flame wrinkling or hydrodynamic instability through heat-release perturbations induced by pulsed voltages.

Chapter 8

Concluding remarks

This dissertation work demonstrates the development of a plasma solver for reacting flows for the purposes of investigating plasma assisted combustion processes. The effects of electric fields on reacting flow processes was investigated in the context of laminar flames and applied to the case of plasma assisted ignition.

8.1 Plasma solver development

A high performance direct numerical simulation solver was modified to include the functionality necessary for performing simulations of reacting plasmas. This included the development of a parallel Poisson solver using the geometric multigrid method, later to be replaced by a high performance multigrid library, the modification of chemistry functionality to account for two-temperature non-thermal plasma chemistry using a modified CHEMKIN implementation, the development of a tabulation environment for the pre-computation of electron fluid parameters associated with the electron EEDF and the fast in-situ interpolation of data tables, as well as modifications to include charged species transport, and momentum and energy coupling.

8.2 Plasma assisted ignition

Following from previous experimental insight, plasma assisted ignition of lean methane-air mixtures was chosen as a suitable test bed for investigation of plasma chemistry (using a skeletal two-temperature plasma combustion mechanism) on a reacting flow. DC voltage pulses of nanosecond duration were applied to a developing ignition kernel in a planar geometry. The effect of the nanosecond pulses was to accelerate electrons formed in the outwardly propagating reactions zones formed after the incipient ignition into the fresh gases, where they subsequently take part in ionization and impact decomposition reactions generating fuel and oxidizer fragments. These fragments persist post pulse and provide an enhanced radical pool to support heat release in the evolving kernel.

8.3 Electric compression

The propagation of charge fronts during the application of DC pulses in plasma assisted ignition augments the strength of the electric field in the fresh gases through a floating electrode effect. Referred to as 'electric field compression' in this work (due to the analogy of squeezing the linear variation in potential in a zero charge density region associated with a shrinking gap between an end electrode and a charge front), a semi-analytical approach was developed to replicate the simulation data using only a few parameters, highlighting the underlying simplicity of the electrodynamics of the problem in comparison to the complexity of the chemistry.

8.4 Comments and future directions

The performance of the solver in its current state is hindered by the range of time scales that exist in the regimes of interest. The numerical framework employed in this work is most suited for resolving highly transient phenomena such as the detailed structure of a discharge, as opposed to the large scale response of a reacting system to the time integrated effects of such phenomena. It is of interest to investigate a wide parameter space of mixtures (including heavier fuels), pressures, pulse characteristics to deduce optimal regimes of enhancement, and this parameter space is an area of current focus. The findings of Chapter 7, which indicate that the application of nanosecond pulses to a developing ignition enhances the kernel development, naturally raises the question of imposing a train of multiple pulses or extending the duration of the pulses. While the expense of the simulations makes this difficult using the current numerical framework, the implementation of stiff solvers for chemistry and transport could make the multiple pulse regime parameter space accessible. To investigate the response of laminar flames to such processes a low-Mach or all-speed formulation that would allow for the time step to be increased massively on demand would be the most appropriate way to deal with the massive change in time scales.

The characteristic boundary condition treatment employed in this work also suffers from instability when significant charge density arrives at the boundaries. Due to the global coupling enforced by Gauss' law, the presence of charge near the boundaries can result in charged species fluxes (i.e. drift fluxes) that point into the domain from outside. As a result the classical transportiveness of the boundary is violated somewhat as the required charge to balance perturbations at the boundary cannot be sourced from outside the domain. A capability that allowed for the smoothing of charge variations near boundaries would aid the stability of the solution, a fact which makes the extrapolation type boundary conditions typically employed by constant pressure solvers all the more attractive.

The spatial resolution requirements dictated by the scale of the reacting zone are often exceeded by the requirement to resolve the fronts associated with electron drift transport.

The electron density is typically not smooth when transported by strong electric fields and the effort to resolve these sharp fronts would benefit greatly from the implementation of monotonicity preserving schemes such as those used for shock-capturing in gas dynamics. Total-variation-diminishing (TVD) schemes are still not popular in the reacting flow community due to their perceived difficulty in implementation, and are mostly used in the context of detonation simulations with strong shocks. The use of such TVD schemes with high-order (e.g. the piece-wise parabolic method (Colella and Woodward, 1984)) to preserve accuracy would improve capabilities immensely.

The uncertainty associated with chemical rate parameters is an active area of concern for all reacting flow simulations and this point is particularly palpable for PAC where the electron energy dependent collision cross sections carry appreciable uncertainty. A robust sensitivity analysis of the electron impact rates, as well as the electron transport coefficients, would be useful in determining the significance of the enhancement effects observed in the simulations. More complex methodologies such as intrusive uncertainty quantification using polynomial chaos approaches would go even further to improving the understanding and limitations of this treatment of plasma chemistry.

Although the analytic model used for representing electric compression appears to work reasonably well and can predict most of the effects of charge front propagation on the electric field evolution (after some tuning of parameters), a model that took into account the spatial distribution of charge in the fronts may deliver more accurate results. Asymptotic analysis of the structure of the charge front (balancing chemistry with transport) would be useful in aiding our understanding of the evolution of the electrodynamic problem.

A simple kinetic model that could be incorporated into the chemistry functionality is a stochastic model to represent ionization by background radiation. As it stands, chemi-ionization is relied upon as the sole means for generating incipient charge at low values of E/N and this occurs in the flame zone only. The presence of a background density of charge in the fresh gases could lead to accelerated ionization on application of voltages which could alter the solution somewhat. This additional functionality would also be useful in simulating discharges in the absence of flames, e.g. corona discharge formation as a prelude to corona ignition (Fig. 1.4).

Finally, multidimensional simulation of ignition kernel development and the investigation of flame wrinkling behavior (as reported by Wolk et al. (Wolk et al., 2013)) remains a goal of this simulation effort. The expense of the simulations using the current explicit time integration framework appears to be inappropriate for this pursuit, and a framework employing stiff solvers is currently being considered for multi-dimensional extensions of this work.

Appendix A

Derivations of plasma scales

A.1 Boltzmann distributed electrons

Starting from the electron momentum equation (in the absence of collisions):

$$m_e n_e \left[\frac{\partial u_e}{\partial t} + u_e \frac{\partial u_e}{\partial x}\right] = -\frac{\partial p_e}{\partial x} - e n_e E \tag{A.1}$$

$$E = -\frac{\partial \phi}{\partial x} \tag{A.2}$$

$$p_e = n_e k_B T_e \tag{A.3}$$

$$e n_e \frac{\partial \phi}{\partial x} = \frac{\partial n_e}{\partial x} k_B T_e \tag{A.4}$$

$$e \frac{\partial \phi}{\partial x} = \frac{1}{n_e} \frac{\partial n_e}{\partial x} k_B T_e \tag{A.5}$$

$$\frac{\partial \ln n_e}{\partial x} = \frac{e \frac{\partial \phi}{\partial x}}{k_B T_e} \tag{A.6}$$

Integrating between two arbitrary points:

$$\int_1^2 \frac{\partial \ln n_e}{\partial x} dx = \int_1^2 \frac{e \frac{\partial \phi}{\partial x}}{k_B T_e} dx \tag{A.7}$$

$$\ln n_e \big|_1^2 = \frac{e\left(\phi_2 - \phi_1\right)}{k_B T_e} \tag{A.8}$$

$$n_{e2} = n_{e1} \exp\left[\frac{e\left(\phi_2 - \phi_1\right)}{k_B T_e}\right] \tag{A.9}$$

Assuming a background density n_0=n_{e1} with a corresponding zero potential:

$$n_e = n_{e0} \exp\left(\frac{-e\phi}{k_B T_e}\right) \tag{A.10}$$

A.2 Plasma frequency

Frequency information requires dynamic information, and it is convenient to proceed in Fourier space. Starting from mass continuity:

$$\frac{\partial n_e}{\partial t} + \frac{\partial n_e u_e}{\partial x} = 0 \tag{A.11}$$

Decomposing the density, velocity, and electric field into a mean and variation:

$$\begin{aligned} n_e &= n_{e0} + n_{e1} \\ u_e &= u_{e0} + u_{e1} \\ E &= E_0 + E_1 \end{aligned}$$

Expanding:

$$\frac{\partial n_{e0} + n_{e1}}{\partial t} + \frac{\partial \left(n_{e0} + n_{e1}\right)\left(u_{e0} + u_{e1}\right)}{\partial x} = 0 \tag{A.12}$$

$$\frac{\partial n_{e0} + n_{e1}}{\partial t} + \frac{\partial \left(n_{e0} u_{e0}\right)}{\partial x} + \frac{\partial \left(n_{e0} u_{e1}\right)}{\partial x} + \frac{\partial \left(n_{e1} u_{e0}\right)}{\partial x} + \frac{\partial \left(n_{e1} u_{e1}\right)}{\partial x} = 0 \tag{A.13}$$

Canceling terms and linearizing:

$$\frac{n_{e1}}{\partial t} + n_{e0}\frac{\partial u_{e1}}{\partial x} + u_{e0}\frac{\partial n_{e1}}{\partial x} = 0 \tag{A.14}$$

Fourier transforming:

$$-i\omega \hat{n}_{e1} + i n_{e0} k \hat{u}_{e1} + i u_{e0} k \hat{n}_{e1} = 0 \tag{A.15}$$

where hatted variables are Fourier coefficients.
Assuming a quiescent plasma ($u_{e0} = 0$):

$$\hat{n}_{e1} = \frac{n_{e0} k \hat{u}_{e1}}{\omega} \tag{A.16}$$

Momentum:

$$m_e n_e \left[\frac{\partial u_e}{\partial t} + u_e \frac{\partial u_e}{\partial x}\right] = -\frac{\partial p_e}{\partial x} - e n_e E \tag{A.17}$$

Expanding, and assuming a cold plasma (neglect pressure):

$$m_e \left(n_{e0} + n_{e1}\right) \left[\frac{\partial \left(u_{e0} + u_{e1}\right)}{\partial t} + \left(u_{e0} + u_{e1}\right) \frac{\partial \left(u_{e0} + u_{e1}\right)}{\partial x}\right] = -e \left(n_{e0} + n_{e1}\right) \left(E_0 + E_1\right) \tag{A.18}$$

Canceling terms and linearizing:

$$m_e n_{e0} \left[\frac{\partial u_{e1}}{\partial t} + u_{e0} \frac{\partial u_{e1}}{\partial x}\right] = -e n_{e0} E_1 \tag{A.19}$$

Fourier transforming:

$$m_e n_{e0} \left(-i\omega \hat{u}_{e1} + i u_{e0} k \hat{u}_{e1}\right) = -e n_{e0} \hat{E}_1 \tag{A.20}$$

Assuming a quiescent plasma ($u_{e0} = 0$):

$$-i m_e n_{e0} \omega \hat{u}_{e1} = -e n_{e0} \hat{E}_1 \tag{A.21}$$

$$\hat{u}_{e1} = \frac{e \hat{E}_1}{i m_e \omega} \tag{A.22}$$

Gauss' Law:

$$\varepsilon_0 \frac{\partial E}{\partial x} = e \left(n_i - n_e\right) \tag{A.23}$$

where 'i' is the (positive) ion density.
Substituting the decomposition:

$$\varepsilon_0 \frac{\partial E_1}{\partial x} = e \left(\left[n_{i0} + n_{i1}\right] - \left[n_{e0} + n_{e1}\right]\right) \tag{A.24}$$

Assuming that the plasma is homogeneous ($n_{i0} = n_{e0}$), and ions are essentially frozen ($n_{i1} = 0$):

$$\varepsilon_0 \frac{\partial E_1}{\partial x} = -e n_{e1} \tag{A.25}$$

Fourier transforming:

$$i \varepsilon_0 k \hat{E}_1 = -e \hat{n}_{e1} \tag{A.26}$$

Simplifying:

$$\hat{E}_1 = \frac{i e \hat{n}_{e1}}{\varepsilon_0 k} \tag{A.27}$$

Combining Eqs. A.16, A.22, and A.27:

$$\hat{E}_1 = \frac{ie}{\varepsilon_0 k} \frac{e\hat{E}_1}{im_e\omega} \tag{A.28}$$

Simplifying:

$$\omega = \sqrt{\frac{e^2 n_{e0}}{\varepsilon_0 m_e}} \tag{A.29}$$

which is the expression for the electron plasma frequency of non-propagating electron plasma (Langmuir) waves.

A.3 Debye length

Assuming Boltzmann distributed electrons:

$$n_e = n_{e0} \exp\left(\frac{-e\phi}{k_B T_e}\right) \tag{A.30}$$

Gauss' law:

$$\frac{d^2\phi}{dx^2} = -\frac{\rho_c}{\varepsilon_0} = -\frac{en_{e0}}{\varepsilon_0} \exp\left(\frac{-e\phi}{k_B T_e}\right) \tag{A.31}$$

Expanding the exponential:

$$\frac{d^2\phi}{dx^2} \approx -\frac{\rho_c}{\varepsilon_0} = \frac{en_{e0}}{\varepsilon_0} \exp\left(1 - \frac{e\phi}{k_B T_e}\right) \tag{A.32}$$

$$\frac{d^2\phi}{dx^2} + \frac{e^2 n_{e0}}{\varepsilon_0 k_B T_e}\phi = \frac{en_{e0}}{\varepsilon_0} \tag{A.33}$$

This is a harmonic equation with eigenvalue $\sqrt{\frac{e^2 n_{e0}}{\varepsilon_0 k_B T_e}}$ corresponding to the characteristic wavelength of a spatial osscilation.

The corresponding length scale is the Debye length, defined as:

$$\lambda_D = \sqrt{\frac{\varepsilon_0 k_B T_e}{e^2 n_{e0}}} \tag{A.34}$$

A.4 Dielectric relaxation time

Starting from electron continuity:

$$\frac{\partial n_e}{\partial t} + \frac{\partial n_e u_e}{\partial x} = 0 \tag{A.35}$$

Assuming the electron flux ($j_e = n_e u_e$) is dominated by a drift component:

$$j_e = -\mu_e n_e E \tag{A.36}$$

Assuming that the ion density is homogenous and frozen, charge perturbations (and thus perturbations in potential) are due to perturbations in the electron density only:

$$\begin{aligned} n_e &= n_{e0} + n_{e1} \\ E &= E_0 + E_1 \\ \rho_{c1} &= -n_{e1} e \end{aligned}$$

resulting in the expression for electron continuity:

$$\frac{\partial \left[n_{e0} + n_{e1}\right]}{\partial t} - \frac{\partial \mu_e \left[n_{e0} + n_{e1}\right] \left[E_0 + E_1\right]}{\partial x} = 0 \tag{A.37}$$

Simplifying (e.g. assuming constant mobility, zero background electric field) and linearizing:

$$\frac{\partial n_{e1}}{\partial t} = \mu_e n_{e0} \frac{\partial E_1}{\partial x} \tag{A.38}$$

Gauss' law in 1D then takes the form (for electric field):

$$\frac{\partial E_1}{\partial x} = -\frac{n_{e1} e}{\varepsilon_0} \tag{A.39}$$

Combining the two above expressions to form an expression for the evolution of a charge perturbation:

$$\frac{\partial \rho_{c1}}{\partial t} = -\frac{\mu_e n_{e0}}{\varepsilon_0} \rho_{c1} \tag{A.40}$$

This is a decay equation with characteristic time:

$$\tau_d = \frac{\varepsilon_0}{\mu_e n_{e0}} \tag{A.41}$$

Substituting using the definition of the mobility and isolating the electric permittivity from the definition of the electron plasma frequency:

$$\tau_d = \frac{\nu_{en}}{\omega_p^2} \tag{A.42}$$

which is the characteristic time of decay of perturbations in charge (and thus potential) under the action of collisions, i.e. the dielectric relaxation time.

A.5 Einstein relation

Starting from Boltzmann distributed species:

$$n_k = n_{k0} \exp\left(\frac{qe\phi}{k_B T}\right) \tag{A.43}$$

Taking the spatial gradient, assuming a uniform temperature field on the scale of the electric potential:

$$\nabla n_k = \frac{qe}{k_B T} n_{k0} \exp\left(\frac{qe\phi}{k_B T}\right) \tag{A.44}$$

Simplifying:

$$\nabla n_k = \frac{qe}{k_B T} n_k \tag{A.45}$$

Posing a drift-diffusion mass flux:

$$j_k = q\mu_k n_k \nabla\phi - D_k \nabla n_k \tag{A.46}$$

At equilibrium:

$$j_k = 0 \tag{A.47}$$

Equating the flux components:

$$\frac{qeD_k n_k \nabla\phi}{k_B T} = q\mu_k n_k \nabla\phi \tag{A.48}$$

Simplifying, delivers an expression for the diffusivity:

$$D_k = \frac{\mu_k k_B T}{e} \tag{A.49}$$

Appendix B

Parallel multigrid solver

Files:
main.f90 (driver)
multigrid_m.f90 (fuction module)
output_m.f90 (i/o module)
precision_m.f90 (floating point precision specification module)

main.f90:

```
!================================
! USE GEOMETRIC MULTIGRID TO SOLVE POISSON'S EQUATION IN PARALLEL FOR A 1D
    DOMAIN
!(example right hand side is a single wavelength sine wave)
!================================

program main
use output_m
use multigrid_m
implicit none
include 'mpif.h'

integer::ierr
integer::procID,numproc
!grid parameters
integer:: nx !the total number of grid intervals, points
integer:: mx !the number of points in each mpi domain
real*8 ::ghostl,ghostr
!grid
real*8, allocatable:: x(:)
real*8, allocatable:: rhs(:)
real*8, allocatable:: rhs_pad2(:)
real*8, allocatable:: a(:)
real*8, allocatable:: a_pad2(:)
```

```
real*8, allocatable:: LOfPhi(:)
real*8, allocatable:: residual(:)
real*8::h,mu

!misc
real*8:: pi = 4.d0*DATAN(1.d0);
integer::i,j,k,req
character(len=20) ::filename
character(len=20) ::numasstring !number as string
integer:: flag,numV,nrelax

flag=1
numV=2
nrelax=3

!set up communication to other processors
call MPI_Init(ierr)
call MPI_Comm_rank(MPI_COMM_WORLD,procID,ierr)
call MPI_Comm_size(MPI_COMM_WORLD,numproc,ierr)


!read in details about the grid
open(file='./input',unit=99,form='formatted',status='old')
read(99,*) nx !the number of grid intervals !(default is 832 points)
close(99)


write(numasstring,'(I3)') procID
call open_output('./outfiles/file'//trim(adjustl(numasstring))//'.dat',procID)


!the number of grid points on this mpi domain
mx = nx/numproc !need this to divide evenly
!create space for grid and rhs
allocate(x(mx))
allocate(rhs(mx))
allocate(a(mx))
allocate(LOfPhi(mx))
allocate(residual(mx))
allocate(a_pad2(mx+2))
allocate(rhs_pad2(mx+2))
!fill x, where the grid ranges from 0 to 2*pi
do i=1,mx
x(i) = ( i+procID*mx  -1 )*2*pi/(nx-1)
!============
!SPECIFY THE RIGHT HAND SIDE FUNCTION
rhs(i)= sin( x(i) )
!============
a(i)=0.0
enddo
```

```
74 !uniform grid spacing
75 h=x(2)-x(1)
76 ghostr=0.0
77 ghostl=0.0
78
79
80 write(*,*) 'solver start, processor #',procID
81 do j=1,4000
82
83
84 if (numproc.gt.1) then
85
86
87 !identify values from neigbors
88
89 !SENDS
90 if (procID.eq.0) then
91         call MPI_SEND(a(mx),1,MPI_REAL8,procID+1,2,MPI_COMM_WORLD,req,ierr)
92 endif
93 if (procID.eq.numproc-1) then
94         call MPI_SEND(a(1),1,MPI_REAL8,procID-1,2,MPI_COMM_WORLD,req,ierr)
95
96 end if
97
98 if (procID.gt.0 .and. procID.lt.numproc-1) then
99         call MPI_SEND(a(mx),1,MPI_REAL8,procID+1,2,MPI_COMM_WORLD,req,ierr)
100 end if
101
102
103 !WAIT FOR SENDS TO COMPLETE
104
105
106 !RECEIVES
107 if (procID.eq.0) then
108         call MPI_RECV(ghostr,1,MPI_REAL8,procID+1,2,MPI_COMM_WORLD,req,ierr)
109 endif
110
111 if (procID.eq.numproc-1) then
112         call MPI_RECV(ghostl,1,MPI_REAL8,procID-1,2,MPI_COMM_WORLD,req,ierr)
113
114 end if
115
116 if (procID.gt.0 .and. procID.lt.numproc-1) then
117         call MPI_RECV(ghostr,1,MPI_REAL8,procID+1,2,MPI_COMM_WORLD,req,ierr)
118         call MPI_RECV(ghostl,1,MPI_REAL8,procID-1,2,MPI_COMM_WORLD,req,ierr)
119
120 end if
121
122 endif
123
```

```
124
125 !perform point relaxation
126 mu = h**2 /8.0
127 if (procID.eq.0) then
128
129 if (flag.eq.1) then
130
131 !MULTIGRID
132 !construct
133 do i=1,mx
134 a_pad2(i+1)=a(i)
135 rhs_pad2(i+1)=rhs(i)
136 enddo
137 a_pad2(1)=0.0
138 a_pad2(mx+2)=ghostr
139 rhs_pad2(1)=0.0
140 rhs_pad2(mx+2)=0.0
141
142 do k=1,numV !V-cycle
143 call multigrid(a_pad2,rhs_pad2,h,mx+1,nrelax)
144 do i=1,mx
145 a(i)=a_pad2(i+1)
146 end do
147 do i=1,mx
148 a_pad2(i+1)=a(i)
149 enddo
150 a(1)=0.0 !bug, enforce this
151 enddo
152
153 endif
154
155 if (flag.eq.2) then
156
157
158 !JACOBI
159 do i=2,mx-1
160 LOfPhi(i) = (a(i-1) +a(i+1) - 2*a(i) )/h**2
161 enddo
162 do i=2,mx-1
163 a(i) = a(i) + mu*( LOfPhi(i) -rhs(i) )
164 enddo
165
166 endif
167
168 if (flag.eq.3) then
169
170 !GAUSS-SEIDEL
171 do i=2,mx-1
172 LOfPhi(i) = (a(i-1) +a(i+1) - 2*a(i) )/h**2
173 a(i) = a(i) + mu*( LOfPhi(i) -rhs(i) )
```

```
174 enddo
175
176 endif
177
178 if (flag.eq.4) then
179
180 !GSRB
181 !red
182 do i=2,mx-1,2
183 LOfPhi(i) = (a(i-1) +a(i+1) - 2*a(i) )/h**2
184 a(i) = a(i) + mu*( LOfPhi(i) -rhs(i) )
185 end do
186 !black
187 do i=3,mx-1,2
188 LOfPhi(i) = (a(i-1) +a(i+1) - 2*a(i) )/h**2
189 a(i) = a(i) + mu*( LOfPhi(i) -rhs(i) )
190 end do
191
192 endif
193
194 LOfPhi(mx) = (a(mx-1) +ghostr - 2*a(mx) )/h**2
195 a(mx) = a(mx) + mu*( LOfPhi(mx) -rhs(mx) )
196
197 endif
198
199 if (procID.eq.numproc-1) then
200
201 if (flag.eq.1) then
202 !MULTIGRID
203 !construct
204 do i=1,mx
205 a_pad2(i+1)=a(i)
206 rhs_pad2(i+1)=rhs(i)
207 enddo
208 a_pad2(1)=ghostl
209 a_pad2(mx+2)=0
210 rhs_pad2(1)=0.0
211 rhs_pad2(mx+2)=0.0
212
213 do k=1,numV !V-cycle
214 call multigrid(a_pad2,rhs_pad2,h,mx+1,nrelax)
215 do i=1,mx
216 a(i)=a_pad2(i+1)
217 end do
218 do i=1,mx
219 a_pad2(i+1)=a(i)
220 enddo
221 end do
222
223 endif
```

```
224
225 if (flag.eq.2) then
226 !JACOBI
227 do i=2,mx-1
228 LOfPhi(i) = (a(i-1) +a(i+1) - 2*a(i) )/h**2
229 enddo
230 do i=2,mx-1
231 a(i) = a(i) + mu*( LOfPhi(i) -rhs(i) )
232 enddo
233
234 end if
235
236 if (flag.eq.3) then
237 !GAUSS-SEIDEL
238 do i=2,mx-1
239 LOfPhi(i) = (a(i-1) +a(i+1) - 2*a(i) )/h**2
240 a(i) = a(i) + mu*( LOfPhi(i) -rhs(i) )
241 enddo
242
243 endif
244
245 if (flag.eq.4) then
246
247 !GSRB
248 !red
249 do i=2,mx-1,2
250 LOfPhi(i) = (a(i-1) +a(i+1) - 2*a(i) )/h**2
251 a(i) = a(i) + mu*( LOfPhi(i) -rhs(i) )
252 end do
253 !black
254 do i=3,mx-1,2
255 LOfPhi(i) = (a(i-1) +a(i+1) - 2*a(i) )/h**2
256 a(i) = a(i) + mu*( LOfPhi(i) -rhs(i) )
257 enddo
258
259 endif
260
261 LOfPhi(1) = (ghostl +a(2) - 2*a(1) )/h**2
262 a(1) = a(1) + mu*( LOfPhi(1) -rhs(1) )
263
264 endif
265
266 if (procID.gt.0 .and. procID.lt.numproc-1) then
267
268 if (flag.eq.1) then
269 !MULTIGRID
270 !construct
271 do i=1,mx
272 a_pad2(i+1)=a(i)
273 rhs_pad2(i+1)=rhs(i)
```

```
274 enddo
275 a_pad2(1)=ghostl
276 a_pad2(mx+2)=ghostr
277 rhs_pad2(1)=0.0
278 rhs_pad2(mx+2)=0.0
279
280 do k=1,numV !V-cycle
281 call multigrid(a_pad2,rhs_pad2,h,mx+1,nrelax)
282 do i=1,mx
283 a(i)=a_pad2(i+1)
284 end do
285 do i=1,mx
286 a_pad2(i+1)=a(i)
287 enddo
288 end do
289
290 end if
291
292 if (flag.eq.2) then
293 !JACOBI
294 do i=2,mx-1
295 LOfPhi(i) = (a(i-1) +a(i+1) - 2*a(i) )/h**2
296 enddo
297 do i=2,mx-1
298 a(i) = a(i) + mu*( LOfPhi(i) -rhs(i) )
299 enddo
300 end if
301
302 if (flag.eq.3) then
303 !GAUSS-SEIDEL
304 do i=2,mx-1
305 LOfPhi(i) = (a(i-1) +a(i+1) - 2*a(i) )/h**2
306 a(i) = a(i) + mu*( LOfPhi(i) -rhs(i) )
307 enddo
308
309 end if
310
311
312 if (flag.eq.4) then
313 !GSRB
314 !red
315 do i=2,mx-1,2
316 LOfPhi(i) = (a(i-1) +a(i+1) - 2*a(i) )/h**2
317 a(i) = a(i) + mu*( LOfPhi(i) -rhs(i) )
318 end do
319 !red
320 do i=3,mx-1,2
321 LOfPhi(i) = (a(i-1) +a(i+1) - 2*a(i) )/h**2
322 a(i) = a(i) + mu*( LOfPhi(i) -rhs(i) )
323 end do
```

```
324 end if
325
326 LOfPhi(mx) = (a(mx-1) +ghostr - 2*a(mx) )/h**2
327 a(mx) = a(mx) + mu*( LOfPhi(mx) -rhs(mx) )
328
329 LOfPhi(1) = (ghostl +a(2) - 2*a(1) )/h**2
330 a(1) = a(1) + mu*( LOfPhi(1) -rhs(1) )
331
332 endif
333
334
335 enddo
336 write(*,*) 'solver finish, processor #',procID
337
338 !write my component of solution to file
339 do i=1,mx
340 write(procID,*) x(i),a(i),rhs(i)
341 end do
342
343 !terminate mpi execution environment - all processes must call this routine
344 !before exiting
345 call MPI_Finalize(ierr)
346
347 call close_output(procID)
348
349 end program main
```

multigrid_m.f90:

```
1  module multigrid_m
2  implicit none
3
4  contains
5
6
7  recursive subroutine multigrid(a_phi,a_rhs,a_h,a_N,a_nrelax)
8  integer, intent(in) ::a_N, a_nrelax
9  real*8,intent(inout),dimension(a_N+1) ::a_phi
10 real*8,intent(in),dimension(a_N+1) ::a_rhs
11 real*8,intent(in) ::a_h
12 !locals
13 real*8 ::hc
14 integer ::Nc
15 real*8,dimension(a_N+1) :: m_res,m_LOfPhi
16 real*8,dimension(a_N/2 +1) :: m_delta
17 real*8,dimension(a_N/2 +1) :: m_resc
```

```
18 integer ::i
19
20
21 !do point relaxation
22 call pointRelax(a_phi,a_rhs,a_nrelax,a_h,a_N)
23
24
25 if (a_N.le.3) then
26 return
27
28 else
29
30 hc=2.0*a_h
31 Nc=(a_N)/2
32
33 !initialize coarse arrays
34 do i=1,Nc+1
35 m_delta(i)=0.0
36 m_resc(i)=0.0
37 end do
38
39 !apply the operator pointwise
40 call applyOp(m_LOfPhi,a_phi,a_h,a_N)
41
42 !calculate the residual
43 do i=1,a_N+1
44 m_res(i) = a_rhs(i) -m_LOfPhi(i)
45 end do
46 !write(*,*) 'max(abs(m_res))= ',maxval(abs(m_res))
47
48 !restrict the residual down to the coarse grid
49 call restrict(m_res,m_resc,a_N,Nc)
50
51 !recursively call multigrid
52 call multigrid(m_delta,m_resc,hc,Nc,a_nrelax)
53
54 !interpolate residual back onto the fine grid (adding) on the way back up
55 call interp(a_phi,m_delta,a_N,Nc)
56
57 !do point relaxation
58 call pointRelax(a_phi,a_rhs,a_nrelax,a_h,a_N)
59
60 end if
61
62 end subroutine multigrid
63
64
65 subroutine interp(a_phi,a_delta,a_N,a_Nc)
66 implicit none
67 integer, intent(in) :: a_N,a_Nc
```

```
68 real*8, intent(inout),dimension(a_N+1) ::a_phi
69 real*8, intent(in),dimension(a_Nc+1) ::a_delta
70 !locals
71 integer :: i
72
73
74 do i=2,a_Nc+1
75 a_phi(2*i-1) =a_phi(2*i-1) +a_delta(i)
76 a_phi(2*i-2) = a_phi(2*i-2) + ( a_delta(i) +a_delta(i-1) )/2
77 end do
78
79 end subroutine interp
80
81
82 subroutine restrict(a_res,a_resc,a_N,a_Nc)
83 implicit none
84 integer, intent(in) :: a_N, a_Nc
85 real*8, intent(in), dimension(a_N+1) :: a_res
86 real*8, intent(inout), dimension(a_Nc+1) :: a_resc
87 !locals
88 integer ::i
89
90 do i=2,a_Nc !skip the boundary points
91 a_resc(i) = a_res(2*i-1)
92 enddo
93
94 end subroutine restrict
95
96
97 subroutine applyOp(a_LOfPhi,a_phi,a_h,a_N)
98 implicit none
99 integer ,intent(in) ::a_N
100 real*8, intent(in), dimension(a_N+1) ::a_phi
101 real*8,intent(inout),dimension(a_N+1) ::a_LOfPhi
102 real*8,intent(in) ::a_h
103 !locals
104 integer :: i
105
106 !initialize LOfPhi
107 a_LOfPhi(:)=0.0
108 do i=2,a_N !do not define operator on the boundaries
109 a_LOfPhi(i) = (a_phi(i-1) + a_phi(i+1) -2*a_phi(i) )/(a_h**2)
110 end do
111
112 end subroutine applyOp
113
114
115 subroutine pointRelax(a_phi,a_rhs,a_nrelax,a_h,a_N)
116 implicit none
117 real*8, intent(in) ::a_h
```

```
118 integer, intent(in) :: a_nrelax,a_N
119 real*8 ::mu
120 real*8,intent(inout),dimension(a_N+1) ::a_phi
121 real*8,intent(in),dimension(a_N+1) ::a_rhs
122 !locals
123 real*8 ::m_LOfPhi(size(a_phi))
124 integer ::i,j
125
126
127 mu = a_h**2 / 8.0d0
128 !do nrelax iterations of relaxation on each point
129 do i=1,a_nrelax
130 !apply the operator
131 call applyOp(m_LOfPhi,a_phi,a_h,a_N)
132
133 do j=2,a_N
134 a_phi(j) =a_phi(j) + mu*( m_LOfPhi(j) -a_rhs(j) )
135 end do
136
137 end do
138
139 end subroutine pointRelax
140
141
142 end module multigrid_m
```

output_m.f90:

```
1 module output_m
2 use precision_m
3 implicit none
4
5 contains
6
7
8 subroutine open_output(path,out_unit)
9 implicit none
10 character (len=*) :: path
11 integer ::out_unit
12
13 open(unit=out_unit, file=trim(path),form='formatted',status='replace')
14
15 end subroutine open_output
16
17
18 subroutine close_output(out_unit)
```

```
19 implicit none
20 integer ::out_unit
21
22 close(out_unit)
23
24 end subroutine close_output
25
26 end module output_m
```

precision_m.f90:

```
1 module precision_m
2
3 integer, parameter :: wp = SELECTED_REAL_KIND(15,307)
4 integer, parameter :: long_int = SELECTED_INT_KIND(15)
5
6 end module precision_m
```

Appendix C

Skeletal two-temperature plasma combustion mechanism

For rate constants specified in Arhennius form, the data are pre-exponential factor (A, [cm^3 mol^{-1} s^{-1}], temperature dependence exponent (n), and activation energy E_a, [J mol^{-1}]).

For rate coefficients of electron impact reactions, the data are coefficients for the Janev-Evans-Post (Janev et al., 1987) form.

```
! CHEMKIN formatted plasma skeletal mechanism with 43 species and 514 steps
ELEMENTS
 O   H   C   N   E
END
SPECIES
N2(C3)    CH        N2^+      N2(ap)    N2(B3)    CH4^+     O2(A3)    O2^+
H^-       O^-       O2(vib4)  O(1D)     O2^-      O2(vib3)  O2        N
O2(vib2)  N2(vib5)  O2(b1)    N2(vib4)  CH3O      HCO       C2H5      CH3OH
O         HO2       O2(a1)    OH        N2(vib1)  H         C2H2      CH2CO
C2H6      CO2       C2H4      CH2O      CH3       H2        CO        H2O
CH4       N2        HCO+      H3O+      E
END
REACTIONS
2O+M<=>O2+M                       1.2000E+17  -1.000  0.0000E+00
 C2H6/ 3.00/ CO2/ 3.60/ H2/ 2.40/ CO/ 1.75/ H2O/15.40/ CH4/ 2.00/
O+H+M<=>OH+M                      5.0000E+17  -1.000  0.0000E+00
 C2H6/ 3.00/ CO2/ 2.00/ H2/ 2.00/ CO/ 1.50/ H2O/ 6.00/ CH4/ 2.00/
O+H2<=>H+OH                       3.8700E+04   2.700  6.2600E+03
O+HO2<=>OH+O2                     2.0000E+13   0.000  0.0000E+00
O+CH<=>H+CO                       5.7000E+13   0.000  0.0000E+00
```

```
O+CH3<=>H+CH2O                  5.0600E+13   0.000  0.0000E+00
O+CH4<=>OH+CH3                  1.0200E+09   1.500  8.6000E+03
O+CO(+M)<=>CO2(+M)              1.8000E+10   0.000  2.3850E+03
 LOW/  6.0200E+14   0.000  3.0000E+03 /
 C2H6/ 3.00/ CO2/ 3.50/ H2/ 2.00/ CO/ 1.50/ H2O/ 6.00/ CH4/ 2.00/ O2/ 6.00/
O+HCO<=>OH+CO                   3.0000E+13   0.000  0.0000E+00
O+HCO<=>H+CO2                   3.0000E+13   0.000  0.0000E+00
O+CH2O<=>OH+HCO                 3.9000E+13   0.000  3.5400E+03
O+CH3O<=>OH+CH2O                1.0000E+13   0.000  0.0000E+00
O+CH3OH<=>OH+CH3O               1.3000E+05   2.500  5.0000E+03
O+C2H4<=>CH3+HCO                1.2500E+07   1.830  2.2000E+02
O+C2H5<=>CH3+CH2O               2.2400E+13   0.000  0.0000E+00
O+C2H6<=>OH+C2H5                8.9800E+07   1.920  5.6900E+03
O2+CO<=>O+CO2                   2.5000E+12   0.000  4.7800E+04
O2+CH2O<=>HO2+HCO               1.0000E+14   0.000  4.0000E+04
H+O2+M<=>HO2+M                  2.8000E+18  -0.860  0.0000E+00
 C2H6/ 1.50/ CO2/ 1.50/ CO/ 0.75/ H2O/ 0.00/ O2/ 0.00/ N2/ 0.00/
H+2O2<=>HO2+O2                  2.0800E+19  -1.240  0.0000E+00
H+O2+H2O<=>HO2+H2O              1.1260E+19  -0.760  0.0000E+00
H+O2+N2<=>HO2+N2                2.6000E+19  -1.240  0.0000E+00
H+O2<=>O+OH                     2.6500E+16  -0.670  1.7041E+04
2H+M<=>H2+M                     1.0000E+18  -1.000  0.0000E+00
 C2H6/ 3.00/ CO2/ 0.00/ H2/ 0.00/ H2O/ 0.00/ CH4/ 2.00/
2H+H2<=>2H2                     9.0000E+16  -0.600  0.0000E+00
2H+H2O<=>H2+H2O                 6.0000E+19  -1.250  0.0000E+00
2H+CO2<=>H2+CO2                 5.5000E+20  -2.000  0.0000E+00
H+OH+M<=>H2O+M                  2.2000E+22  -2.000  0.0000E+00
 C2H6/ 3.00/ H2/ 0.73/ H2O/ 3.65/ CH4/ 2.00/
H+HO2<=>O+H2O                   3.9700E+12   0.000  6.7100E+02
H+HO2<=>O2+H2                   4.4800E+13   0.000  1.0680E+03
H+HO2<=>2OH                     8.4000E+13   0.000  6.3500E+02
H+CH3(+M)<=>CH4(+M)             1.3900E+16  -0.530  5.3600E+02
 LOW/  2.6200E+33  -4.760  2.4400E+03 /
 TROE/ 0.7830      74.00      2941.      6964.     /
 C2H6/ 3.00/ CO2/ 2.00/ H2/ 2.00/ CO/ 1.50/ H2O/ 6.00/ CH4/ 3.00/
H+CH4<=>CH3+H2                  6.6000E+08   1.620  1.0840E+04
H+HCO(+M)<=>CH2O(+M)            1.0900E+12   0.480 -2.6000E+02
 LOW/  2.4700E+24  -2.570  4.2500E+02 /
 TROE/ 0.7824      271.0      2755.      6570.     /
 C2H6/ 3.00/ CO2/ 2.00/ H2/ 2.00/ CO/ 1.50/ H2O/ 6.00/ CH4/ 2.00/
H+HCO<=>H2+CO                   7.3400E+13   0.000  0.0000E+00
H+CH2O(+M)<=>CH3O(+M)            5.4000E+11   0.450  2.6000E+03
```

```
 LOW/  2.2000E+30  -4.800  5.5600E+03 /
 TROE/ 0.7580      94.00      1555.      4200.     /
 C2H6/ 3.00/ CO2/ 2.00/ H2/ 2.00/ CO/ 1.50/ H2O/ 6.00/ CH4/ 2.00/
H+CH2O<=>HCO+H2                 5.7400E+07   1.900  2.7420E+03
H+CH3O(+M)<=>CH3OH(+M)          2.4300E+12   0.510  5.0000E+01
 LOW/  4.6600E+41  -7.440  1.4080E+04 /
 TROE/ 0.7000      100.0     0.9000E+05 0.1000E+05 /
 C2H6/ 3.00/ CO2/ 2.00/ H2/ 2.00/ CO/ 1.50/ H2O/ 6.00/ CH4/ 2.00/
H+CH3O<=>H2+CH2O                2.0000E+13   0.000  0.0000E+00
H+CH3O<=>OH+CH3                 1.5000E+12   0.500 -1.1000E+02
H+CH3OH<=>CH3O+H2               4.2000E+06   2.100  4.8700E+03
H+C2H4(+M)<=>C2H5(+M)           5.4000E+11   0.450  1.8200E+03
 LOW/  6.0000E+41  -7.620  6.9700E+03 /
 TROE/ 0.9753      210.0      984.0      4374.     /
 C2H6/ 3.00/ CO2/ 2.00/ H2/ 2.00/ CO/ 1.50/ H2O/ 6.00/ CH4/ 2.00/
H+C2H5(+M)<=>C2H6(+M)           5.2100E+17  -0.990  1.5800E+03
 LOW/  1.9900E+41  -7.080  6.6850E+03 /
 TROE/ 0.8422      125.0      2219.      6882.     /
 C2H6/ 3.00/ CO2/ 2.00/ H2/ 2.00/ CO/ 1.50/ H2O/ 6.00/ CH4/ 2.00/
H+C2H5<=>H2+C2H4                2.0000E+12   0.000  0.0000E+00
H+C2H6<=>C2H5+H2                1.1500E+08   1.900  7.5300E+03
H+CH2CO<=>CH3+CO                1.1300E+13   0.000  3.4280E+03
H2+CO(+M)<=>CH2O(+M)            4.3000E+07   1.500  7.9600E+04
 LOW/  5.0700E+27  -3.420  8.4350E+04 /
 TROE/ 0.9320      197.0      1540.     0.1030E+05 /
 C2H6/ 3.00/ CO2/ 2.00/ H2/ 2.00/ CO/ 1.50/ H2O/ 6.00/ CH4/ 2.00/
OH+H2<=>H+H2O                   2.1600E+08   1.510  3.4300E+03
2OH<=>O+H2O                     3.5700E+04   2.400 -2.1100E+03
OH+HO2<=>O2+H2O                 1.4500E+13   0.000 -5.0000E+02
DUPLICATE
OH+CH<=>H+HCO                   3.0000E+13   0.000  0.0000E+00
OH+CH3(+M)<=>CH3OH(+M)          2.7900E+18  -1.430  1.3300E+03
 LOW/  4.0000E+36  -5.920  3.1400E+03 /
 TROE/ 0.4120      195.0      5900.      6394.     /
 C2H6/ 3.00/ CO2/ 2.00/ H2/ 2.00/ CO/ 1.50/ H2O/ 6.00/ CH4/ 2.00/
OH+CH4<=>CH3+H2O                1.0000E+08   1.600  3.1200E+03
OH+CO<=>H+CO2                   4.7600E+07   1.220  7.0000E+01
OH+HCO<=>H2O+CO                 5.0000E+13   0.000  0.0000E+00
OH+CH2O<=>HCO+H2O               3.4300E+09   1.180 -4.4700E+02
OH+CH3O<=>H2O+CH2O              5.0000E+12   0.000  0.0000E+00
OH+CH3OH<=>CH3O+H2O             6.3000E+06   2.000  1.5000E+03
OH+C2H2<=>H+CH2CO               2.1800E-04   4.500 -1.0000E+03
```

```
OH+C2H2<=>CH3+CO                 4.8300E-04   4.000 -2.0000E+03
OH+C2H6<=>C2H5+H2O               3.5400E+06   2.120  8.7000E+02
HO2+CH3<=>O2+CH4                 1.0000E+12   0.000  0.0000E+00
HO2+CH3<=>OH+CH3O                3.7800E+13   0.000  0.0000E+00
HO2+CO<=>OH+CO2                  1.5000E+14   0.000  2.3600E+04
CH+O2<=>O+HCO                    6.7100E+13   0.000  0.0000E+00
CH+H2O<=>H+CH2O                  5.7100E+12   0.000 -7.5500E+02
CH+CH4<=>H+C2H4                  6.0000E+13   0.000  0.0000E+00
CH+CO2<=>HCO+CO                  1.9000E+14   0.000  1.5792E+04
CH+CH2O<=>H+CH2CO                9.4600E+13   0.000 -5.1500E+02
CH3+O2<=>O+CH3O                  3.5600E+13   0.000  3.0480E+04
CH3+O2<=>OH+CH2O                 2.3100E+12   0.000  2.0315E+04
2CH3(+M)<=>C2H6(+M)              6.7700E+16  -1.180  6.5400E+02
 LOW/  3.4000E+41  -7.030  2.7620E+03 /
 TROE/ 0.6190      73.20      1180.      9999.     /
 C2H6/ 3.00/ CO2/ 2.00/ H2/ 2.00/ CO/ 1.50/ H2O/ 6.00/ CH4/ 2.00/
2CH3<=>H+C2H5                    6.8400E+12   0.100  1.0600E+04
CH3+HCO<=>CH4+CO                 2.6480E+13   0.000  0.0000E+00
CH3+CH2O<=>HCO+CH4               3.3200E+03   2.810  5.8600E+03
CH3+CH3OH<=>CH3O+CH4             1.0000E+07   1.500  9.9400E+03
CH3+C2H6<=>C2H5+CH4              6.1400E+06   1.740  1.0450E+04
HCO+H2O<=>H+CO+H2O               1.5000E+18  -1.000  1.7000E+04
HCO+M<=>H+CO+M                   1.8700E+17  -1.000  1.7000E+04
 C2H6/ 3.00/ CO2/ 2.00/ H2/ 2.00/ CO/ 1.50/ H2O/ 0.00/ CH4/ 2.00/
HCO+O2<=>HO2+CO                  1.3450E+13   0.000  4.0000E+02
CH3O+O2<=>HO2+CH2O               4.2800E-13   7.600 -3.5300E+03
C2H4(+M)<=>H2+C2H2(+M)           8.0000E+12   0.440  8.6770E+04
 LOW/  1.5800E+51  -9.300  9.7800E+04 /
 TROE/ 0.7345      180.0      1035.      5417.     /
 C2H6/ 3.00/ CO2/ 2.00/ H2/ 2.00/ CO/ 1.50/ H2O/ 6.00/ CH4/ 2.00/
C2H5+O2<=>HO2+C2H4               8.4000E+11   0.000  3.8750E+03
O+CH3=>H+H2+CO                   3.3700E+13   0.000  0.0000E+00
OH+HO2<=>O2+H2O                  5.0000E+15   0.000  1.7330E+04
DUPLICATE
OH+CH3=>H2+CH2O                  8.0000E+09   0.500 -1.7550E+03
CH+H2(+M)<=>CH3(+M)              1.9700E+12   0.430 -3.7000E+02
 LOW/  4.8200E+25  -2.800  5.9000E+02 /
 TROE/ 0.5780      122.0      2535.      9365.     /
 C2H6/ 3.00/ CO2/ 2.00/ H2/ 2.00/ CO/ 1.50/ H2O/ 6.00/ CH4/ 2.00/
C2H6+O2(a1)=>C2H5+HO2            5.4700E-01   3.660  1.0194E+04
C2H6+O2(a1)=>C2H6+O2             2.2000E-01   3.110  3.9147E+03
H2+O2(a1)<=>H+HO2                1.1000E+08   1.880  3.3915E+04
```

```
H2+O2(b1)<=>H+HO2                 2.1000E+13   0.000  4.0739E+04
H+O2(a1)<=>OH+O                   1.1640E+07   1.615  1.3174E+03
DUPLICATE
H+O2(a1)<=>OH+O                   6.9380E+10   0.962  5.0454E+03
DUPLICATE
H+O2(b1)<=>OH+O(1D)               2.6400E+14  -0.030  3.2213E+04
H+O2(a1)(+M)<=>HO2(+M)            1.1640E+07   1.615  1.3175E+03
 LOW/  9.8900E+09   2.030  3.3604E+03 /
H2O+O2(a1)<=>OH+HO2               2.0500E+15   0.000  4.9661E+04
H2O+O2(b1)<=>OH+HO2               2.0500E+15   0.000  5.4410E+04
CH4+O2(a1)<=>CH3+HO2              7.0600E+07   1.970  3.3523E+04
CH4+O2(b1)<=>CH3+HO2              2.2200E+14   0.000  3.9685E+04
O2(a1)+M=>2O+M                    5.4000E+18  -1.000  9.5402E+04
O2(b1)+M=>2O+M                    5.4000E+18  -1.000  8.0313E+04
OH+O2(a1)=>O+HO2                  1.3000E+13   0.000  3.4045E+04
OH+O2(b1)=>O+HO2                  1.3000E+13   0.000  2.0093E+04
CO+O2(a1)=>CO2+O                  6.7690E+07   1.600  2.7145E+04
CO+O2(b1)=>CO2+O                  6.7690E+07   1.600  5.7172E+04
CO+HO2=>HCO+O2(a1)                8.9100E+12   0.000  5.4976E+04
CO+HO2=>HCO+O2(b1)                8.9100E+12   0.000  7.0065E+04
CH2O+O2(a1)=>HO2+HCO              3.6300E+15   0.000  2.5834E+04
CH2O+O2(b1)=>HO2+HCO              3.6300E+15   0.000  1.4765E+04
CH3+O2(a1)=>CH2O+OH               6.6200E+11   0.000  1.0876E+04
CH3+O2(b1)=>CH2O+OH               6.6200E+11   0.000  9.3757E+03
CH3+O2(a1)=>CH3O+O                2.1100E+13   0.000  1.4374E+04
CH3+O2(b1)=>CH3O+O                2.1100E+13   0.000  7.2612E+03
CH+O2(a1)=>CO+OH                  1.4000E+11   0.670  2.3226E+04
CH+O2(b1)=>CO+OH                  1.4000E+11   0.670  2.1784E+04
HCO+O<=>CH+O2(a1)                 1.4000E+13   0.000  9.7105E+04
HCO+O<=>CH+O2(b1)                 1.4000E+13   0.000  1.1219E+05
CH3O+O2(a1)=>CH2O+HO2             6.6200E+10   0.000  1.5002E+03
CH3O+O2(b1)=>CH2O+HO2             6.6200E+10   0.000  1.1625E+03
C2H5+O2(a1)=>C2H4+HO2             8.4300E+11   0.000  1.7130E+03
C2H5+O2(b1)=>C2H4+HO2             8.4300E+11   0.000  1.2261E+03
C2H6+O2(b1)=>C2H5+HO2             4.0300E+13   0.000  1.3147E+04
C2H2+O2(a1)=>2HCO                 4.0000E+12   0.000  2.3101E+04
C2H2+O2(b1)=>2HCO                 4.0000E+12   0.000  2.0144E+04
N2(B3)+CH4<=>N2+CH3+H             1.8000E+14   0.000  0.0000E+00
N2(C3)+CH4<=>N2+CH3+H             4.0000E+14   0.000  0.0000E+00
N2(ap)+CH4<=>N2+CH3+H             1.8000E+14   0.000  0.0000E+00
N2(C3)=>N2(B3)                    2.4500E+07   0.000  0.0000E+00
N2(ap)=>N2                        1.0000E+02   0.000  0.0000E+00
```

```
O2(a1)=>O2                          2.6000E-04   0.000  0.0000E+00
O2(b1)=>O2(a1)                      1.5000E-03   0.000  0.0000E+00
O2(b1)=>O2                          8.5000E-02   0.000  0.0000E+00
O2(A3)=>O2                          5.0000E+04   0.000  0.0000E+00
O(1D)=>O                            9.0900E-03   0.000  0.0000E+00
2O2(a1)<=>O2(b1)+O2                 4.2000E-04   3.800 -1.3910E+03
O2(a1)+M=>O2+M                      1.0000E+06   0.000  0.0000E+00
 O/160.00/ HO2/11100.00/ H/160.00/ CO/ 2.00/ H2O/ 1.24/ O2/ 0.37/ N2/ 0.00/
O2(b1)+M=>O2(a1)+M                  4.9200E+11   0.000  0.0000E+00
 O/ 0.10/ OH/ 8.17/ H/ 0.10/ CO2/ 0.41/ H2O/ 0.00/ O2/ 0.00/ N2/ 0.00/
O2(b1)+H2O=>O2(a1)+H2O              2.7000E+12   0.000 -1.7686E+02
O2(b1)+N2=>O2(a1)+N2                1.2000E+09   0.000 -7.3614E+01
O2(b1)+M=>O2+M                      4.9200E+11   0.000  0.0000E+00
 N/ 0.10/
N2(B3)+N2=>2N2                      6.0200E+11   0.000  0.0000E+00
N2(B3)+O2=>N2+2O                    1.8100E+14   0.000  0.0000E+00
N2(C3)+N2=>N2(ap)+N2                1.5100E+13   0.000  0.0000E+00
N2(C3)+O2=>N2+O+O(1D)               6.0200E+13   0.000  0.0000E+00
N2(ap)+N2=>N2(B3)+N2                1.1400E+11   0.000  0.0000E+00
N2(ap)+O2=>N2+2O                    1.6900E+13   0.000  0.0000E+00
N2(ap)+H=>N2+H                      9.0300E+13   0.000  0.0000E+00
N2(ap)+H2=>N2+2H                    1.5700E+13   0.000  0.0000E+00
O2(b1)+O=>O2+O(1D)                  3.6100E+13  -0.100  8.3458E+03
O2(A3)+O=>O2+O                      5.4200E+12   0.000  0.0000E+00
O2(A3)+O2=>2O2                      1.8100E+11   0.000  0.0000E+00
O2(A3)+N2=>O2+N2                    5.4200E+09   0.000  0.0000E+00
2O+CO2=>O2(a1)+CO2                  9.0700E+12   0.000 -1.7885E+03
2O+CO2=>O2(b1)+CO2                  1.3100E+12   0.000 -1.7885E+03
O(1D)+O=>2O                         4.8200E+12   0.000  0.0000E+00
O(1D)+O2=>O+O2                      3.8500E+12   0.000 -1.3313E+02
O(1D)+O2=>O+O2(a1)                  6.0200E+11   0.000  0.0000E+00
O(1D)+O2=>O+O2(b1)                  1.5700E+13   0.000 -1.3313E+02
O(1D)+N2=>O+N2                      1.3900E+13   0.000  0.0000E+00
N2(ap)+O2<=>N2(B3)+O2               1.6900E+13   0.000  0.0000E+00
N2(C3)+N2<=>N2(B3)+N2               6.0200E+12   0.000  0.0000E+00
N2(C3)+O2<=>N2(B3)+O2(A3)           1.8100E+14   0.000  0.0000E+00
N2(vib1)+C2H4<=>N2+C2H4             6.0200E+09   0.000  0.0000E+00
O2(b1)+N<=>O2(a1)+N                 6.0200E+10   0.000  0.0000E+00
O2(A3)+O2<=>2O2(b1)                 1.7500E+11   0.000  0.0000E+00
O2(A3)+N2<=>O2(b1)+N2               1.8100E+11   0.000  0.0000E+00
O2(A3)+O<=>O2(b1)+O(1D)             5.4200E+12   0.000  0.0000E+00
2N+M<=>N2+M                         1.6000E+15   0.000  0.0000E+00
```

```
2N+M=>N2(B3)+M                  8.7000E+14   0.000  0.0000E+00
HCO+O2(a1)=>HO2+CO              1.3450E+13   0.000  2.4092E+02
HCO+O2(b1)=>HO2+CO              1.3450E+13   0.000  2.6482E+02
O2(A3)+CO=>O+CO2                2.5000E+12   0.000  2.0722E+04
CH3+O2(A3)=>OH+CH2O             2.3100E+12   0.000  9.0894E+03
HCO+O2(A3)=>HO2+CO              1.3450E+13   0.000  1.0134E+02
C2H5+O2(A3)=>HO2+C2H4           8.4000E+11   0.000  5.6979E+02
O(1D)+CO(+M)=>CO2(+M)           1.8000E+10   0.000  1.7727E+03
 LOW/  6.0200E+14   0.000  2.2345E+03 /
O(1D)+CH2O=>OH+HCO              3.9000E+13   0.000  1.0347E+03
O(1D)+C2H4=>CH3+HCO             1.2500E+07   1.830  8.2457E+01
O(1D)+C2H6=>OH+C2H5             8.9800E+07   1.920  8.8193E+02
O(1D)+CH3O=>CH3+O2              6.3440E+16  -0.770  1.6061E+03
O2(vib2)+M=>2O+M                1.1280E+20  -1.440  1.1078E+05
OH+O2(vib2)=>O+HO2              7.2230E+11   0.450  4.3236E+04
O2(vib2)+CO=>O+CO2              2.5000E+12   0.000  4.3642E+04
O2(vib2)+CH2O=>HO2+HCO          1.0000E+14   0.000  3.1190E+04
HO2+O2(vib2)=>H+2O2             1.4220E+21  -1.720  4.1252E+04
H+O2(vib2)=>O+OH                2.6500E+16  -0.670  8.1023E+03
O2(vib2)+H2=>H+HO2              2.1560E+12   0.510  4.6295E+04
O2(vib2)+H2O=>OH+HO2            6.5920E+13   0.140  6.0803E+04
DUPLICATE
O2(vib2)+CH4=>HO2+CH3           1.2220E+17  -0.890  4.9952E+04
CH3+O2(vib2)=>O+CH3O            3.5600E+13   0.000  2.2036E+04
CH3+O2(vib2)=>OH+CH2O           2.3100E+12   0.000  1.8325E+04
HCO+O2(vib2)=>HO2+CO            1.3450E+13   0.000  2.9446E+02
C2H5+O2(vib2)=>HO2+C2H4         8.4000E+11   0.000  2.1721E+03
O2(vib2)+H2O=>OH+HO2            2.2730E+16   0.140  8.0163E+04
DUPLICATE
O2(vib3)+M=>2O+M                1.1280E+20  -1.440  1.0629E+05
OH+O2(vib3)=>O+HO2              7.2230E+11   0.450  3.8671E+04
O2(vib3)+CO=>O+CO2              2.5000E+12   0.000  4.1539E+04
O2(vib3)+CH2O=>HO2+HCO          1.0000E+14   0.000  2.6769E+04
HO2+O2(vib3)=>H+2O2             1.4220E+21  -1.720  3.6807E+04
H+O2(vib3)=>O+OH                2.6500E+16  -0.670  3.6305E+03
O2(vib3)+H2=>H+HO2              2.1560E+12   0.510  4.1778E+04
O2(vib3)+H2O=>OH+HO2            6.5920E+13   0.140  5.6262E+04
DUPLICATE
O2(vib3)+CH4=>HO2+CH3           1.2220E+17  -0.890  4.5626E+04
CH3+O2(vib3)=>O+CH3O            3.5600E+13   0.000  1.7811E+04
CH3+O2(vib3)=>OH+CH2O           2.3100E+12   0.000  1.7330E+04
HCO+O2(vib3)=>HO2+CO            1.3450E+13   0.000  2.4163E+02
```

```
C2H5+O2(vib3)=>HO2+C2H4          8.4000E+11   0.000  1.3203E+03
O2(vib3)+H2O=>OH+HO2             2.2730E+16   0.140  7.6410E+04
DUPLICATE
O2(vib4)+M=>2O+M                 1.1280E+20  -1.440  1.0179E+05
OH+O2(vib4)=>O+HO2               7.2230E+11   0.450  3.4082E+04
O2(vib4)+CO=>O+CO2               2.5000E+12   0.000  3.9460E+04
O2(vib4)+CH2O=>HO2+HCO           1.0000E+14   0.000  2.2371E+04
HO2+O2(vib4)=>H+2O2              1.4220E+21  -1.720  3.2385E+04
H+O2(vib4)=>O+OH                 2.6500E+16  -0.670  0.0000E+00
O2(vib4)+H2=>H+HO2               2.1560E+12   0.510  3.7285E+04
O2(vib4)+H2O=>OH+HO2             6.5920E+13   0.140  5.1721E+04
DUPLICATE
O2(vib4)+CH4=>HO2+CH3            1.2220E+17  -0.890  4.1324E+04
CH3+O2(vib4)=>O+CH3O             3.5600E+13   0.000  1.3592E+04
CH3+O2(vib4)=>OH+CH2O            2.3100E+12   0.000  1.6336E+04
HCO+O2(vib4)=>HO2+CO             1.3450E+13   0.000  1.8905E+02
C2H5+O2(vib4)=>HO2+C2H4          8.4000E+11   0.000  4.6941E+02
O2(vib4)+H2O=>OH+HO2             2.2730E+16   0.140  7.2634E+04
DUPLICATE
HO2+N2(vib1)=>H+O2+N2            1.7770E+21  -1.720  4.3571E+04
HO2+N2(vib4)=>H+O2+N2            1.7770E+21  -1.720  2.3972E+04
HO2+N2(vib5)=>H+O2+N2            1.7770E+21  -1.720  1.7428E+04
H+O2(a1)+O2=>HO2+O2              2.0800E+19  -1.240  0.0000E+00
HO2+O2(a1)=>H+2O2                1.4220E+21  -1.720  5.0096E+04
H+O2(a1)+H2O=>HO2+H2O            1.1260E+19  -0.760  0.0000E+00
H+O2(a1)+N2=>HO2+N2              2.6000E+19  -1.240  0.0000E+00
H+O2(b1)+M=>HO2+M                2.8000E+18  -0.860  0.0000E+00
H+O2(b1)+O2=>HO2+O2              2.0800E+19  -1.240  0.0000E+00
HO2+O2(b1)=>H+2O2                1.4220E+21  -1.720  5.0096E+04
H+O2(b1)+H2O=>HO2+H2O            1.1260E+19  -0.760  0.0000E+00
H+O2(b1)+N2=>HO2+N2              2.6000E+19  -1.240  0.0000E+00
H+O2(b1)=>O+OH                   2.6500E+16  -0.670  1.7041E+04
O2(A3)+M=>2O+M                   1.1280E+20  -1.440  1.1977E+05
OH+O2(A3)=>O+HO2                 7.2230E+11   0.450  5.2414E+04
O2(A3)+CH2O=>HO2+HCO             1.0000E+14   0.000  4.0010E+04
H+O2(A3)+M=>HO2+M                2.8000E+18  -0.860  0.0000E+00
H+O2(A3)+O2=>HO2+O2              2.0800E+19  -1.240  0.0000E+00
HO2+O2(A3)=>H+2O2                1.4220E+21  -1.720  5.0096E+04
H+O2(A3)+H2O=>HO2+H2O            1.1260E+19  -0.760  0.0000E+00
H+O2(A3)+N2=>HO2+N2              2.6000E+19  -1.240  0.0000E+00
H+O2(A3)=>O+OH                   2.6500E+16  -0.670  1.7041E+04
O2(A3)+H2=>H+HO2                 2.1560E+12   0.510  5.5306E+04
```

```
O2(A3)+H2O=>OH+HO2                6.5920E+13   0.140  6.9861E+04
DUPLICATE
O2(A3)+CH4=>HO2+CH3               1.2220E+17  -0.890  5.8604E+04
CH+O2(A3)=>O+HCO                  6.7100E+13   0.000  0.0000E+00
CH3+O2(A3)=>O+CH3O                3.5600E+13   0.000  3.0473E+04
CH3O+O2(A3)=>HO2+CH2O             4.2800E-13   7.600 -3.5301E+03
O2(A3)+H2O=>OH+HO2                2.2730E+16   0.140  8.7691E+04
DUPLICATE
2O(1D)+M=>O2+M                    1.2000E+17  -1.000  0.0000E+00
O(1D)+H+M=>OH+M                   5.0000E+17  -1.000  0.0000E+00
O(1D)+H2=>H+OH                    3.8700E+04   2.700  6.2596E+03
O(1D)+HO2=>OH+O2                  2.0000E+13   0.000  0.0000E+00
O(1D)+CH=>H+CO                    5.7000E+13   0.000  0.0000E+00
O(1D)+CH3=>H+CH2O                 5.0600E+13   0.000  0.0000E+00
O(1D)+CH4=>OH+CH3                 1.0200E+09   1.500  8.5994E+03
O(1D)+HCO=>OH+CO                  3.0000E+13   0.000  0.0000E+00
O(1D)+HCO=>H+CO2                  3.0000E+13   0.000  0.0000E+00
O(1D)+CH3O=>OH+CH2O               1.0000E+13   0.000  0.0000E+00
O(1D)+CH3OH=>OH+CH3O              1.3000E+05   2.500  5.0000E+03
O(1D)+C2H5=>CH3+CH2O              2.2400E+13   0.000  0.0000E+00
O(1D)+CO2=>O2+CO                  3.6680E+16  -0.880  5.6692E+04
O(1D)+OH=>H+O2                    6.9600E+13  -0.270 -2.1549E+02
O(1D)+H2O=>H+HO2                  4.7400E+10   0.550  5.3776E+04
O(1D)+H2O=>2OH                    4.4930E+06   2.100  1.5851E+04
O(1D)+HCO=>CH+O2                  1.3840E+14  -0.050  7.3136E+04
O(1D)+CH3=>H+H2+CO                3.3700E+13   0.000  0.0000E+00
H+O2+N2(B3)=>HO2+N2               2.6000E+19  -1.240  0.0000E+00
HO2+N2(B3)=>H+O2+N2               1.7770E+21  -1.720  5.0096E+04
H+O2+N2(ap)=>HO2+N2               2.6000E+19  -1.240  0.0000E+00
HO2+N2(ap)=>H+O2+N2               1.7770E+21  -1.720  5.0096E+04
H+O2+N2(C3)=>HO2+N2               2.6000E+19  -1.240  0.0000E+00
HO2+N2(C3)=>H+O2+N2               1.7770E+21  -1.720  5.0096E+04
H+O2(vib2)+M=>HO2+M               2.8000E+18  -0.860  0.0000E+00
H+O2(vib2)+O2=>HO2+O2             2.0800E+19  -1.240  0.0000E+00
H+O2(vib2)+H2O=>HO2+H2O           1.1260E+19  -0.760  0.0000E+00
H+O2(vib2)+N2=>HO2+N2             2.6000E+19  -1.240  0.0000E+00
CH+O2(vib2)=>O+HCO                6.7100E+13   0.000  0.0000E+00
CH3O+O2(vib2)=>HO2+CH2O           4.2800E-13   7.600 -3.5301E+03
H+O2(vib3)+M=>HO2+M               2.8000E+18  -0.860  0.0000E+00
H+O2(vib3)+O2=>HO2+O2             2.0800E+19  -1.240  0.0000E+00
H+O2(vib3)+H2O=>HO2+H2O           1.1260E+19  -0.760  0.0000E+00
H+O2(vib3)+N2=>HO2+N2             2.6000E+19  -1.240  0.0000E+00
```

```
CH+O2(vib3)=>O+HCO              6.7100E+13   0.000  0.0000E+00
CH3O+O2(vib3)=>HO2+CH2O         4.2800E-13   7.600 -3.5301E+03
H+O2(vib4)+M=>HO2+M             2.8000E+18  -0.860  0.0000E+00
H+O2(vib4)+O2=>HO2+O2           2.0800E+19  -1.240  0.0000E+00
H+O2(vib4)+H2O=>HO2+H2O         1.1260E+19  -0.760  0.0000E+00
H+O2(vib4)+N2=>HO2+N2           2.6000E+19  -1.240  0.0000E+00
CH+O2(vib4)=>O+HCO              6.7100E+13   0.000  0.0000E+00
CH3O+O2(vib4)=>HO2+CH2O         4.2800E-13   7.600 -3.5301E+03
H+O2+N2(vib1)=>HO2+N2           2.6000E+19  -1.240  0.0000E+00
H+O2+N2(vib4)=>HO2+N2           2.6000E+19  -1.240  0.0000E+00
H+O2+N2(vib5)=>HO2+N2           2.6000E+19  -1.240  0.0000E+00
O2(vib3)+H2=>O2(vib2)+H2        3.2000E+16   0.000  0.0000E+00
O2(vib3)+O2=>O2(vib2)+O2        3.3000E+18   0.000  0.0000E+00
O2(vib3)+N2=>O2(vib2)+N2        2.9000E+18   0.000  0.0000E+00
O2(vib3)+CO=>O2(vib2)+CO        2.9000E+18   0.000  0.0000E+00
O2(vib3)+H2O=>O2(vib2)+H2O      1.6000E+18   0.000  0.0000E+00
O2(vib3)+CO2=>O2(vib2)+CO2      4.6000E+18   0.000  0.0000E+00
O2(vib3)+CH4=>O2(vib2)+CH4      1.6000E+18   0.000  0.0000E+00
O2(vib4)+H2=>O2(vib3)+H2        4.6000E+16   0.000  0.0000E+00
O2(vib4)+O2=>O2(vib3)+O2        5.3000E+18   0.000  0.0000E+00
O2(vib4)+N2=>O2(vib3)+N2        4.5000E+18   0.000  0.0000E+00
O2(vib4)+CO=>O2(vib3)+CO        4.5000E+18   0.000  0.0000E+00
O2(vib4)+H2O=>O2(vib3)+H2O      2.5000E+18   0.000  0.0000E+00
O2(vib4)+CO2=>O2(vib3)+CO2      7.5000E+18   0.000  0.0000E+00
O2(vib4)+CH4=>O2(vib3)+CH4      2.5000E+18   0.000  0.0000E+00
N2(vib1)+H2=>N2+H2              2.7000E+15   0.000  0.0000E+00
N2(vib1)+O2=>N2+O2              2.0000E+12   0.000  0.0000E+00
N2(vib1)+N2=>2N2                1.7000E+12   0.000  0.0000E+00
N2(vib1)+CO=>N2+CO              1.7000E+15   0.000  0.0000E+00
N2(vib1)+H2O=>N2+H2O            1.0000E+15   0.000  0.0000E+00
N2(vib1)+CO2=>N2+CO2            2.6000E+15   0.000  0.0000E+00
N2(vib1)+CH4=>N2+CH4            1.0000E+15   0.000  0.0000E+00
N2(vib5)+H2=>N2(vib4)+H2        1.8000E+17   0.000  0.0000E+00
N2(vib5)+O2=>N2(vib4)+O2        2.2000E+18   0.000  0.0000E+00
N2(vib5)+N2=>N2(vib4)+N2        1.9000E+18   0.000  0.0000E+00
N2(vib5)+CO=>N2(vib4)+CO        1.9000E+18   0.000  0.0000E+00
N2(vib5)+H2O=>N2(vib4)+H2O      1.0000E+18   0.000  0.0000E+00
N2(vib5)+CO2=>N2(vib4)+CO2      3.1000E+18   0.000  0.0000E+00
N2(vib5)+CH4=>N2(vib4)+CH4      1.0000E+18   0.000  0.0000E+00
N2(vib1)+O=>N2+O                1.3900E+11   0.000  2.5435E+03
DUPLICATE
N2(vib1)+O=>N2+O                1.6300E+13   0.000  2.1540E+04
```

```
DUPLICATE
N2(vib1)+O2(vib2)=>N2+O2(vib3)  7.4070E+09   1.000  0.0000E+00
N2(vib1)+O2(vib3)=>N2+O2(vib4)  7.4070E+09   1.000  0.0000E+00
O2+E+O<=>O2^-+O                 3.6300E+16   0.000  0.0000E+00
O2+E+H2O<=>O2^-+H2O             5.0800E+18   0.000  0.0000E+00
O2+E+N2=>O2^-+N2                3.5900E+21  -2.000  1.3862E+02
2O2+E=>O2^-+O2                  1.5200E+21  -1.000  1.1926E+03
E+O+O2<=>O^-+O2                 3.6300E+16   0.000  0.0000E+00
E+2O<=>O^-+O                    3.0200E+17   0.000  0.0000E+00
O2^-+N2=>O2+E+N2                6.6100E+10   0.500  9.9163E+03
O2^-+O2=>2O2+E                  9.3900E+12   0.500  1.1107E+04
O2^-+N2(B3)=>O2+N2+E            1.5060E+15   0.000  0.0000E+00
O2^-+O2(a1)=>2O2+E              1.2040E+14   0.000  0.0000E+00
O2^-+O2(b1)=>2O2+E              2.1680E+15   0.000  0.0000E+00
O2^-+O2(vib4)=>2O2+E            1.2000E+14   0.000  0.0000E+00
O2^-+N2(vib4)=>O2+N2+E          1.2650E+15   0.000  0.0000E+00
O2^-+N2(vib5)=>O2+N2+E          1.2650E+15   0.000  0.0000E+00
O^-+N2(vib1)=>O+N2+E            7.6500E+13   0.500  2.7032E+04
O^-+N2(vib4)=>O+N2+E            7.6500E+13   0.500  7.0507E+03
O^-+N2(vib5)=>O+N2+E            7.6500E+13   0.500  3.7524E+02
O^-+O2(vib2)=>O+O2+E            2.4000E+13   0.500  2.4665E+04
O^-+O2(vib3)=>O+O2+E            2.4000E+13   0.500  2.0148E+04
O^-+O2(vib4)=>O+O2+E            2.4000E+13   0.500  1.5631E+04
O^-+O2(b1)=>O+O2+E              4.1550E+14   0.000  0.0000E+00
O^-+N2(B3)=>O+N2+E              1.1440E+15   0.000  0.0000E+00
O^-+O2(A3)=>O+O2+E              4.1550E+14   0.000  0.0000E+00
O^-+N2(C3)=>O+N2+E              1.1440E+15   0.000  0.0000E+00
O^-+N2(ap)=>O+N2+E              1.1440E+15   0.000  0.0000E+00
H^-+CH3=>CH4+E                  6.0221E+14   0.000  0.0000E+00
H^-+HCO=>CH2O+E                 6.0221E+14   0.000  0.0000E+00
H^-+CO=>HCO+E                   1.2044E+13   0.000  0.0000E+00
H^-+H=>H2+E                     2.5473E+16  -0.400  7.8296E+01
H^-+O=>OH+E                     6.0221E+14   0.000  0.0000E+00
H^-+OH=>H2O+E                   6.0221E+13   0.000  0.0000E+00
H^-+O2=>HO2+E                   7.8290E+14   0.000  0.0000E+00
H^-+CH2O=>CH3O+E                6.0221E+14   0.000  0.0000E+00
H^-+C2H4=>C2H5+E                6.0221E+14   0.000  0.0000E+00
O2^-+H=>HO2+E                   7.2300E+14   0.000  0.0000E+00
O^-+H=>OH+E                     3.0100E+14   0.000  0.0000E+00
O^-+H2=>H2O+E                   4.2200E+14   0.000  0.0000E+00
O^-+CH=>HCO+E                   3.0100E+14   0.000  0.0000E+00
O^-+CO=>CO2+E                   3.9100E+14   0.000  0.0000E+00
```

```
O^-+O=>O2+E                       1.3900E+14   0.000  0.0000E+00
O^-+C2H2=>CH2CO+E                 7.2300E+14   0.000  0.0000E+00
O2^-+O<=>O^-+O2                   1.9900E+14   0.000  0.0000E+00
O^-+O2(a1)=>O2^-+O                6.6000E+12   0.000  0.0000E+00
CH4^++O2<=>O2^++CH4               2.3486E+14   0.000  0.0000E+00
N2^++O2<=>O2^++N2                 3.0111E+13   0.000  0.0000E+00
O2^-+O2^+=>2O2                    2.0900E+18  -0.500  0.0000E+00
O^-+O2^+=>O+O2                    2.9600E+17  -0.440  0.0000E+00
O^-+O2^+=>3O                      1.9300E+17  -0.440  0.0000E+00
O2^++E=>2O                        3.7700E+18  -0.610  0.0000E+00
!
! 3 step chemi-ionization mechanism
! Units : A - cm3/(mol-s) or cm6/(mol2-s); Ea - cal/mol
CH + O => HCO+ + E                2.512E+11     0.000       1700.
HCO+ + H2O => H3O+ + CO           1.506E+15     0.000       0.000
H3O+ + E => H2O +H                2.291E+18    -0.500       0.000
H3O+ + E => OH + H + H            7.949E+21    -1.370       0.000
H3O+ + E => H2 + OH               1.253E+19    -0.500       0.000
H3O+ + E => O + H2 + H            6.000E+17    -0.300       0.000
!
TDEP/E/
N2^++E=>2N                        3.0300E+18  -0.570  0.0000E+00
TDEP/E/
CH4^++E=>CH3+H                    3.5900E+18  -0.530  0.0000E+00
TDEP/E/
N2^++2E=>N2+E                     1.0605E+40  -4.500  0.0000E+00
TDEP/E/
O2^++2E=>O2+E                     4.4856E+39  -4.500  0.0000E+00
TDEP/E/
CH4^++2E=>CH4+E                   5.1627E+39  -4.500  0.0000E+00
TDEP/E/
E+CH4=>E+CH4                      6.0221E+23   0.000  0.0000E+00
DUPLICATE
TDEP/E/
/MOME
JAN/ -1.151853E+01 -3.075157E-01  5.033922E-02  5.530594E-02
-6.582943E-02 -1.009087E-02  5.445923E-03  2.653697E-04 -3.242870E-04/
E+CH4=>E+CH4                      0.0000E+00   0.000  0.0000E+00
DUPLICATE
TDEP/E/
EXCI/ 0.15900/
E+CH4=>E+CH4                      0.0000E+00   0.000  0.0000E+00
```

```
DUPLICATE
TDEP/E/
EXCI/ 0.37000/
E+CH4=>E+CH3+H                  6.0221E+23   0.000  0.0000E+00
TDEP/E/
JAN/ -2.463061E+01  4.381080E+00 -1.770511E+00  5.256923E+01
-2.068412E+02  3.305527E+02 -2.604328E+02  1.007294E+02 -1.530068E+01/
E+CH4=>E+CH+H2+H                6.0221E+23   0.000  0.0000E+00
TDEP/E/
JAN/ -2.887296E+01  6.846938E+00 -2.222628E+01  9.990615E+01
-1.923752E+02  1.816222E+02 -8.581213E+01  1.802531E+01 -1.016967E+00/
E+CH4=>2E+CH4^+                 6.0221E+23   0.000  0.0000E+00
TDEP/E/
JAN/ -2.965735E+01  8.029990E+00 -1.611065E+01  9.676885E+01
-2.512924E+02  3.235852E+02 -2.203086E+02  7.620146E+01 -1.056842E+01/
E+CH4=>CH3+H^-                  6.0221E+23   0.000  0.0000E+00
TDEP/E/
JAN/ -2.553777E+01  3.376727E+00 -7.505610E-01  4.872114E+01
-1.993259E+02  3.224795E+02 -2.559604E+02  9.952179E+01 -1.517454E+01/
E+O2=>E+O2                      6.0221E+23   0.000  0.0000E+00
DUPLICATE
TDEP/E/
/MOME
JAN/ -1.667459E+01  1.117100E-02  1.319834E-01  1.622721E-01
-2.492241E-02 -1.993274E-02 -2.309521E-04  5.048132E-04  1.461185E-05/
E+O2=>E+O2                      0.0000E+00   0.000  0.0000E+00
DUPLICATE
TDEP/E/
EXCI/ 0.02000/
E+O2=>E+O2(vib2)                6.0221E+23   0.000  0.0000E+00
DUPLICATE
TDEP/E/
JAN/ -2.308608E+01 -6.027889E-01 -2.917628E-01  1.364253E-01
-1.888023E-01 -1.663281E-02  1.854420E-02  8.564650E-03  5.206541E-04/
E+O2=>E+O2(vib2)                6.0221E+23   0.000  0.0000E+00
DUPLICATE
TDEP/E/
JAN/ -2.388058E+01  2.873884E+00 -8.348839E+00  5.455102E+01
-1.372186E+02  1.679746E+02 -1.085978E+02  3.569004E+01 -4.703233E+00/
E+O2=>E+O2(vib3)                6.0221E+23   0.000  0.0000E+00
TDEP/E/
JAN/ -2.377049E+01  1.191540E+00  6.620202E-01  8.462958E-02
```

```
-4.196426E-01  3.153016E-02  3.705810E-02  1.470296E-03 -1.225641E-03/
E+O2=>E+O2(vib4)                 6.0221E+23   0.000  0.0000E+00
TDEP/E/
JAN/ -2.467041E+01  1.877501E+00  4.103441E-01 -8.639092E-02
-4.206783E-01  1.007090E-01  5.065812E-02 -7.667529E-03 -3.963305E-03/
E+O2=>E+O2(a1)                   6.0221E+23   0.000  0.0000E+00
TDEP/E/
JAN/ -2.289541E+01  2.768605E+00 -8.962704E-01 -5.742305E-01
2.462532E-01  2.601202E-01 -8.397914E-02 -2.489623E-02  2.385195E-03/
E+O2=>E+O2(b1)                   6.0221E+23   0.000  0.0000E+00
TDEP/E/
JAN/ -2.471566E+01  5.214250E+00 -2.339415E+00 -2.446112E+00
5.908785E-01  1.282369E+00 -3.701299E-02 -1.839803E-01 -2.892849E-02/
E+O2=>E+O2(A3)                   6.0221E+23   0.000  0.0000E+00
TDEP/E/
JAN/ -2.393892E+01  2.724655E+00 -5.270904E+00  5.018328E+01
-1.522971E+02  2.125883E+02 -1.531783E+02  5.543491E+01 -7.985311E+00/
E+O2=>E+2O                       6.0221E+23   0.000  0.0000E+00
DUPLICATE
TDEP/E/
JAN/ -2.479545E+01  3.558299E+00 -6.803565E+00  5.419864E+01
-1.568786E+02  2.142641E+02 -1.521755E+02  5.446841E+01 -7.776750E+00/
E+O2=>E+O2                       6.0221E+23   0.000  0.0000E+00
DUPLICATE
TDEP/E/
EXCI/ 6.00000/
JAN/ -2.383134E+01  2.916103E+00 -5.778284E+00  5.156328E+01
-1.550818E+02  2.161769E+02 -1.558684E+02  5.648331E+01 -8.148618E+00/
E+O2=>E+2O                       6.0221E+23   0.000  0.0000E+00
DUPLICATE
TDEP/E/
JAN/ -3.052675E+01  6.903242E+00 -2.125007E+01  9.903285E+01
-1.975395E+02  1.950285E+02 -9.865708E+01  2.356588E+01 -1.919793E+00/
E+O2=>E+O+O(1D)                  6.0221E+23   0.000  0.0000E+00
TDEP/E/
JAN/ -2.948617E+01  6.563016E+00 -7.839867E+00  9.108082E+01
-3.005482E+02  4.428402E+02 -3.317455E+02  1.237881E+02 -1.829600E+01/
E+O2=>E+O2                       6.0221E+23   0.000  0.0000E+00
DUPLICATE
TDEP/E/
EXCI/ 8.40000/
JAN/ -2.346768E+01  3.562112E+00  1.294259E+00  5.023607E+01
```

```
-2.247900E+02  3.746117E+02 -3.019352E+02  1.185428E+02 -1.820027E+01/
E+O2=>E+O2                        6.0221E+23   0.000  0.0000E+00
DUPLICATE
TDEP/E/
EXCI/ 9.97000/
JAN/ -3.094684E+01  4.523992E+00  2.383478E+00  6.070672E+01
-2.768605E+02  4.635757E+02 -3.741273E+02  1.469345E+02 -2.256208E+01/
E+O2=>2E+O2^+                     6.0221E+23   0.000  0.0000E+00
TDEP/E/
JAN/ -2.964395E+01  7.081127E+00 -2.081307E+01  9.932122E+01
-2.036181E+02  2.082951E+02 -1.107956E+02  2.876071E+01 -2.774709E+00/
E+O2=>O+O^-                       6.0221E+23   0.000  0.0000E+00
TDEP/E/
JAN/ -2.615135E+01  2.432776E+00 -3.927317E+00  4.842420E+01
-1.576111E+02  2.282017E+02 -1.686261E+02  6.223272E+01 -9.109840E+00/
E+N2=>E+N2                        6.0221E+23   0.000  0.0000E+00
DUPLICATE
TDEP/E/
/MOME
JAN/ -1.393425E+01  1.119909E+00 -1.741946E+00 -8.732670E-01
7.102912E-01  3.602121E-01 -7.539807E-02 -5.801923E-02 -7.370021E-03/
E+N2=>E+N2                        0.0000E+00   0.000  0.0000E+00
DUPLICATE
TDEP/E/
EXCI/ 0.02000/
E+N2=>E+N2(vib1)                  6.0221E+23   0.000  0.0000E+00
DUPLICATE
TDEP/E/
JAN/ -2.245950E+01  2.611484E-01 -4.136204E-01  1.082233E+00
5.111468E-03 -3.799771E-01 -3.212864E-02  4.923081E-02  9.350533E-03/
E+N2=>E+N2(vib1)                  6.0221E+23   0.000  0.0000E+00
DUPLICATE
TDEP/E/
JAN/ -1.951539E+01  2.984236E+00 -3.305513E+00 -1.396858E+00
1.014712E+00  9.664641E-01 -1.461630E-01 -1.514451E-01 -1.928647E-02/
E+N2=>E+N2(vib4)                  6.0221E+23   0.000  0.0000E+00
TDEP/E/
JAN/ -2.126177E+01  5.974720E+00 -8.379202E+00  2.269163E-01
2.351989E+00  5.170356E-01 -3.113030E-01 -1.311622E-01 -1.294151E-02/
E+N2=>E+N2(vib5)                  6.0221E+23   0.000  0.0000E+00
TDEP/E/
JAN/ -2.119369E+01  4.180744E+00 -1.307323E+01  1.025438E+01
```

```
5.328654E+00 -7.872890E+00  3.650770E-02  1.924704E+00 -4.668873E-01/
E+N2=>E+N2(B3)                   6.0221E+23   0.000  0.0000E+00
DUPLICATE
TDEP/E/
JAN/ -2.493889E+01  3.658233E+00 -4.209001E+00  5.471831E+01
-1.852817E+02  2.756781E+02 -2.076991E+02  7.780112E+01 -1.152858E+01/
E+N2=>E+N2(B3)                   6.0221E+23   0.000  0.0000E+00
DUPLICATE
TDEP/E/
JAN/ -2.571985E+01  3.944154E+00 -1.142545E+00  5.072799E+01
-2.040808E+02  3.284568E+02 -2.597676E+02  1.007125E+02 -1.532239E+01/
E+N2=>E+N2(B3)                   6.0221E+23   0.000  0.0000E+00
DUPLICATE
TDEP/E/
JAN/ -2.703512E+01  4.080603E+00 -7.341150E-01  5.192059E+01
-2.133635E+02  3.461007E+02 -2.749587E+02  1.069248E+02 -1.630258E+01/
E+N2=>E+N2(ap)                   6.0221E+23   0.000  0.0000E+00
DUPLICATE
TDEP/E/
JAN/ -2.733645E+01  4.215809E+00 -9.075529E-01  5.272340E+01
-2.160039E+02  3.503042E+02 -2.783533E+02  1.082726E+02 -1.651190E+01/
E+N2=>E+N2(ap)                   6.0221E+23   0.000  0.0000E+00
DUPLICATE
TDEP/E/
JAN/ -2.654321E+01  3.898119E+00 -2.070136E+00  6.002992E+01
-2.231250E+02  3.442480E+02 -2.646121E+02  1.004602E+02 -1.503950E+01/
E+N2=>E+N2(ap)                   6.0221E+23   0.000  0.0000E+00
DUPLICATE
TDEP/E/
JAN/ -2.716782E+01  4.067065E+00  2.501274E+00  5.212547E+01
-2.464734E+02  4.183088E+02 -3.404031E+02  1.344537E+02 -2.073012E+01/
E+N2=>E+N2(C3)                   6.0221E+23   0.000  0.0000E+00
DUPLICATE
TDEP/E/
JAN/ -2.709411E+01  5.309536E+00  2.939946E+00  6.754236E+01
-3.144770E+02  5.307346E+02 -4.304446E+02  1.696100E+02 -2.610188E+01/
E+N2=>E+N2(C3)                   6.0221E+23   0.000  0.0000E+00
DUPLICATE
TDEP/E/
JAN/ -3.017012E+01  4.246506E+00  2.463670E+00  6.870243E+01
-3.088521E+02  5.139158E+02 -4.135203E+02  1.621389E+02 -2.486909E+01/
E+N2=>E+N2(C3)                   6.0221E+23   0.000  0.0000E+00
```

```
DUPLICATE
TDEP/E/
JAN/ -3.160245E+01  6.125984E+00 -1.561379E+00  7.963809E+01
-3.194428E+02  5.130769E+02 -4.051261E+02  1.568429E+02 -2.383100E+01/
E+N2=>E+2N                      6.0221E+23   0.000  0.0000E+00
TDEP/E/
JAN/ -2.926806E+01  5.245170E+00  2.680346E+00  6.106892E+01
-2.803532E+02  4.707759E+02 -3.803593E+02  1.493993E+02 -2.293330E+01/
E+N2=>2E+N2^+                   6.0221E+23   0.000  0.0000E+00
TDEP/E/
JAN/ -3.353871E+01  1.411246E+01 -2.161509E+01  4.660642E+01
-6.999784E+01  6.646214E+01 -3.684074E+01  1.076302E+01 -1.278393E+00/
E+H2O=>E+H2O                    6.0221E+23   0.000  0.0000E+00
DUPLICATE
TDEP/E/
/MOME
JAN/ -1.031872E+01 -1.196794E+00  8.778519E-02 -5.532978E-02
-3.183902E-02  3.006118E-02  1.112279E-02 -3.200382E-03 -1.140245E-03/
E+H2O=>E+H2O                    0.0000E+00   0.000  0.0000E+00
DUPLICATE
TDEP/E/
EXCI/ 0.00460/
E+H2O=>E+H2O                    0.0000E+00   0.000  0.0000E+00
DUPLICATE
TDEP/E/
EXCI/ 0.00869/
E+H2O=>E+H2O                    0.0000E+00   0.000  0.0000E+00
DUPLICATE
TDEP/E/
EXCI/ 0.01764/
E+H2O=>E+H2O                    6.0221E+23   0.000  0.0000E+00
DUPLICATE
TDEP/E/
EXCI/ 0.19800/
JAN/ -1.981915E+01 -1.647396E-01  1.492472E-01  1.266275E-02
-6.736158E-02  2.297664E-02  1.036932E-02 -2.331925E-03 -1.188291E-03/
E+H2O=>E+H2O                    6.0221E+23   0.000  0.0000E+00
DUPLICATE
TDEP/E/
EXCI/ 0.45300/
JAN/ -1.945667E+01  1.505287E-01  1.356059E-01  9.139809E-02
-1.075219E-01  8.490705E-03  4.470243E-03  3.169937E-04 -5.995762E-04/
```

```
E+H2O=>E+H2+O                     6.0221E+23   0.000  0.0000E+00
TDEP/E/
JAN/ -3.539648E+01  1.076523E+01 -1.578696E+01  3.284163E+01
-4.844921E+01  4.566953E+01 -2.516748E+01  7.301072E+00 -8.599436E-01/
E+H2O=>E+OH+H                     6.0221E+23   0.000  0.0000E+00
TDEP/E/
JAN/ -2.469923E+01  3.808537E+00 -5.924001E+00  5.576575E+01
-1.716413E+02  2.430208E+02 -1.770003E+02  6.463613E+01 -9.388051E+00/
E+H2O=>H^-+OH                     6.0221E+23   0.000  0.0000E+00
TDEP/E/
JAN/ -2.519366E+01  2.568925E+00 -5.121749E+00  4.821152E+01
-1.474800E+02  2.074066E+02 -1.505014E+02  5.482395E+01 -7.944376E+00/
E+H2O=>O^-+H2                     6.0221E+23   0.000  0.0000E+00
TDEP/E/
JAN/ -3.022813E+01  3.226368E+00 -3.028880E+00  4.442604E+01
-1.589677E+02  2.439835E+02 -1.878785E+02  7.155847E+01 -1.074445E+01/
E+CO2=>E+CO2                      6.0221E+23   0.000  0.0000E+00
DUPLICATE
TDEP/E/
/MOME
JAN/ -1.687849E+01  3.185338E-01  2.598628E-01  3.106570E-02
-5.219965E-02 -1.472093E-02  4.578672E-03  2.299034E-03  2.460206E-04/
E+CO2=>E+CO2                      6.0221E+23   0.000  0.0000E+00
DUPLICATE
TDEP/E/
EXCI/ 0.08300/
JAN/ -1.910525E+01  3.513636E-01  3.744406E-01 -2.044136E-01
-1.729153E-01  5.274595E-02  2.957714E-02 -5.550645E-03 -2.431504E-03/
E+CO2=>E+CO2                      6.0221E+23   0.000  0.0000E+00
DUPLICATE
TDEP/E/
EXCI/ 0.16700/
JAN/ -1.943108E+01  6.482484E-01  4.305566E-02 -1.869126E-01
-5.661915E-02  4.570648E-02  8.780517E-03 -4.962376E-03 -1.430933E-03/
E+CO2=>E+CO2                      6.0221E+23   0.000  0.0000E+00
DUPLICATE
TDEP/E/
EXCI/ 0.25200/
JAN/ -2.244405E+01  1.096831E+01 -2.535504E+01  1.417378E+01
7.844989E+00 -5.718854E+00 -1.590012E+00  6.812124E-01  1.743617E-01/
E+CO2=>E+CO2                      6.0221E+23   0.000  0.0000E+00
DUPLICATE
```

```
TDEP/E/
EXCI/ 0.29100/
JAN/ -1.904069E+01  1.399371E-01 -2.725845E-01  1.874804E-01
2.166502E-02 -4.315053E-02 -9.492329E-03  5.116712E-03  8.701557E-04/
E+CO2=>E+CO2                    6.0221E+23   0.000  0.0000E+00
DUPLICATE
TDEP/E/
EXCI/ 0.33900/
JAN/ -2.197536E+01  3.883340E+00 -2.397676E+00 -1.847717E+00
6.777436E-01  1.024349E+00 -8.697746E-02 -1.485614E-01 -2.067820E-02/
E+CO2=>E+CO2                    6.0221E+23   0.000  0.0000E+00
DUPLICATE
TDEP/E/
EXCI/ 0.42200/
JAN/ -2.318815E+01  9.225298E+00 -2.856019E+01  2.259816E+01
6.119076E+00 -8.235519E+00 -1.410049E+00  9.994481E-01  2.161272E-01/
E+CO2=>E+CO2                    6.0221E+23   0.000  0.0000E+00
DUPLICATE
TDEP/E/
EXCI/ 0.50500/
JAN/ -2.278968E+01  9.228227E+00 -2.856355E+01  2.259814E+01
6.121422E+00 -8.235997E+00 -1.410561E+00  9.995278E-01  2.161674E-01/
E+CO2=>E+CO2                    6.0221E+23   0.000  0.0000E+00
DUPLICATE
TDEP/E/
EXCI/ 2.50000/
JAN/ -2.324588E+01  1.079415E+01 -2.510176E+01  1.412573E+01
7.715954E+00 -5.679731E+00 -1.565866E+00  6.763095E-01  1.725298E-01/
E+CO2=>E+CO2                    6.0221E+23   0.000  0.0000E+00
DUPLICATE
TDEP/E/
EXCI/ 7.00000/
JAN/ -2.319054E+01  2.949265E+00 -4.782813E+00  5.256168E+01
-1.689111E+02  2.441598E+02 -1.805137E+02  6.668733E+01 -9.773084E+00/
E+CO2=>E+CO2                   6.0221E+23   0.000  0.0000E+00
DUPLICATE
TDEP/E/
EXCI/10.50000/
JAN/ -2.546046E+01  4.270762E+00 -1.271120E+01  9.241019E+01
-2.307845E+02  2.754863E+02 -1.719785E+02  5.419520E+01 -6.805590E+00/
E+CO2=>E+CO+O(1D)              6.0221E+23   0.000  0.0000E+00
TDEP/E/
```

```
JAN/ -2.874875E+01  4.592190E+00 -1.294553E+01  9.301336E+01
-2.313972E+02  2.758184E+02 -1.719222E+02  5.406135E+01 -6.770907E+00/
E+CO2=>CO+O^-                   6.0221E+23   0.000  0.0000E+00
TDEP/E/
JAN/ -2.805562E+01  2.617842E+00 -5.284466E+00  4.930288E+01
-1.480970E+02  2.050178E+02 -1.467076E+02  5.277490E+01 -7.560917E+00/
E+CO=>E+CO                      6.0221E+23   0.000  0.0000E+00
DUPLICATE
TDEP/E/
/MOME
JAN/ -1.554328E+01  2.873505E-01 -5.913595E-01  1.109610E-01
1.947108E-01  8.767581E-03 -2.651309E-02 -7.035863E-03 -5.064147E-04/
E+CO=>E+CO                      6.0221E+23   0.000  0.0000E+00
DUPLICATE
TDEP/E/
EXCI/ 6.22000/
JAN/ -2.252577E+01  3.409528E+00 -6.061130E+00  5.445793E+01
-1.647415E+02  2.307412E+02 -1.668803E+02  6.060803E+01 -8.760293E+00/
E+CO=>E+CO                      6.0221E+23   0.000  0.0000E+00
DUPLICATE
TDEP/E/
EXCI/ 6.80000/
JAN/ -2.363209E+01  3.576259E+00 -5.412619E+00  5.526263E+01
-1.749596E+02  2.514463E+02 -1.851341E+02  6.817042E+01 -9.965250E+00/
E+CO=>E+CO                      6.0221E+23   0.000  0.0000E+00
DUPLICATE
TDEP/E/
EXCI/ 7.90000/
JAN/ -2.491226E+01  3.855181E+00 -1.054529E+00  5.064942E+01
-2.045718E+02  3.296718E+02 -2.609708E+02  1.012731E+02 -1.542142E+01/
E+CO=>E+CO                      6.0221E+23   0.000  0.0000E+00
DUPLICATE
TDEP/E/
EXCI/10.40000/
JAN/ -2.857374E+01  4.597971E+00  3.326827E+00  6.142586E+01
-2.903743E+02  4.917618E+02 -3.993844E+02  1.574840E+02 -2.424699E+01/
E+CO=>E+CO                      6.0221E+23   0.000  0.0000E+00
DUPLICATE
TDEP/E/
EXCI/10.60000/
JAN/ -2.809763E+01  4.525190E+00 -3.496770E-01  7.207939E+01
-2.879364E+02  4.575143E+02 -3.580278E+02  1.376777E+02 -2.081667E+01/
```

```
E+H2=>E+H2                      6.0221E+23   0.000  0.0000E+00
DUPLICATE
TDEP/E/
/MOME
JAN/ -1.347055E+01  3.097251E-01 -6.002074E-01  6.141886E-02
8.316040E-02 -1.694215E-02 -8.434694E-03 -7.696031E-04 -1.975527E-04/
E+H2=>E+H2                      0.0000E+00   0.000  0.0000E+00
DUPLICATE
TDEP/E/
EXCI/ 0.04400/
E+H2=>E+H2                      0.0000E+00   0.000  0.0000E+00
DUPLICATE
TDEP/E/
EXCI/ 0.07300/
E+H2=>E+H2                      0.0000E+00   0.000  0.0000E+00
DUPLICATE
TDEP/E/
EXCI/ 0.51600/
E+H2=>E+H2                      0.0000E+00   0.000  0.0000E+00
DUPLICATE
TDEP/E/
EXCI/ 1.00000/
E+H2=>E+H2                      0.0000E+00   0.000  0.0000E+00
DUPLICATE
TDEP/E/
EXCI/ 1.50000/
E+H2=>E+2H                      6.0221E+23   0.000  0.0000E+00
DUPLICATE
TDEP/E/
JAN/ -2.568639E+01  3.995066E+00  2.929773E+00  5.207720E+01
-2.496696E+02 4.252342E+02 -3.465777E+02  1.370224E+02 -2.114130E+01/
E+H2=>E+H2                      6.0221E+23   0.000  0.0000E+00
DUPLICATE
TDEP/E/
EXCI/11.30000/
JAN/ -2.801280E+01  4.616431E+00  3.725450E+00  6.634729E+01
-3.116604E+02 5.259906E+02 -4.261789E+02  1.677876E+02 -2.580724E+01/
E+H2=>E+H2                      6.0221E+23   0.000  0.0000E+00
DUPLICATE
TDEP/E/
EXCI/11.75000/
JAN/ -2.814162E+01  4.823454E+00  3.012137E+00  6.985318E+01
```

```
-3.197962E+02 5.356025E+02 -4.323458E+02  1.698028E+02 -2.606876E+01/
E+H2=>E+H2                      6.0221E+23   0.000  0.0000E+00
DUPLICATE
TDEP/E/
EXCI/11.80000/
JAN/ -2.879233E+01  5.137157E+00  1.920330E+00  7.306663E+01
-3.234278E+02 5.362149E+02 -4.306039E+02  1.685661E+02 -2.581912E+01/
E+H2=>E+H2                      6.0221E+23   0.000  0.0000E+00
DUPLICATE
TDEP/E/
EXCI/12.40000/
JAN/ -2.970681E+01  5.767162E+00  7.074903E-01  8.400253E+01
-3.540041E+02 5.768575E+02 -4.587552E+02  1.784232E+02 -2.720100E+01/
E+H2=>E+H2                      6.0221E+23   0.000  0.0000E+00
DUPLICATE
TDEP/E/
EXCI/13.86000/
JAN/ -5.451582E+01  4.361205E+01 -1.155724E+02  2.583738E+02
-3.628067E+02  3.170581E+02 -1.657646E+02  4.709627E+01 -5.576112E+00/
E+H2=>E+H2                      6.0221E+23   0.000  0.0000E+00
DUPLICATE
TDEP/E/
EXCI/14.00000/
JAN/ -3.251252E+01  1.156415E+01 -1.733606E+01  3.707124E+01
-5.757299E+01 5.701446E+01 -3.309353E+01  1.014569E+01 -1.266672E+00/
E+H2=>E+2H                      6.0221E+23   0.000  0.0000E+00
DUPLICATE
TDEP/E/
JAN/ -3.640328E+01  1.591586E+01 -2.616494E+01  5.819715E+01
-8.858077E+01 8.443624E+01 -4.710286E+01  1.391910E+01 -1.679343E+00/
E+H2=>E+H2                      6.0221E+23   0.000  0.0000E+00
DUPLICATE
TDEP/E/
EXCI/15.20000/
JAN/ -3.533387E+01  1.483849E+01 -2.456502E+01  5.569231E+01
-8.553675E+01 8.172019E+01 -4.545346E+01  1.335197E+01 -1.598990E+00/
E+H2=>E+2H                      6.0221E+23   0.000  0.0000E+00
DUPLICATE
TDEP/E/
JAN/ -3.768132E+01  1.477308E+01 -2.251116E+01  4.906982E+01
-7.603937E+01 7.447753E+01 -4.265279E+01  1.290364E+01 -1.590394E+00/
E+CH3=>E+CH3                    6.0221E+23   0.000  0.0000E+00
```

```
TDEP/E/
/MOME
JAN/ -1.880666E+01  4.355849E-01 -2.187509E-02  7.316557E-02
2.218076E-02 -2.657125E-02 -7.857029E-03  3.101043E-03  9.645206E-04/
E+CH3=>E+CH+H2                6.0221E+23   0.000  0.0000E+00
TDEP/E/
JAN/ -3.008018E+01  5.152053E+00  1.636014E+00  6.315869E+01
-2.809019E+02 4.671359E+02 -3.756267E+02  1.471390E+02 -2.254742E+01/
E+CH=>E+CH                    6.0221E+23   0.000  0.0000E+00
TDEP/E/
/MOME
JAN/ -1.880666E+01  4.355849E-01 -2.187509E-02  7.316557E-02
2.218076E-02 -2.657125E-02 -7.857029E-03  3.101043E-03  9.645206E-04/
E+O2(vib2)=>E+O2(vib2)        6.0221E+23   0.000  0.0000E+00
TDEP/E/
/MOME
JAN/ -1.688000E+01  4.237775E-01 -1.528840E-01  1.280344E-01
6.274124E-02 -1.180210E-02 -1.080037E-02 -1.700395E-03 -4.373597E-05/
E+O2(vib2)=>E+O2              6.0221E+23   0.000  0.0000E+00
TDEP/E/
JAN/ -2.306310E+01 -8.052326E-01  2.638262E-01 -1.362790E-01
-3.037674E-01 1.950509E-02  5.212861E-02  4.455218E-03 -1.431043E-03/
E+O2(vib3)=>E+O2(vib3)        6.0221E+23   0.000  0.0000E+00
TDEP/E/
/MOME
JAN/ -1.688000E+01  4.237775E-01 -1.528840E-01  1.280344E-01
6.274124E-02 -1.180210E-02 -1.080037E-02 -1.700395E-03 -4.373597E-05/
E+O2(vib3)=>E+O2              6.0221E+23   0.000  0.0000E+00
TDEP/E/
JAN/ -2.358159E+01  1.095267E+00  1.360410E+00 -5.617271E-01
-5.876480E-01 2.090032E-01  1.164851E-01 -2.573657E-02 -1.081866E-02/
E+O2(vib4)=>E+O2(vib4)        6.0221E+23   0.000  0.0000E+00
TDEP/E/
/MOME
JAN/ -1.688000E+01  4.237775E-01 -1.528840E-01  1.280344E-01
6.274124E-02 -1.180210E-02 -1.080037E-02 -1.700395E-03 -4.373597E-05/
E+O2(vib4)=>E+O2              6.0221E+23   0.000  0.0000E+00
TDEP/E/
JAN/ -2.436799E+01  1.693432E+00  1.281846E+00 -9.048703E-01
-6.244256E-01 3.403019E-01  1.438478E-01 -4.393817E-02 -1.543435E-02/
E+O2(a1)=>E+O2(a1)            6.0221E+23   0.000  0.0000E+00
TDEP/E/
```

```
/MOME
JAN/ -1.695285E+01  4.408161E-01 -1.169721E-01  1.595927E-01
4.264989E-02 -4.978464E-02 -1.380316E-02  5.610651E-03  1.686026E-03/
E+O2(a1)=>E+O2                6.0221E+23   0.000  0.0000E+00
TDEP/E/
JAN/ -2.338594E+01  1.054845E+00 -1.936937E-02 -1.008638E-01
-1.922600E-02 9.967528E-03  1.481504E-03 -1.569734E-03 -3.618162E-04/
E+O2(a1)=>E+O2(b1)            6.0221E+23   0.000  0.0000E+00
TDEP/E/
JAN/ -2.111650E+01  1.484745E+00 -3.812007E-01 -1.254913E-01
-2.687929E-02 1.231737E-01 -4.282118E-03 -1.452035E-02 -2.731100E-03/
E+O2(a1)=>E+O+O(1D)           6.0221E+23   0.000  0.0000E+00
TDEP/E/
JAN/ -2.351687E+01  3.618816E+00 -6.481397E+00  5.521459E+01
-1.637674E+02 2.268929E+02 -1.627669E+02  5.873874E+01 -8.447691E+00/
E+O2(a1)=>O+O^-               6.0221E+23   0.000  0.0000E+00
TDEP/E/
JAN/ -2.473310E+01  2.282604E+00 -4.700277E+00  4.654477E+01
-1.420963E+02 1.983340E+02 -1.428070E+02  5.165335E+01 -7.437720E+00/
E+O2(a1)=>2E+O2^+             6.0221E+23   0.000  0.0000E+00
TDEP/E/
JAN/ -2.947603E+01  5.388452E+00  1.539668E+00  7.048785E+01
-3.088859E+02 5.107566E+02 -4.094089E+02  1.600504E+02 -2.449163E+01/
E+O2(b1)=>E+O2(b1)            6.0221E+23   0.000  0.0000E+00
TDEP/E/
/MOME
JAN/ -1.695285E+01  4.408161E-01 -1.169721E-01  1.595927E-01
4.264989E-02 -4.978464E-02 -1.380316E-02  5.610651E-03  1.686026E-03/
E+O2(b1)=>E+O2                6.0221E+23   0.000  0.0000E+00
TDEP/E/
JAN/ -2.263284E+01  7.842137E-01 -4.618188E-02 -7.697215E-02
1.387915E-02 -3.427752E-03 -5.662667E-03  7.235036E-06  2.759739E-04/
E+O2(b1)=>E+O2(A3)            6.0221E+23   0.000  0.0000E+00
TDEP/E/
JAN/ -2.380384E+01  2.861986E+00 -7.283102E+00  5.370278E+01
-1.446454E+02 1.865209E+02 -1.262098E+02  4.329285E+01 -5.947913E+00/
E+O2(b1)=>E+2O                6.0221E+23   0.000  0.0000E+00
TDEP/E/
JAN/ -2.391501E+01  3.037427E+00 -7.838051E+00  5.474795E+01
-1.436710E+02 1.819407E+02 -1.212426E+02  4.101158E+01 -5.560469E+00/
E+O2(b1)=>E+O+O(1D)           6.0221E+23   0.000  0.0000E+00
TDEP/E/
```

```
JAN/ -2.616247E+01  3.534993E+00 -2.975010E+00  4.684438E+01
-1.602902E+02 2.391254E+02 -1.799457E+02  6.721746E+01 -9.929546E+00/
E+O2(b1)=>2E+O2^+             6.0221E+23   0.000  0.0000E+00
TDEP/E/
JAN/ -2.870471E+01  4.793886E+00 -2.139817E+00  7.577021E+01
-2.829628E+02 4.368915E+02 -3.357204E+02  1.273887E+02 -1.906141E+01/
E+O2(b1)=>O+O^-               6.0221E+23   0.000  0.0000E+00
TDEP/E/
JAN/ -2.362855E+01  3.850021E+00 -7.834142E+00  2.357032E+01
-4.796272E+01 5.624587E+01 -3.715312E+01  1.281600E+01 -1.793592E+00/
E+O2(A3)=>E+O2(A3)            6.0221E+23   0.000  0.0000E+00
TDEP/E/
/MOME
JAN/ -1.688000E+01  4.237775E-01 -1.528840E-01  1.280344E-01
6.274124E-02 -1.180210E-02 -1.080037E-02 -1.700395E-03 -4.373597E-05/
E+O2(A3)=>E+O2                6.0221E+23   0.000  0.0000E+00
TDEP/E/
JAN/ -2.041001E+01  4.136951E-01 -4.804525E-01  1.753114E-01
6.470600E-02 -6.349904E-02 -1.331553E-02  5.073702E-03  1.137868E-03/
E+N2(vib1)=>E+N2(vib1)        6.0221E+23   0.000  0.0000E+00
TDEP/E/
/MOME
JAN/ -1.630692E+01  4.854956E-01 -2.282758E-01  4.242349E-02
8.822978E-02 -6.909215E-03 -1.669398E-02 -4.261605E-04  7.501261E-04/
E+N2(vib1)=>E+N2              6.0221E+23   0.000  0.0000E+00
TDEP/E/
JAN/ -1.872755E+01  1.278687E+00 -2.100801E+00 -5.447786E-01
5.162753E-01  5.320673E-01 -9.307825E-02 -8.291849E-02 -9.648074E-03/
E+N2(vib1)=>E+2N              6.0221E+23   0.000  0.0000E+00
TDEP/E/
JAN/ -2.894372E+01  4.941644E+00  1.292085E+00  6.441895E+01
-2.738715E+02 4.459472E+02 -3.537386E+02  1.372116E+02 -2.087329E+01/
E+N2(vib1)=>2E+N2^+           6.0221E+23   0.000  0.0000E+00
TDEP/E/
JAN/ -3.318280E+01  1.368488E+01 -2.038903E+01  4.320208E+01
-6.458942E+01 6.147609E+01 -3.420591E+01  1.002182E+01 -1.192201E+00/
E+N2(vib4)=>E+N2(vib4)        6.0221E+23   0.000  0.0000E+00
TDEP/E/
/MOME
JAN/ -1.630801E+01  5.914051E-01 -1.988326E-01 -6.907961E-03
7.455820E-02 1.237335E-03 -1.458763E-02 -1.024869E-03  5.907874E-04/
E+N2(vib4)=>E+N2              6.0221E+23   0.000  0.0000E+00
```

```
TDEP/E/
JAN/ -1.890993E+01 -4.079217E-01 -8.117920E-01  3.975601E-01
2.743260E-02 -9.128820E-02 -5.792084E-02  2.223656E-02  7.869805E-03/
E+N2(vib5)=>E+N2(vib5)        6.0221E+23   0.000  0.0000E+00
TDEP/E/
/MOME
JAN/ -1.630801E+01  5.914051E-01 -1.988326E-01 -6.907961E-03
7.455820E-02 1.237335E-03 -1.458763E-02 -1.024869E-03  5.907874E-04/
E+N2(vib5)=>E+N2              6.0221E+23   0.000  0.0000E+00
TDEP/E/
JAN/ -1.900109E+01 -5.161459E-01 -4.759439E-01  1.992028E-01
-1.065115E-01 -3.420520E-02 -5.949926E-03  1.175284E-02  2.515243E-03/
E+N2(B3)=>E+N2(B3)            6.0221E+23   0.000  0.0000E+00
TDEP/E/
/MOME
JAN/ -1.630801E+01  5.914051E-01 -1.988326E-01 -6.907961E-03
7.455820E-02  1.237335E-03 -1.458763E-02 -1.024869E-03  5.907874E-04/
E+N2(B3)=>E+N2                6.0221E+23   0.000  0.0000E+00
TDEP/E/
JAN/ -2.174799E+01  4.356868E-01 -9.753053E-02  1.759575E-02
7.684151E-03 -1.385238E-02 -3.753852E-03  7.303078E-04  2.112233E-04/
E+N2(ap)=>E+N2(ap)            6.0221E+23   0.000  0.0000E+00
TDEP/E/
/MOME
JAN/ -1.630801E+01  5.914051E-01 -1.988326E-01 -6.907961E-03
7.455820E-02  1.237335E-03 -1.458763E-02 -1.024869E-03  5.907874E-04/
E+N2(ap)=>E+N2                6.0221E+23   0.000  0.0000E+00
TDEP/E/
JAN/ -2.098876E+01  5.593946E-01 -1.778728E-02  2.584482E-02
-1.546471E-02 -3.385040E-02 -4.632292E-03  4.512798E-03  1.096780E-03/
E+N2(C3)=>E+N2(C3)            6.0221E+23   0.000  0.0000E+00
TDEP/E/
/MOME
JAN/ -1.630801E+01  5.914051E-01 -1.988326E-01 -6.907961E-03
7.455820E-02  1.237335E-03 -1.458763E-02 -1.024869E-03  5.907874E-04/
E+N2(C3)=>E+N2                6.0221E+23   0.000  0.0000E+00
TDEP/E/
JAN/ -2.036785E+01  8.409769E-01 -3.213697E-01 -1.314690E-01
8.219385E-02 2.659800E-02 -1.126104E-02 -4.954046E-03 -4.759928E-04/
E+O^-=>E+O^-                  6.0221E+23   0.000  0.0000E+00
TDEP/E/
/MOME
```

```
JAN/ -1.420148E+01  4.355849E-01 -2.187509E-02  7.316557E-02
2.218076E-02 -2.657125E-02 -7.857029E-03  3.101043E-03  9.645206E-04/
E+O^-=>2E+O                    6.0221E+23   0.000  0.0000E+00
TDEP/E/
JAN/ -2.016032E+01  5.171619E+00 -2.082485E+00 -2.368713E+00
6.768875E-01  1.197051E+00 -6.757517E-02 -1.665461E-01 -2.425721E-02/
END
```

Bibliography

Moon Soo Bak, Hyungrok Do, Mark Godfrey Mungal, and Mark A Cappelli. Plasma-assisted stabilization of laminar premixed methane/air flames around the lean flammability limit. *Combust. Flame*, 159(10):3128–3137, 2012.

Memdouh Belhi, Pascale Domingo, and Pierre Vervisch. Modelling of the effect of DC and AC electric fields on the stability of a lifted diffusion methane/air flame. *Combust. Theor. Model.*, 2013.

John B Bell, Marcus S Day, Joseph F Grcar, Michael J Lijewski, James F Driscoll, and Sergei A Filatyev. Numerical simulation of a laboratory-scale turbulent slot flame. *Proceedings of the combustion institute*, 31(1):1299–1307, 2007.

Fabrizio Bisetti and Mbark El Morsli. Kinetic parameters, collision rates, energy exchanges and transport coefficients of non-thermal electrons in premixed flames at sub-breakdown electric field strengths. *Combust. Theor. Model.*, 2014. doi: 10.1080/13647830.2013.872300.

J Blamey, EJ Anthony, J Wang, and PS Fennell. The calcium looping cycle for large-scale CO2 capture. *Progress in Energy and Combustion Science*, 36(2):260–279, 2010.

John David Buckmaster and Geoffrey Stuart Stephen Ludford. *Theory of laminar flames*. Cambridge University Press, 1982.

Alexander Burcat and Branko Ruscic. *Third millenium ideal gas and condensed phase thermochemical database for combustion with updates from active thermochemical tables*. Argonne National Laboratory Argonne, IL, 2005.

John Burrows, Jim Lykowski, and Kristapher Mixell. Corona ignition system for highly efficient gasoline engines. *MTZ worldwide*, 74(6):38–41, 2013.

Jacqueline H Chen, Alok Choudhary, B De Supinski, M DeVries, ER Hawkes, S Klasky, WK Liao, KL Ma, J Mellor-Crummey, N Podhorszki, et al. Terascale direct numerical simulations of turbulent combustion using S3D. *Computational Science & Discovery*, 2 (1):015001, 2009.

Alexandre Joel Chorin. Numerical solution of the navier-stokes equations. *Mathematics of computation*, 22(104):745–762, 1968.

Phillip Colella and Paul R Woodward. The piecewise parabolic method (PPM) for gas-dynamical simulations. *Journal of computational physics*, 54(1):174–201, 1984.

Phillip Colella, Milo R Dorr, and Daniel D Wake. A conservative finite difference method for the numerical solution of plasma fluid equations. *Journal of Computational Physics*, 149(1):168–193, 1999.

Mark S Day and John B Bell. Numerical simulation of laminar reacting flows with complex chemistry. *Combustion Theory and Modelling*, 4(4):535–556, 2000.

Anthony Cesar DeFilippo. *Microwave-Assisted Ignition for Improved Internal Combustion Engine Efficiency, PhD Thesis*. University of California, Berkeley, 2013.

Robert Falgout and Ulrike Yang. hypre: A library of high performance preconditioners. *Computational Science ICCS 2002*, pages 632–641, 2002.

A.B. Fialkov. Investigations on ions in flames. *Prog. Energy Combust. Sci.*, 23(5-6):399–528, 1997.

Mike Folk, Albert Cheng, and Kim Yates. HDF5: A file format and I/O library for high performance computing applications. In *Proceedings of supercomputing*, volume 99, pages 5–33, 1999.

Wendell H Furry. On the elementary explanation of diffusion phenomena in gases. *American Journal of Physics*, 16(2):63–78, 1948.

Edward G Groff and Mark K Krage. Microwave effects on premixed flames. *Combustion and flame*, 56(3):293–306, 1984.

Donald A Gurnett and Amitava Bhattacharjee. *Introduction to plasma physics: with space and laboratory applications*. Cambridge university press, 2005.

GJM Hagelaar and LC Pitchford. Solving the boltzmann equation to obtain electron transport coefficients and rate coefficients for fluid models. *Plasma Sources Sci. Tech.*, 14(4): 722, 2005.

EP Hammond, K Mahesh, and P Moin. A numerical method to simulate radio-frequency plasma discharges. *Journal of Computational Physics*, 176(2):402–429, 2002.

Jie Han, Memdouh Belhi, Fabrizio Bisetti, and S Mani Sarathy. Numerical modelling of ion transport in flames. *Combustion Theory and Modelling*, 19(6):744–772, 2015.

Evatt R Hawkes, Ramanan Sankaran, James C Sutherland, and Jacqueline H Chen. Direct numerical simulation of turbulent combustion: fundamental insights towards predictive models. In *Journal of Physics: Conference Series*, volume 16, page 65. IOP Publishing, 2005.

Fred L Hinton. Collisional transport in plasma. *Handbook of Plasma Physics*, 1:147, 1983.

Joseph O Hirschfelder, Charles F Curtiss, Robert Byron Bird, and Maria Goeppert Mayer. *Molecular theory of gases and liquids*, volume 26. Wiley New York, 1954.

IEA. *Key World Energy Statistics 2015*. OECD/IEA, 2015.

Yuji Ikeda, Atsushi Nishiyama, and Masashi Kaneko. Microwave enhanced ignition process for fuel mixture at elevated pressure of 1MPa. *47th AIAA Aerospace Sciences Meeting Including the New Horizons Forum and Aerospace Exposition*, 2009.

Hong G Im, Arnaud Trouvé, Christopher J Rutland, and Jacqueline H Chen. Terascale high-fidelity simulations of turbulent combustion with detailed chemistry. Technical report, University of Maryland, College Park MD, 2012.

IPCC. Ipcc special report on renewable energy sources and climate change mitigation. 2011.

HC Jaggers and A Von Engel. The effect of electric fields on the burning velocity of various flames. *Combust. Flame*, 16(3):275–285, 1971.

Ratko K Janev, William D Langer, Douglas E Post Jr, and Kenneth Evans Jr. *Elementary processes in hydrogen-helium plasmas: cross sections and reaction rate coefficients*, volume 4. 1987.

Yiguang Ju and Wenting Sun. Plasma assisted combustion: Dynamics and chemistry. *Prog. Energ. Combust. Sci.*, 48:21–83, 2015.

Gautam T Kalghatgi and Derek Bradley. Pre-ignition and super-knock in turbo-charged spark-ignition engines. *International Journal of Engine Research*, 13(4):399–414, 2012.

RJ Kee, G Dixon-Lewis, J Warnatz, ME Coltrin, and JA Miller. The chemkin transport database. *Sandia National Laboratories, Livermore, CA, Report No. SAND86-8246*, 1986.

Robert J Kee, Joseph F Grcar, MD Smooke, JA Miller, and E Meeks. Premix: a fortran program for modeling steady laminar one-dimensional premixed flames, 1985.

Robert J Kee, Fran M Rupley, and James A Miller. Chemkin-II: A fortran chemical kinetics package for the analysis of gas-phase chemical kinetics. Technical report, Sandia National Labs., Livermore, CA (USA), 1989.

Bhupendra Khandelwal, Adam Karakurt, Paulas R Sekaran, Vishal Sethi, and Riti Singh. Hydrogen powered aircraft: the future of air transport. *Progress in Aerospace Sciences*, 60:45–59, 2013.

John Kim and Parviz Moin. Application of a fractional-step method to incompressible navier-stokes equations. *Journal of computational physics*, 59(2):308–323, 1985.

Kenneth K Kuo. Principles of combustion. 1986.

MF Lai, John B Bell, and Phillip Colella. A projection method for combustion in the zero mach number limit. In *Proceedings of the Eleventh AIAA Computational Fluid Dynamics Conference*, pages 776–783, 1993.

James Lawton and Felix Jiri Weinberg. *Electrical aspects of combustion*. Clarendon Press, 1969.

Edbertho Leal-Quirós. Plasma processing of municipal solid waste. *Brazilian Journal of Physics*, 34(4B):1587–1593, 2004.

Sanjiva K Lele. Compact finite difference schemes with spectral-like resolution. *Journal of computational physics*, 103(1):16–42, 1992.

Shankar Mahadevan and Laxminarayan L Raja. Simulations of direct-current air glow discharge at pressures 1 torr: Discharge model validation. *Journal of Applied Physics*, 107 (9):093304, 2010.

Andrew Majda and James Sethian. The derivation and numerical solution of the equations for zero mach number combustion. *Combustion science and technology*, 42(3-4):185–205, 1985.

Aram H Markosyan, Jannis Teunissen, Saša Dujko, and Ute Ebert. Comparing plasma fluid models of different order for 1D streamer ionization fronts. *Plasma Sources Science and Technology*, 24(6):065002, 2015.

Michael L Minion. Semi-implicit projection methods for incompressible flow based on spectral deferred corrections. *Applied numerical mathematics*, 48(3):369–387, 2004.

Sharath Nagaraja, Vigor Yang, and Igor Adamovich. Multi-scale modelling of pulsed nanosecond dielectric barrier plasma discharges in plane-to-plane geometry. *Journal of Physics D: Applied Physics*, 46(15):155205, 2013.

Sharath Nagaraja, Wenting Sun, and Vigor Yang. Effect of non-equilibrium plasma on two-stage ignition of n-heptane. *Proc. Combust. Inst.*, 35(3):3497–3504, 2015.

TE Nitschke and DB Graves. A comparison of particle in cell and fluid model simulations of low-pressure radio frequency discharges. *J. Appl. Phys.*, 76(10):5646–5660, 1994.

S Pancheshnyi, B Eismann, GJM Hagelaar, and LC Pitchford. Computer code zdplaskin. In *11th Int. Symp. on High Pressure, Low Temperature Plasma Chemistry*, 2008.

S Pancheshnyi, S Biagi, MC Bordage, GJM Hagelaar, WL Morgan, AV Phelps, and LC Pitchford. The lxcat project: Electron scattering cross sections and swarm parameters for low temperature plasma modeling. *Chem. Phys.*, 398:148–153, 2012.

Daniel I Pineda and Jyh-Yuan Chen. Effects of updated transport properties of singlet oxygen species on steady laminar flame simulations. *Western States Section Spring Technical Meeting of the Combustion Institute, Seattle, WA*, 2016.

Daniel I Pineda, Benjamin Wolk, Tim Sennott, Jyh-Yuan Chen, Robert W Dibble, and Daniel Singleton. Nanosecond pulsed discharge in a lean methane-air mixture. In *Laser Ignition Conference*, pages T5A–2. Optical Society of America, 2015.

Jonathan Poggie, I Adamovich, N Bisek, and Munetake Nishihara. Numerical simulation of nanosecond-pulse electrical discharges. *Plasma Sources Science and Technology*, 22(1): 015001, 2012.

T J&amp Poinsot and SK Lele. Boundary conditions for direct simulations of compressible viscous flows. *Journal of computational physics*, 101(1):104–129, 1992.

Thierry Poinsot and Denis Veynante. *Theoretical and numerical combustion*. RT Edwards, Inc., 2005.

J Prager, U Riedel, and J Warnatz. Modeling ion chemistry and charged species diffusion in lean methane–oxygen flames. *Proc. Combust. Inst.*, 31(1):1129–1137, 2007.

Ronald G Rehm and Howard R Baum. The equations of motion for thermally driven, buoyant flows. *Journal of Research of the National Bureau of Standards*, 83(3), 1978.

Michael W Schmidt, Kim K Baldridge, Jerry A Boatz, Steven T Elbert, Mark S Gordon, Jan H Jensen, Shiro Koseki, Nikita Matsunaga, Kiet A Nguyen, Shujun Su, et al. General atomic and molecular electronic structure system. *Journal of computational chemistry*, 14 (11):1347–1363, 1993.

Gregory P Smith, David M Golden, Michael Frenklach, Nigel W Moriarty, Boris Eiteneer, Mikhail Goldenberg, C Thomas Bowman, Ronald K Hanson, Soonho Song, William C Gardiner Jr, et al. GRI-mech 3.0. available at `<http://www.me.berkeley.edu/gri_mech/>`, 1999.

N Speelman, LPH de Goey, and JA van Oijen. Development of a numerical model for the electric current in burner-stabilised methane–air flames. *Combustion Theory and Modelling*, 19(2):159–187, 2015a.

N Speelman, M Kiefer, D Markus, U Maas, LPH de Goey, and JA van Oijen. Validation of a novel numerical model for the electric currents in burner-stabilized methane–air flames. *Proceedings of the Combustion Institute*, 35(1):847–854, 2015b.

Lyman Spitzer Jr. The stability of isolated clusters. *Monthly Notices of the Royal Astronomical Society*, 100:396, 1940.

SM Starikovskaia. Plasma assisted ignition and combustion. *Journal of Physics D: Applied Physics*, 39(16):R265, 2006.

Andrey Starikovskiy and Nickolay Aleksandrov. Plasma-assisted ignition and combustion. *Progress in Energy and Combustion Science*, 39(1):61–110, 2013.

R Steeneveldt, B Berger, and TA Torp. CO2 capture and storage: closing the knowing–doing gap. *Chemical Engineering Research and Design*, 84(9):739–763, 2006.

Wenting Sun and Yiguang Ju. Nonequilibrium plasma-assisted combustion: a review of recent progress. *J. Plasma Fusion Res.*, 89(4):208–219, 2013.

M Surendra and M Dalvie. Moment analysis of rf parallel-plate-discharge simulations using the particle-in-cell with monte carlo collisions technique. *Physical Review E*, 48(5):3914, 1993.

YF Tham, F Bisetti, and J-Y Chen. Development of a highly reduced mechanism for iso-octane hcci combustion with targeted search algorithm. *J. Eng. Gas Turb. Power*, 130(4): 042804, 2008.

Tamás Turányi. Applications of sensitivity analysis to combustion chemistry. *Reliability Engineering & System Safety*, 57(1):41–48, 1997.

Mruthunjaya Uddi, Naibo Jiang, Evgeny Mintusov, Igor V Adamovich, and Walter R Lempert. Atomic oxygen measurements in air and air/fuel nanosecond pulse discharges by two photon laser induced fluorescence. *Proceedings of the Combustion Institute*, 32(1):929–936, 2009.

UNDP. *Human Development Report*. 2006.

Hai Wang, Xiaoqing You, Ameya V Joshi, Scott G Davis, Alexander Laskin, Fokion Egolfopoulos, Chung K Law, and USC Mech Version II. High-temperature combustion reaction model of H2. Technical report, CO/C1-C4 Compounds, 2007.

FA Williams. Elementary derivation of the multicomponent diffusion equation. *American Journal of Physics*, 26(7):467–469, 1958.

Benjamin Wolk, Anthony DeFilippo, Jyh-Yuan Chen, Robert Dibble, Atsushi Nishiyama, and Yuji Ikeda. Enhancement of flame development by microwave-assisted spark ignition in constant volume combustion chamber. *Combust. Flame*, 160(7):1225–1234, 2013.

Sang Hee Won, Bo Jiang, Pascal Diévart, Chae Hoon Sohn, and Yiguang Ju. Self-sustaining n-heptane cool diffusion flames activated by ozone. *Proceedings of the Combustion Institute*, 35(1):881–888, 2015.

Chun Sang Yoo and Hong G Im. Characteristic boundary conditions for simulations of compressible reacting flows with multi-dimensional, viscous and reaction effects. *Combust. Theor. Model.*, 11(2):259–286, 2007.